RELATING FATIGUE CRACK GROWTH TO MICROSTRUCTURE VIA MULTISCALE DIGITAL IMAGE CORRELATION

BY

JAY CARROLL

DISSERTATION

Submitted in partial fulfillment of the requirements
for the degree of Doctor of Philosophy in Mechanical Engineering
in the Graduate College of the
University of Illinois at Urbana-Champaign, 2011

Urbana, Illinois

Doctoral Committee:

Professor Huseyin Sehitoglu, Chair
Professor John Lambros, Director of Research
Professor Daniel Tortorelli
Professor Robert Dodds
Professor Ravinder Chona, Air Force Research Laboratory

Abstract

This work investigates fatigue crack growth at multiple scales and links material deformation to microstructural properties. The optical technique of digital image correlation (DIC) is well suited for this task since it provides quantitative full-field deformation measurements at multiple length scales.

The first part of this work introduces two DIC-based techniques for measuring fatigue crack closure levels and demonstrates them on titanium. At the macroscale, a least squares regression was performed on full field measurements of displacement near the crack tip. At the microscale, two-point virtual extensometers were placed on the crack flanks behind the crack tip. These two measurement techniques provided crack closure level measurements from multiple scales that were consistent with one another.

In the second part of this work, fatigue crack growth was observed in a nickel based superalloy, Hastelloy X, at the grain level. A novel high resolution *ex situ* DIC technique was developed and used to measure accumulated strain fields in the plastic wake of a fatigue crack. Additionally, the evolution of the strain field as the fatigue crack grew through the imaging region was captured using an *in situ* real time DIC technique. Finally, these strain fields (from both *ex situ* and *in situ* measurements) were related to microstructural geometry and orientation

obtained through electron backscatter diffraction (EBSD). By linking accumulated fatigue strain to microstructure, a deeper understanding of fatigue crack growth was obtained.

Plastic deformation in fatigue crack growth was found to follow lobes of high strain that emanate from the crack tip at angles of 45°. These lobes leave behind an inhomogeneous strain field in which slip bands and strain localizations on grain boundaries were observed. Fatigue crack growth was observed to be transgranular following lines of slip bands as dictated by global loading and local microstructure.

To Science and Reason!

Acknowledgements

I am grateful to a number of people who supported me and gave me many fond memories during my time at the University of Illinois. I was lucky to have such an outstanding advisor as Professor John Lambros. I am grateful to John for his guidance and for helping me see the big picture when it is so easy to focus on the details. The analysis, writing, and presentation skills I learned from him will stay with me for life.

I had additional support from Professor Huseyin Sehitoglu as my co-advisor. He took me into his group as one of his own students and provided me with valuable insights and an incredible memory full of good references. I also want to thank my committee members, Professor Ravi Chona from Air Force Research Laboratory, Professor Bob Dodds, Professor Dan Tortorelli, and Professor Glaucio Paulino for the time and effort they spent making sure this work was as good as it could be. They pointed out more paths than I could possibly follow and helped me pick the right one. The Midwest Structural Sciences Center (MSSC) funded me throughout my Ph.D. and provided me with many opportunities to present my work at several conferences.

Thanks to Peter Kurath for knowing where to hit the machines to keep them running, Gavin Horn for giving me sensible advice when I most needed it, Rick Rottet for help with Labview, and Professor Darrell Socie for teaching me to focus on the important parts.

One of the benefits of having two advisors is that it also means having two sets of labmates. I enjoyed many debates, collaborations, and fun times with the students in Professor Sehitoglu's lab (team MEB) and in Professor Lambros's lab (team Talbot). In particular, I want to thank Christos Efstathiou for teaching me how science is done in the real world. Thanks to Wael Abuzaid for keeping my nose to the grindstone, Tawhid Ezaz for showing me how hard I could be working, and Garrett Pataky for showing me interesting applications of my work and for helping me strategize. Mallory Casperson's unrelenting cheerfulness made my time here much brighter and I was proud to assist her with her research. I am indebted to Henry Padilla for allowing me to follow in his footsteps, not only in my Ph.D. work, but also after graduation at Sandia National Laboratory. I appreciate Owen Kingstedt for bringing the Lambros lab together as friends. I looked forward to our group lunches each week, and I enjoyed the collaboration, discussions, and friendship I had with both groups. In particular, I appreciate the support and friendship of Reggie Hamilton, Mike Sangid, John Oyelakin, Piyas Bal Chowdhury, Shahla Chowdhury, Luca Patriarca, Alpay Oral, Jifeng Wang, Joe Gonzalez, Tommy On, Erheng Wang, Bharath Swaminathan, and Mark Gates and the good times we had both in and out of the office.

Lastly, I owe a great deal to my family. My parents taught me the value of education and encouraged my engineering capabilities to blossom. They had patience and allowed me to attempt to fix things when they heard my catchphrase "That doesn't look like it was designed very well." I also want to thank my wife for putting up with a long distance relationship off and on for six years, for talking to me on those homesick nights, and for helping me balance work and life.

Table of Contents

List of Figures

List of Tables

Chapter 1: Introduction

Despite decades of research efforts, most fatigue crack growth models are currently phenomenological in nature with fatigue crack growth rate predictions based primarily on the 50-year-old Paris relationship with slight modifications to account for more complex phenomena such as crack closure or frequency effects. Physics-based multiscale fatigue crack growth models have the potential to provide improved lifetime predictions over a wider variety of loading situations, but the development of such models requires corresponding multiscale measurements of fatigue crack growth deformations and their relation to microstructure. Although many experiments have provided a qualitative link of fatigue crack growth to microstructure, and have explained the physical basis of fatigue (Suresh, 1998), quantitative results to support novel physics-based models are lacking.

The research described in this thesis concentrates on experimental studies of fatigue crack growth performed with multiscale digital image correlation techniques – a method ideally suited for full-field quantitative measurements at multiple length scales. The first part of this thesis presents the introduction and use of experimental techniques for measuring fatigue crack closure at multiple scales. The second part of this work uses novel experimental techniques for linking multiscale measurements of strain accumulation to microstructure. Several researchers have investigated the relationship between fatigue crack growth and microstructure (see section 1.1); however, the measurements presented in this thesis are unprecedented in both the amount of

information and in their spatial resolution. Full-field measurements of strain accumulation, and their development over time, are made with sub-grain level resolution over regions spanning hundreds of grains. These strain measurements are then linked to measurements of grain geometry, grain orientation, and crack path information to provide insights into the mechanisms of fatigue crack growth.

1.1 Background

1.1.1 Fatigue Crack Growth

There are five stages of fatigue: (1) microstructural changes leading to permanent damage accumulation, (2) microcrack nucleation, (3) microcrack growth and coalescence into a dominant crack, (4) growth of the dominant fatigue crack, and (5) fracture. Component lifetimes in high cycle fatigue (*i.e.*, low stress and lifetimes $\gtrsim$ 10,000 cycles) are dominated by microcrack nucleation with relatively little time spent in the other two stages. In low cycle fatigue (*i.e.*, high stress and lifetimes $\lesssim$ 10,000 cycles), many microcracks nucleate in the early cycles, but most of the fatigue life is spent linking microcracks to form a dominant crack. Fatigue crack growth analysis is used when a significant portion of the lifetime is spent growing a single crack to failure. Because the focus of this work is fatigue crack growth, notched specimens are used so that a dominant fatigue crack initiates early.

Fatigue crack growth is divided into two stages. Stage I fatigue crack growth typically occurs when cracks are microstructurally short and is characterized by a crack tip plastic zone size that is smaller than the grain size. In stage I, fatigue cracks follow slip systems within grains changing direction at grain boundaries. Once the crack has grown through several grains, its associated plastic zone covers multiple grains, and it is said to be in stage II crack growth. The fatigue crack path in stage II is largely dominated by global loading conditions that cause the

crack to generally grow perpendicular to the direction of maximum principal stress. Although stage II fatigue crack growth is often thought of as independent of microstructure, the crack path still changes direction according to microstructural parameters. The interplay between global crack driving force and microstructural effects on crack path in stage II fatigue crack growth will be discussed extensively in this thesis.

Fatigue crack growth in metals occurs by the repeated blunting and shear deformation process shown in Fig. 1.1 (Laird 1963). As a cracked specimen is loaded, the material at the crack tip yields in shear deformation at angles to the crack tip resulting in crack tip blunting. Unloading subsequently results in a sharpening of the crack as the elastic material surrounding the crack tip region forces the crack closed once again. Although this basic fatigue crack growth mechanism does not explicitly consider the effects of microstructure, the concept can be used to qualitatively explain many of the features seen in experimental observations of fatigue crack growth. However, a quantitative understanding, necessary for model development, must include the effects of microstructure that take place at scales larger than the Laird (1963) model describes. At the first instance, this can be thought of as the collective response of two or more grains in the vicinity of the crack tip. Interaction at this scale would include the effects of grain boundaries in the evolution of plastic deformation in fatigue. The grain boundaries may act either as deformation initiators, or as deformation inhibitors depending upon the type of the boundary and/or the local loading conditions. Additionally, in materials exhibiting twinning, the presence of twins near the crack tip can introduce additional boundary interaction effects.

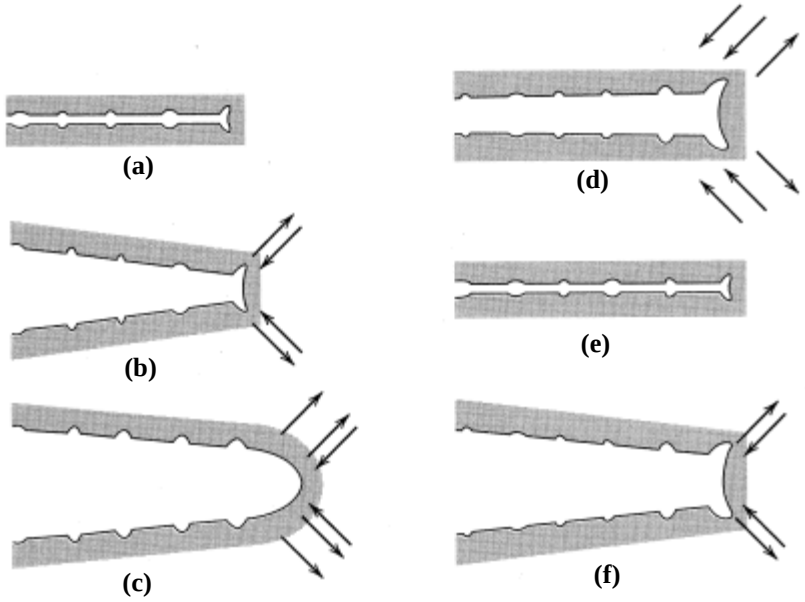

Fig. 1.1. Mechanism of fatigue crack propagation proposed by Laird in 1963 (from Callister, 1999). (a) Unloaded, (b) increasing tension, (c) peak load, (d) unloading, (e) unloaded, (f) increasing load on the subsequent cycle.

1.1.2 Strain Measurements in Fatigue Crack Growth

Researchers have been attempting to relate fatigue crack growth to microstructure for decades following the early work of Laird (1963). Lankford and Davidson (1983) studied striations and crack growth rates in relation to crack closure, and Davidson (1984) studied slip localizations at the crack tip. Despite extensive study of fatigue cracking, published measurements of full-field strains associated with fatigue crack growth are relatively limited. One of the earliest measurements of the strain field near a fatigue crack was made by Morris *et al.* (1985) who computed strains by manually comparing optical micrographs in a rudimentary form of digital image correlation. These low resolution strain fields were used to examine the shape of the plastically deformed material in the single grain on the surface containing the crack tip.

More recently, Peralta *et al.* (2005) studied crack nucleation and fatigue growth rates in relation to microstructure at the crack tip (without any measurements of strain fields). Peralta *et*

al. (2007) is one of the few studies to have full-field measurements of strain fields in fatigue crack growth; however, in their work, there was little consideration of microstructure. These researchers measured the strain field around crack tips for several specimens and found strain localizations in lobes along slip bands ahead of the crack tip. These deformation bands emanating from the crack tip were not symmetrically distributed with respect to the local crack direction. The relationship between fatigue crack strain fields and microstructure has been recognized as an important one by many researchers including the ones listed above. However, not until recent advances in computing, digital imaging, and electron microscopy has the acquisition of high resolution strain fields and their comparison with microstructure been possible.

1.1.3 Digital Image Correlation

This work uses the experimental technique of digital image correlation (DIC) extensively. DIC is a technique for measuring full-field displacements by comparing an image of a deformed specimen surface to a reference image at an earlier state. The algorithm is relatively simple and will not be described here in detail. More information can be found in and Sutton *et al.* (1983, 2009). Briefly, the method tracks the displacements of markers on the specimen surface between the two images. For full-field measurements, a random placement of markers, called a speckle pattern (Fig. 1.2), works better than a periodic grid pattern, which has also been used in what are referred to as grid methods (Delaire *et al.* 2000; Clayton *et al.*, 2002; Héripré *et al.*, 2007).

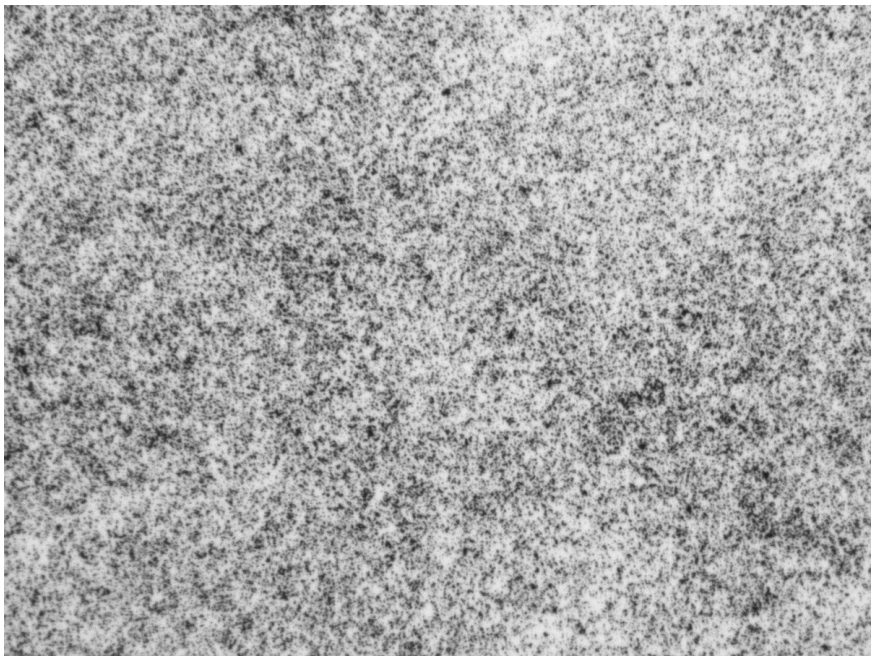

Fig. 1.2. Example of a speckle pattern for digital image correlation.

Because individual pixel intensities within an image are not unique, the algorithm measures displacements by searching for the best correlation between images of square groupings of pixels, called subsets. Subsets are defined in the reference image, and optimization techniques are used to find its best match is in the deformed image, thus providing a displacement vector assigned to that subset's center, referred to as a correlation point. This process is repeated for many correlation points in the image to obtain a displacement field. The location of a point within the subset in the deformed image $(\tilde{x}, \tilde{y})$ is given by a Taylor expansion about the center point, *P*, of the subset in the reference image (x_0, y_0):

$$\tilde{x} = x_0 + u_0 + \frac{du}{dx}\Delta x + \frac{du}{dy}\Delta y + \frac{1}{2}\frac{d^2u}{dx^2}\Delta x^2 + \frac{1}{2}\frac{d^2u}{dy^2}\Delta y^2 + \frac{d^2u}{dxdy}\Delta x\Delta y \qquad (1.1)$$

$$\tilde{y} =, y_0 + v_0 + \frac{dv}{dx}\Delta x + \frac{dv}{dy}\Delta y + \frac{1}{2}\frac{d^2v}{dx^2}\Delta x^2 + \frac{1}{2}\frac{d^2v}{dy^2}\Delta y^2 + \frac{d^2v}{dxdy}\Delta x\Delta y, \qquad (1.2)$$

where (x, y) are the reference coordinates of the point. The horizontal and vertical displacement fields are represented by u and v, respectively, and $\Delta x = x - x_0$, $\Delta y = y - y_0$. In any but the

simplest of cases (such as rigid translation), subsets will not remain square. The higher order terms including displacement gradients (and the second order terms) in eq. 1.1 and eq. 1.2 allow the subsets to change shape according to material deformation as shown in Fig. 1.3. This transformation considers all points within the subset so that an arbitrary point Q maps to Q' in the deformed image (Fig. 1.3).

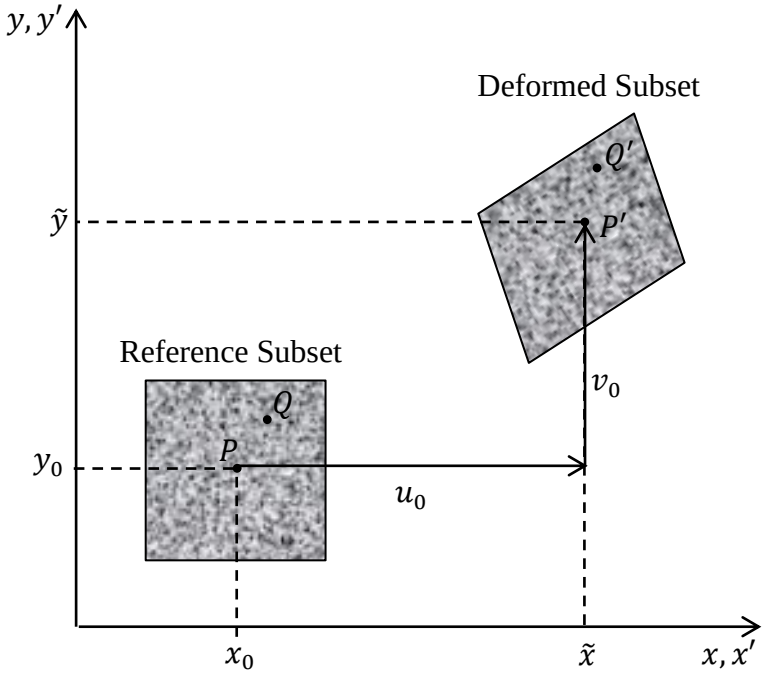

Fig. 1.3. Subsets are mapped to their deformed locations to determine the displacement at each correlation point.

From the above discussion, it is clear that the subset size, and indirectly the pixel size, is what controls the measurement resolution of DIC. However, since neither the subset size nor the pixel size are fixed physical parameters, DIC does not possess an inherent length scale, unlike interferometric or other light based methods that are limited in their resolution by length scales. Therefore, DIC is ideally suited for multiscale measurements across length scales. The limiting factors of DIC length scales are simply the availability of high magnification images and the generation of a suitable speckle pattern in these images. Consequently, DIC has been used in

experimental studies at a wide variety of length scales. DIC has been used at the macroscale to measure deflections in bridges (Yoneyama *et al.,* 2007). At the mesoscale, the behavior of collections of grains can be observed (Padilla *et al.,* 2011). At the microscale (Lambros and Patel, 2011), sub-grain level deformation can be captured. DIC can even be extended to the nanoscale as in Jonnalagadda *et. al.* (2010b) to investigate the properties of nanocrystalline gold films.

In the execution of DIC, typical subset sizes range from 21 x 21 pixels to 101 to 101 pixels depending on the quality of the speckle pattern achieved[1]. Subsets are allowed to overlap one another significantly; the distance between subset centers, called the subset spacing, is typically 5 or 10 pixels (in both directions). Because a typical image consists of 1600 x 1200 pixels, there are usually several thousands of subsets per image, with each subset giving a displacement measurement at its correlation point, allowing for full-field displacement measurements. Note that although rigid body displacements are captured by DIC, they can often be accounted for (as in chapter 2). In any case, strain fields, which are frequently used in analyzing material behavior, automatically ignore rigid body motion because strains are computed by differentiating DIC displacements.

1.2 Objectives

The overall objective of this work is to obtain a detailed high resolution quantitative evaluation of fatigue damage accumulation, both ahead of and behind a propagating crack tip, at a number of length scales that span the macroscale (defined as the scale at which individual grain response is smeared out) to the microscale (defined as having sub-grain level resolution). In

[1] The quality of the pattern dictates the subset size because the number and size of speckle features within a subset have to be sufficient to allow correlation between the two images.

areas behind the crack tip, fatigue influence can be realized as a plastic wake surrounding the crack tip that can lead to the beneficial shielding effect of crack closure (Elber, 1970). For the purposes of this work, which will deal with metallic materials, fatigue damage ahead of the crack tip, is thought of as plastic strain that accumulates at a microstructural level over a number of cycles.

To move toward achieving this overall goal, the specific objectives of this work are to:

(i) Develop and assess multiscale techniques for measuring crack closure. Although closure has been extensively studied in the past, an analysis relating macroscale and microscale effects has not been performed.

(ii) Develop novel techniques that can provide ultra-high resolution, full-field displacement measurements at the sub-grain level: The lack of an inherent length scale of DIC makes it ideally suitable for this part of the study. Obtaining such unprecedented measurement resolution will allow far better quantitative development and assessment of fatigue damage accumulation models.

(iii) Use the developed methods to acquire multiscale measurements of strain field generation and evolution associated with fatigue crack growth. Such measurements will allow us to develop a physical understanding of how fatigue damage evolves at one length scale higher than the laird (1963) model (Fig. 1.1) where sub-grain and grain-grain interaction and collective grain response effects can all be studied simultaneously.

(iv) Relate strain localizations and fatigue crack path to microstructural characteristics: Eventually, a true multiscale fatigue crack growth model will need to determine how microstructural details relate to plastic strain accumulation and eventually material failure. In this work, we would like to experimentally establish the capability to *directly*

link microstructural information such as grain shape, size, orientation, *etc.* to the corresponding strain accumulation.

1.3 Thesis Outline

This section provides a brief overview of the layout of this thesis to aid the reader in following the portions of interest. Chapter 2 deals with the application of DIC at the macroscale and demonstrates the use of a least squares regression method for extracting macroscopic stress intensity factors from displacement fields. Chapter 3 uses DIC virtual extensometers for measuring local crack closure values along the crack line (a microscale method). Additionally, two full-field (macroscale) methods for measuring crack closure, (based on the regression technique from chapter 2) are introduced in chapter 3. These two techniques are demonstrated and results are compared to local crack closure measurements from the microscale method. In chapter 4, experiments are discussed that use multiscale DIC to measure strain accumulation resulting from fatigue crack growth at two different length scales. In the first case, a titanium specimen is etched to reveal grain boundaries in order to relate DIC strain measurements to grain geometry as the crack growth is imaged at 14x magnification (a moderate magnification for this work that can be considered to image at the mesoscale, *i.e.*, several dozens of grains). The second approach discussed in chapter 4 demonstrates *in situ*, real time, multiscale strain field measurements for fatigue crack growth in Hastelloy X by *simultaneously* observing a fatigue crack with 14x magnification (mesoscale) and with 2x magnification (macroscale). Chapter 5 introduces a novel *ex situ* technique for linking ultra-high resolution, sub-grain level strain field measurements to microstructural details that include more than just grain boundaries. This is achieved by precisely aligning high resolution DIC measurements with electron backscatter diffraction (EBSD) data that provide a wealth of microstructural data in addition to grain shape

and size. The novel technique is demonstrated on a specimen of Hastelloy X, a nickel-based high-temperature superalloy, by periodically removing the specimen from the load frame for *ex situ* imaging. In chapter 6, an *in situ* DIC technique is combined with the high resolution *ex situ* technique to observe the development of sub-grain level strain fields and their relation to microstructural properties. The ultra-high resolution *ex situ* technique provides excellent spatial resolution while the *in situ* technique provides excellent temporal measurement resolution. Finally, conclusions and suggestions for future work are given in chapter 7.

Chapter 2: Measurements of Stress Intensity Factor during Fatigue Crack Growth from DIC Displacements

2.1 Two Approaches for DIC Measurements

In fatigue crack growth, each fatigue cycle generates a plastic zone at the current crack tip location. As the crack propagates, the plastic zone generated during each cycle is left behind forming a wake of plastically deformed material behind the crack tip. This process is shown in Fig. 2.1 (from Elber, 1971) and is the basis for plasticity-induced crack closure.

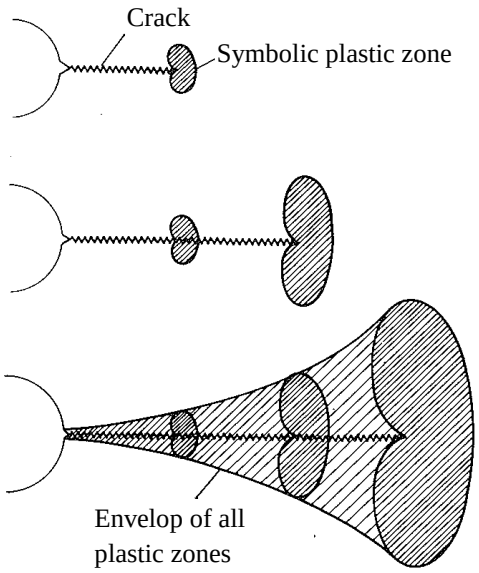

Fig. 2.1. The development of a wake of plastically deformed material behind a fatigue crack (from Elber, 1971). The plastic zones of past cycles are left behind as the crack tip moves forward.

In this thesis, two different approaches will be taken to study the strain associated with fatigue crack growth. In the first approach, a typical fatigue cycle will be examined by capturing many images *within* a fatigue cycle as shown in Fig. 2.2a. By correlating these images with the

first image of the cycle, this approach reveals details about strain accumulation within a single cycle similar to the first picture in Fig. 2.1. In the second approach, DIC is performed *between* cycles by capturing a reference image at one cycle and a deformed image at the same load level in a later cycle as shown in Fig. 2.2. The cycle for the deformed image could come immediately after the reference cycle or it could be tens of thousands cycles after the reference cycle. For the work shown in this thesis, the spacing between reference and deformed cycles is as little as 16 cycles in some cases and as large as 200,000 cycles in others. The second approach reveals details about the plastic wake of the fatigue crack, *i.e.*, the region highlighted in the third picture of Fig. 2.1. Performing DIC between cycles in this way gives measurements of plastic fatigue strain accumulation that can be used to investigate how fatigue damage develops. If no plasticity is accumulated between cycles, then the correlation using the second approach should yield a zero result. Of course, any deformation that occurs before the reference cycle will not be captured.

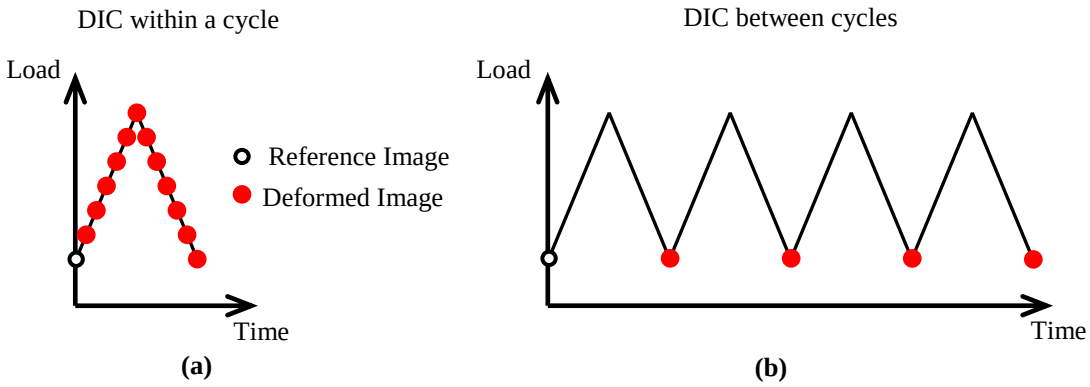

Fig. 2.2. Schematic comparing within cycles to between cycles.

Sample results from the two methods, taken from this thesis, are shown in Fig. 2.3 The ε_{yy} strain field (strain perpendicular to the crack line) within a single cycle is shown in Fig. 2.3a with the crack tip at 0,0 as indicated by the white dot. Fatigue strain accumulation (ε_{yy}) measured by correlating between cycles is shown in Fig. 2.3b. In this plot, the reference image was taken

before any fatigue loading, and the deformed image was taken after the crack had grown through the entire imaging region. The notch can be seen as the black region on the left side of the plot with the crack going horizontally through the image. The plots shown in Fig. 2.3 are experimental measurements of the phenomena described in the first and third pictures of Fig. 2.1a with a single plastic zone in Fig. 2.3a and a wake of plastically deformed material in Fig. 2.3b.

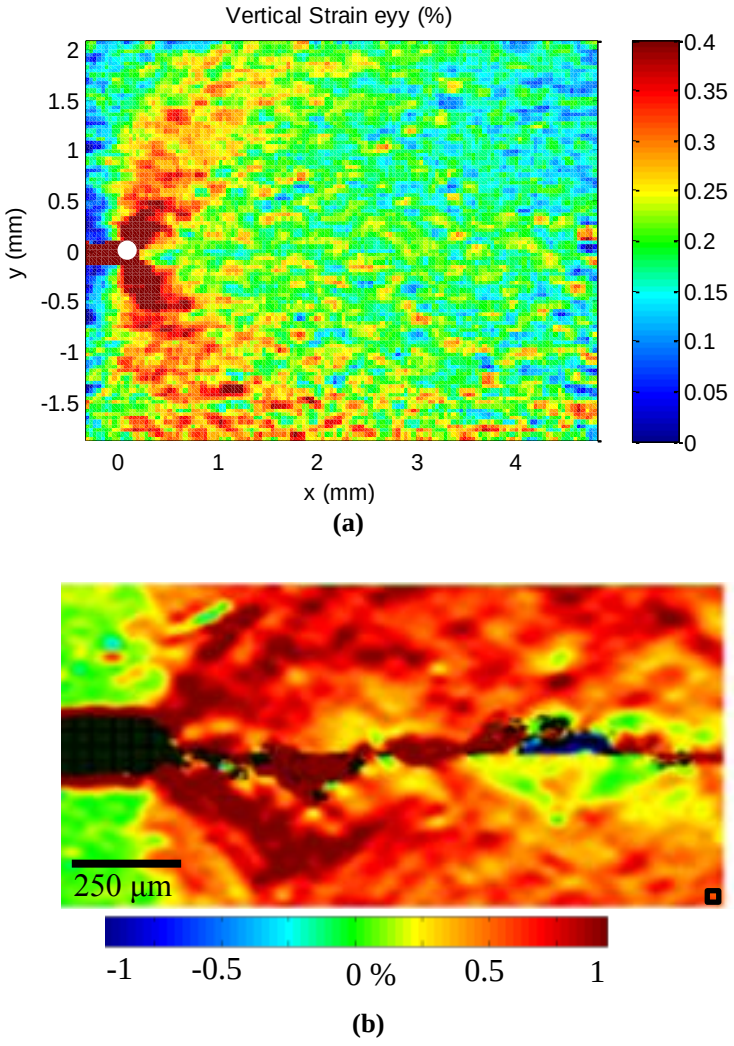

Fig. 2.3. Strain fields, ε_{yy}, from (a) DIC performed within a single cycle (taken from Fig. 2.10a) and (b) DIC performed between two cycles showing fatigue strain accumulation (taken from Fig. 4.11).

The work shown in this and the next chapter will focus primarily on the first approach of studying a single fatigue cycle at a time while fatigue damage accumulation over a number of

cycles will be discussed in later chapters. This chapter shows a methodology for experimentally extracting stress intensity factors from DIC displacement measurements surrounding a fatigue crack tip. This is done by performing a least squares regression on the DIC crack tip displacement fields. This method has been in use for decades with data acquired from the experimental techniques of photoelasticity (Eftis *et al.*, 1977; Sanford and Dally, 1979) and DIC (McNeill *et al.*, 1987; Abanto-Bueno and Lambros, 2006a, 2006b), and moiré methods (Kmiec, 1994). In this work, the technique will be employed using either images taken in real time during a fatigue loading cycle, or during a small number of specific measurement cycles at lower loading frequency. In addition to demonstrating this technique in fatigue, the effects of field of view (*i.e.*, magnification and consequently resolution) and the number of terms included in the expression for crack tip displacements will also be investigated. The resulting values of stress intensity factor obtained through this method will be used in chapter 3 to investigate the phenomenon of crack closure.

Table 2.1. Chemical Composition of Grade 2 Titanium

Element	**Weight % (max)**
Titanium	Balance
Iron	0.3
Oxygen	0.25
Carbon	0.08
Nitrogen	0.03
Hydrogen	0.015
Residual Elements (each)	0.10
Residual Elements (total)	0.40

2.2 Material and Specimen Preparation

Commercially pure titanium (grade 2) was used for the experiments in chapters 2 and 3. It was obtained from McMaster-Carr in the form of a rolled plate with a thickness of 3.18 mm.

The chemical composition, as supplied by the manufacturer, is given in Table 2.1. From both ultrasonic testing and uniaxial tension tests, the modulus of elasticity and Poisson's ratio of this material were found to be 109 GPa and 0.33, respectively. By testing specimens of different orientations, the properties of elastic modulus and Poisson's ratio were found to be isotropic. A yield stress of 400 MPa was also determined from uniaxial tension tests. Microscopy on etched specimens indicated an average grain size of roughly 10 μm.

A single edge-notched tension (SENT) specimen was cut from a plate of the grade 2 titanium using electrical discharge machining (EDM). Specimen dimensions were 150 mm x 6.33 mm x 3.10 mm (Fig. 2.4a). A 0.15 mm EDM wire was used to machine a 0.49 mm through-thickness edge notch in the specimen width. The specimen was rough polished using increasingly fine abrasive paper up to 800 grit. The natural texture of the specimen surface after rough polishing provided a suitable speckle pattern for DIC at all magnifications used; therefore, no speckle pattern was applied to the specimen surface. The resulting speckle pattern at each magnification is shown in Fig. 2.4b.

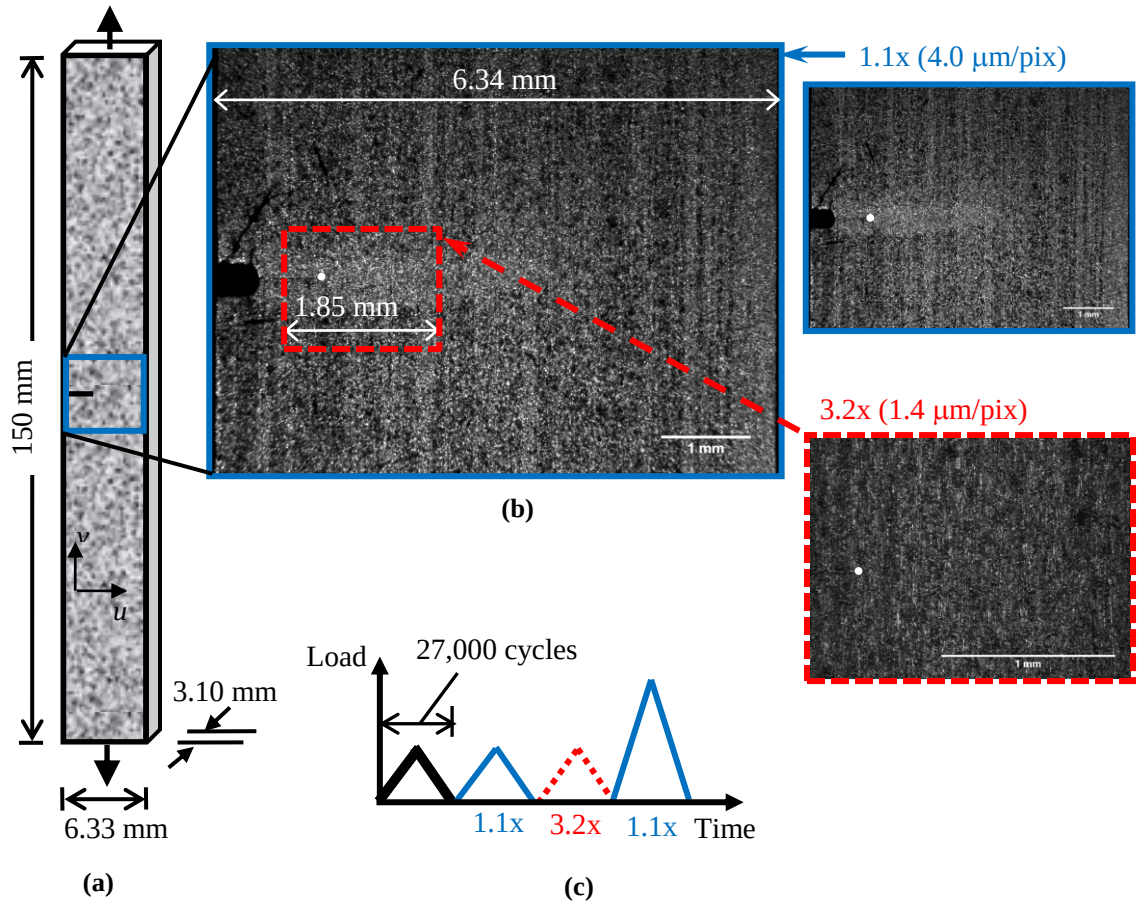

Fig. 2.4. (a) Specimen geometry and dimensions. This specimen had a notch length of 0.49 mm. (b) Field of view and resolution at each magnification level. The crack tip is shown as a white dot in the center set of images. Images are shown at the same size at the right to allow comparisons of speckle patterns. (c) Loading history. Data gathered from each magnification level was from a different cycle.

2.3 Experimental Setup

Using a servohydraulic load frame, the specimen was fatigue loaded (in load control) at constant load amplitude and a load ratio *R* (minimum load divided by maximum load) of roughly zero in order to initiate and grow a crack from the EDM notch tip. The fatigue crack was allowed to grow to a total length (notch plus fatigue crack) of 1.19 mm. The load was monitored so that the nominal stress intensity factor was relatively constant at 18 MPa√m.

After 28,000 cycles of crack growth at frequencies of 2-8Hz, fatigue loading was stopped and several "measurement" cycles were applied to the specimen at a much slower rate (0.008

Hz) so that a typical fatigue cycle could be studied in detail at different magnifications. A schematic of the load history and corresponding magnifications used is shown in Fig. 2.4c. In these measurement cycles, Labview software was used to control the load frame and precisely synchronize captured images with corresponding load levels. Crack growth rates during high frequency loading were on the order of 10^{-5} mm/cycle, so no significant crack growth is expected to take place during the measurement cycles. For comparison, if the threshold crack growth rate corresponds to approximately one Burger's vector per cycle (2×10^{-7} mm/cycle), then these experiments are two orders of magnitude above the threshold crack growth rate. While it would be preferable to perform this multiscale experiment with multiple cameras simultaneously viewing the specimen, it is nearly impossible to create such a setup due to limitations of depth of field and space limitations. Therefore, each magnification was studied on successive measurement cycles with the assumption that each cycle was basically equivalent. Experiments shown in later chapters will present results of real-time imaging being used, *i.e.*, without the use of measurements cycles done at lower frequency, but only one single magnification will be used each time.

As shown in Fig. 2.4, two magnifications were observed. At 1.1x (with a scale of 4.0 μm/pixel), the entire specimen width of 6.33 mm can be captured, while at 3.2x (1.4 μm/pixel), the field of view is 1.85 mm x 1.39 mm. Apart from the loading frequency, the two measurement cycles (1.1x and 3.2x), were equivalent to the last high frequency cycle such that the stress intensity factor cycled between 0 and 18 MPa√m. The 1.1x cycle was loaded at a rate of 120 seconds per cycle and 61 images were captured throughout this time. The 3.2x cycle was run at the same rate, but 121 images were captured. A Navitar 12x long working distance microscope lens was used in conjunction with an IMI Tech 202ft digital camera with a resolution of 1600 x

1200 pixels. In the final measurement cycle, the specimen was overloaded to a theoretical stress intensity factor of 30 MPa√m. During this 240-second cycle, 121 images were captured at 1.1x magnification,

DIC was performed on images from each of the measurement cycles using commercially available image correlation software (Vic2d from Correlated Solutions Inc.). The first image in the measurement cycle (at minimum load) was used as the reference image, and terms up to first order displacement gradients were used in all correlations. All of the images in each loading cycle were correlated giving at least 60 full-field measurements of displacements per cycle. The result of each image correlation is a measurement of the near-crack-tip displacement field at each load level. An example of such a field is the displacement field for the peak load image of the 1.1x measurement cycle shown in Fig. 2.5. In these plots, the crack tip is located at (0,0) and is indicated by a black dot. Typically, the rigid body motion is very large compared to motion due to material deformation. This is illustrated in Fig. 2.5a; the raw measurement of total displacement is shown as an arrow plot, in which the displacement field due to the crack opening is masked by the rigid translation of the specimen moving down and to the right when it was loaded. Rigid body motion was calculated (see section 2.3) and subtracted from the displacement field to give a clearer picture of the deformation related displacements (Fig 2.5b).

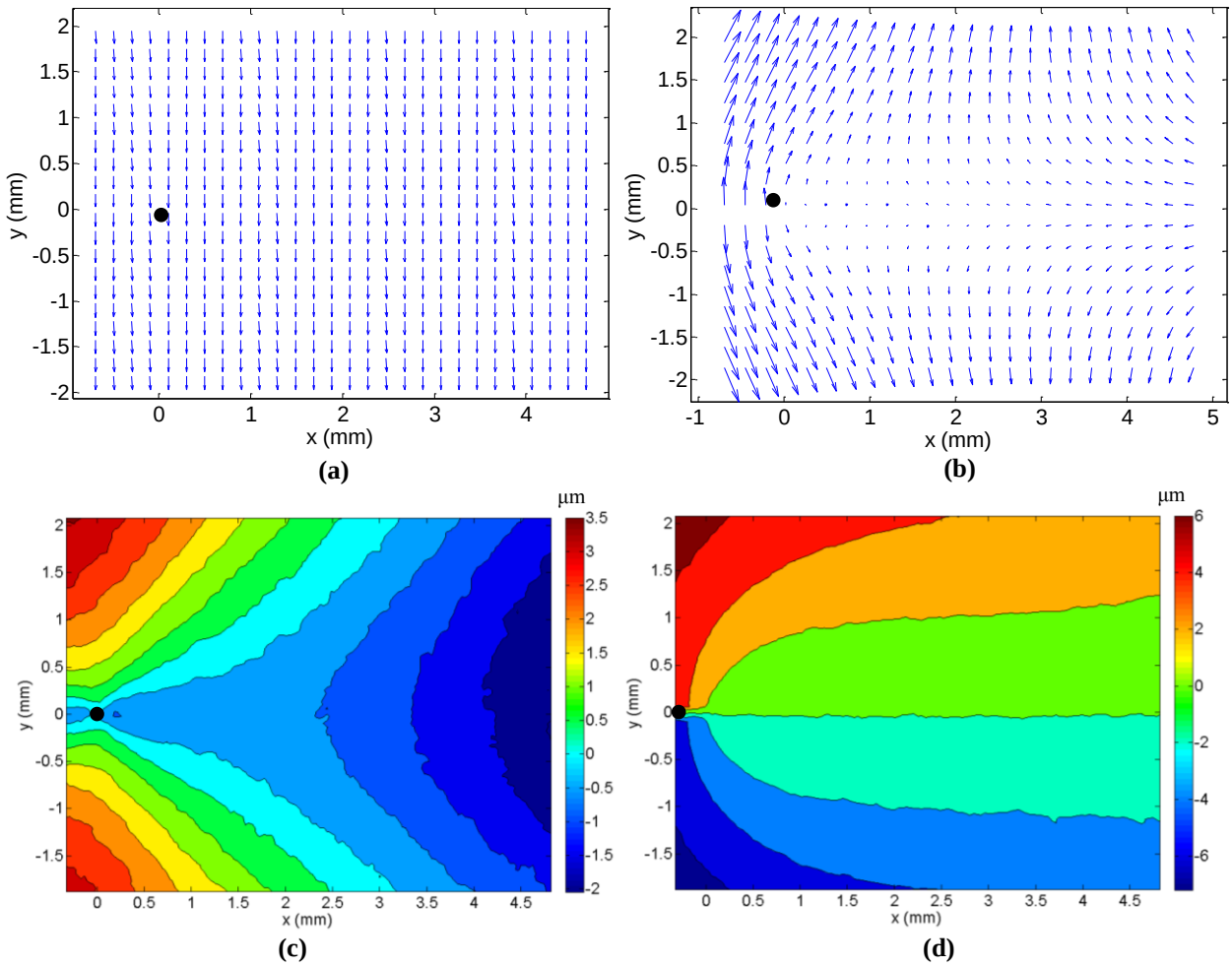

Fig. 2.5. Displacement field for 1.1x magnification at peak load. (a) Arrow plot of the raw displacement field (arrows shown at a scale of 1). (b) Arrow plot of the displacement field with rigid motion subtracted (arrows scaled by 20). (c) Contours of u displacement (µm). (d) Contours of v displacements (µm).

Contour plots of the horizontal and vertical components of displacement are shown in Figs 2.5c and 2.5d, respectively. A comparison of the color bars in Figs 2.5c and 2.5d, shows that *v* displacements (the displacement component perpendicular to the crack line) are larger than *u* displacements (parallel to the crack line) in mode I loading. In this work, a least squares regression using *v* displacements will be used to extract the mode I stress intensity factor since *v* displacements have a larger signal to noise ratio. Regression based on *u* displacements is commonly used in mixed mode conditions (Abanto-Bueno and Lambros, 2006a) where the magnitude of the *u* component of the deformation field is more significant.

2.4 Regression Analysis

The stress intensity factor, *K*, characterizes the stress, strain, and displacement fields near a crack tip in a linear elastic medium (Williams, 1957). For a single edge-notched tension specimen, K_I can be theoretically calculated assuming two-dimensional linear elasticity given the (monotonic) load and specimen geometry by:

$$K = F\sigma\sqrt{\pi a}, \tag{2.1}$$

where σ is the nominal stress and *a* is the crack length. The dimensionless function *F* is given by

$$F = 0.265(1-\alpha)^4 + \frac{0.857 + 0.265\alpha}{(1-\alpha)^{3/2}}.$$

with α being the ratio of crack length to the specimen width (Tada *et al.*, 1985). The value obtained by eq. 2.1 will be referred to as the theoretical stress intensity factor.

The stress, strain, and displacement fields near a crack tip are given by an infinite series of terms (Westergaard, 1939; Irwin, 1957; Williams, 1957; Eftis *et al.*, 1977). When the crack tip is approached, this series can be approximated by the most singular term of the asymptotic solution that only includes the *K* term, which is the first term in the series. While the stress and strain fields can be uniquely defined by this single term, the displacement field is not unique unless rigid body motion is also specified. Consequently, when using the displacement equations, it is necessary to consider three in-plane rigid motion terms. Rigid rotation, *A*, rigid translation parallel to the crack line, B_u, and rigid translation perpendicular to the crack line, B_v. When these terms are included, the asymptotic crack tip displacement equations become:

$$u = \frac{K_I}{\mu}\sqrt{\frac{r}{2\pi}}cos\left(\frac{\theta}{2}\right)\left[\tfrac{1}{2}(\kappa+1) - cos\left(\frac{\theta}{2}\right)\right] - Arsin(\theta) + B_u + H.O.T., \tag{2.2}$$

$$v = \frac{K_I}{\mu}\sqrt{\frac{r}{2\pi}}sin\left(\frac{\theta}{2}\right)\left[\tfrac{1}{2}(\kappa+1) - cos\left(\frac{\theta}{2}\right)\right] + Arcos(\theta) + B_v + H.O.T., \tag{2.3}$$

where u is the displacement component parallel to the crack line, v is the displacement component perpendicular to the crack line, r is the distance from the crack tip, θ is the angle from the crack line ahead of the tip, and μ is the shear modulus. The variable κ is given by:

$$\kappa = \begin{cases} \dfrac{3-\gamma}{1+\gamma} & \text{for plane stress} \\ 3-4\gamma & \text{for plane strain} \end{cases}$$

where γ is Poisson's ratio. The plane stress case is the most appropriate assumption for this work since all observations are on the surface of the specimen that is, by definition, in a state of plane stress. Even a significant proportion of the interior of the specimen is expected to be in a state of nearly plane stress since these specimens are relatively thin (ASTM E399, 2006).

By fitting the v displacement field of eq. 2.3 to the experimentally measured v displacement field (the vertical component of Fig. 2.5a) using least squares regression, the stress intensity factor, K_I, the rigid rotation, A, and the rigid translation, B_v, can be determined. This regression is referred to as the K regression as it accounts for the contribution to displacement of only the most singular term in the asymptotic expansion for stresses. This regression was performed on the DIC results from each image of the measurement cycles. The quality of the regression results can be assessed by comparing regression and experimental contours of displacement to one another. In Fig 2.6a, experimental v displacements are shown as blue solid contours along with the contours resulting from the linear regression (red dashed lines) for the peak load image of the 1.1x magnification cycle. The crack tip is located at (0, 0), and rigid body motion (A and B_v in eq. 2.3) has been subtracted from both fields. Because the zone of K-dominance would in part be dictated by the extent of the crack tip plastic zone (Irwin, 1957). , the plane stress plastic zone estimates are outlined in black in Fig. 2.6. The boundaries of the plastic zones were calculated using the Von Mises estimate based on regression K values.

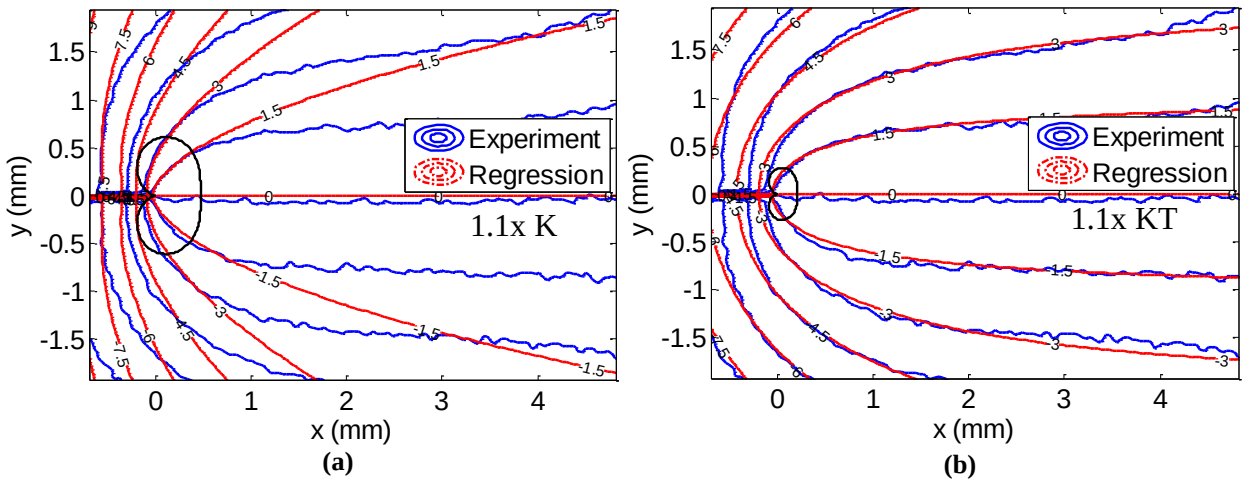

Fig. 2.6. Comparison of experimentally measured and regression *v*-displacement contours for (a) *K*-only regression and (b) *KT* regression. The thick solid gray contour represents the approximate Von-Mises plastic zone size. Magnification is 1.1x and contours are spaced by 1.5 µm.

In Fig. 2.6a, the experimental and regression contours agree near the crack tip, but they diverge beyond 1 mm from the crack tip. This can be explained by the fact that the *K* regression includes only the first term in the asymptotic expansion. Consequently, it can only capture the displacement field in the immediate vicinity of the crack tip where the *K* term dominates the displacement field. As the distance from the crack tip increases, higher order terms have increasing influence over displacements. In order to accurately fit experimental displacement contours further from the crack tip, it is therefore necessary to include higher order terms in the regression. The second term in the Williams expansion for stresses (Williams, 1957), and often the most influential after *K*, is the *T*-stress term. To account for the *T*-stress and its effects at larger distances from the crack tip, a second regression was performed. This regression, called the *KT* regression, includes a parameter for *T*-stress (*T*) in addition to the other three parameters used in the *K* regression. With *T*-stress added, eq. 2.2 and eq. 2.3 become:

$$u = \frac{K_I}{\mu}\sqrt{\frac{r}{2\pi}}cos\frac{\theta}{2}\left[\frac{1}{2}(\kappa+1) - cos\frac{\theta}{2}\right] + \frac{1}{2\mu(1+\nu)}Trcos\theta - Arsin\theta + B_u \quad (2.4)$$

$$v = \frac{K_I}{\mu}\sqrt{\frac{r}{2\pi}}sin\frac{\theta}{2}\left[\frac{1}{2}(\kappa+1) - cos\frac{\theta}{2}\right] - \frac{1}{2\mu}\left(\frac{\upsilon}{1+\nu}\right)Trsin\theta + Arcos\theta + B_v. \quad (2.5)$$

Note that eq. 2.4 and eq. 2.5 only apply for cases with small displacement gradients. For finite rotations, an additional term involving *A*rcos(θ) and *A*rsin(θ) should also be added to eq. 2.4 and eq. 2.5, respectively (Kmiec, 1994). For regression purposes, these terms have the same *r* and θ dependence as the *T*-stress terms. In that case, the contribution of rigid rotation would be combined with the value of *T*-stress obtained from the regression, and a second procedure would have to be followed to separate the two (Kmiec, 1994). However, by the author's analysis, the rigid rotation has been found to significantly contribute to the *T*-stress term only if the rigid rotation (coefficient *A* in eq. 2.4) exceeds 0.5 degrees. In the present effort, the calculated rotation never exceeds 10^{-4} degrees, and regression using eq. 2.4 will suffice.

The contours resulting from the *KT* regression at 1.1x magnification are shown in Fig. 2.6b. Including the *T*-stress term allows regression contours to match experimental contours much better at large distances from the crack tip, without affecting accuracy closer to the crack tip, where *K* dominates. When the field of view is restricted to only material close to the crack tip (*i.e.*, at higher magnifications), the effects of including *T*-stress are less pronounced. This is evident in Fig. 2.7, which compares results from the *K* and *KT* regressions at 3.2x magnification. At this higher magnification, the field of view is much closer to the crack tip so experimental and *K* regression contours match over a larger portion of the field of view (within 0.4 mm). Consequently, displacement contours at 3.2x are less affected by the addition of the *T*-stress term to the regression (Fig. 4b). This insensitivity to *T*-stress indicates that the majority of the 3.2x field of view is within the *K* dominant region.

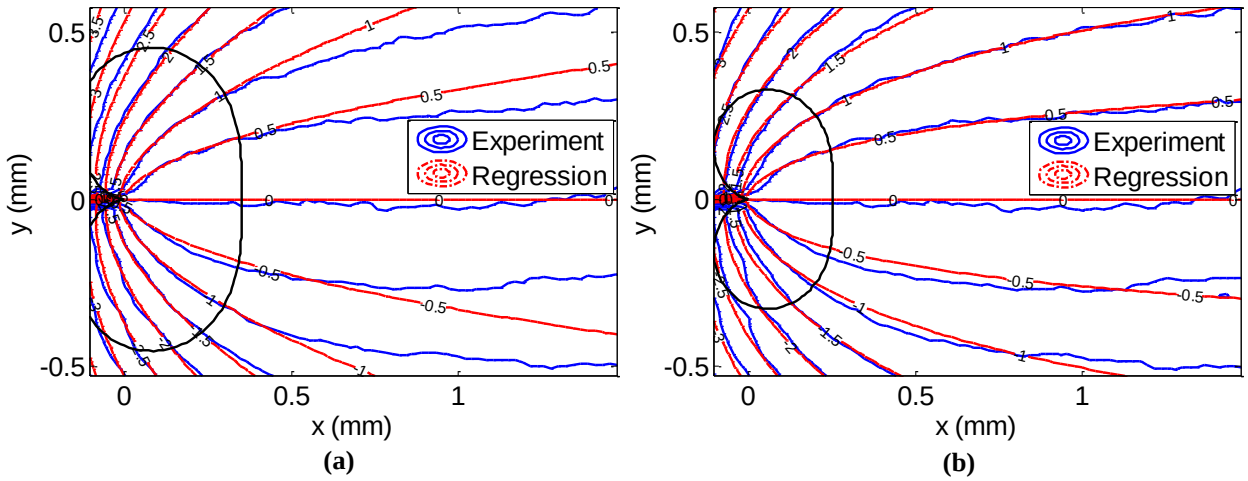

Fig. 2.7. Comparison of experimentally measured and regression *v*-displacement contours for (a) *K*-only regression and (b) *KT* regression. The thick solid gray contour represents the approximate Von-Mises plastic zone size. Magnification is 3.2x and contours are spaced by 1.5 µm.

Another interesting observation from the regression contours is that both the *K* and *KT* regressions appear to capture the displacement field very close to the tip. The regression equations shown here are elastic equations that contain a stress singularity at the crack tip. While stresses may not be captured very well by linear elastic fracture mechanics (LEFM), it is apparent that displacements can be described reasonably well by LEFM even within the plastic zone. In both Figs. 2.6 and 2.7, the plastic zone estimate is smaller for the *KT* regression than the *K* regression. This is because stress intensity factors measured from the *KT* regression are generally lower (and more accurate) than those predicted from the *K* regression. This results from the fact that the *K* regression tends to overestimate displacements far from the crack tip in these experiments.

2.5 Regression Results as a Function of Load

The regression process returns the values of *K*, *A*, B_v, and *T* that provide the best fit to experimental data. In fact, the motive for performing these regressions is to measure *K* values. Since the regression was performed on all of the images in each measurement cycle, the

measured stress intensity factor can be plotted against the load level within each cycle. A plot of regression *K* stress intensity factors vs. load throughout the 1.1x measurement cycle is shown in Fig. 2.8a for both the *K* and *KT* regressions. Because the shape of the *v* displacement contours at 1.1x was significantly altered by the inclusion of *T*-stress (Fig. 2.6), there is a correspondingly large difference in the stress intensity factor measured by the *K* and *KT* regressions. For comparison, the theoretical stress intensity factors calculated from eq. 2.1 are plotted as a solid black line. The *KT* regression results are closer to this line demonstrating the improved accuracy of including the *T*-stress. A similar comparison of regression *K* values from the 3.2x cycle is shown in Fig 2.8b. Since a large proportion of the data is within the *K* dominant region in the 3.2x field of view (Fig. 2.7), *T*-stress has less effect on regression *K* values.

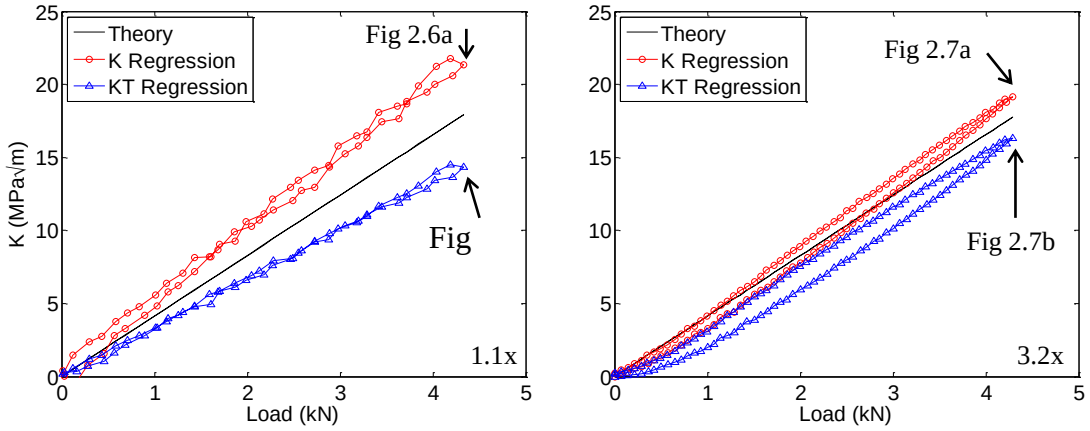

Fig. 2.8: Stress intensity factor vs. load for magnifications of a1.1x and b) 3.2x. Note that the 3.2x plot has some curvature at the bottom; this is due to crack closure.

At first glance, the *KT* regression may appear to "overcorrect" at both magnifications by giving a stress intensity factor below theoretical values. This is not necessarily the case for several reasons. First, it is possible that the crack tip location used in the regression analysis is inaccurate. Crack tip location has a substantial effect on the regression *K* value, and it is difficult to identify the crack tip very well. It is possible to perform the regression using several crack tip

locations to pinpoint the crack location more accurately or even to account for the Irwin plastic zone correction. This tedious process can provide limited improvement to regression results. If the crack tip is misidentified to be longer than the true crack length, the slope of the curves like those in Fig. 2.8 tends to be steeper than the theory line. On the other hand, if the crack tip is misidentified crack tip is shorter than reality, the curves become less steep. By observation of the overload experiment discussed later, crack tip identification is believed to be accurate in this case.

There are several reasons for differences between the theory and regression curves in Fig. 2.8 besides crack tip misidentification. Recall that the simple theoretical equation for stress intensity factor, eq. 2.1, does not capture plasticity effects because it is based on LEFM. Three dimensional effects are also not accounted for in this theory. Finally, the theoretical equation for stress intensity factor is for a monotonically loaded pre-existing crack while the crack being examined here is a fatigue crack. It is well known that fatigue cracks leave behind a wake of plastically deformed material that gives rise to crack closure (Elber, 1970, 1971). Crack closure lowers the effective stress intensity factor within the specimen by shielding the crack tip and lessening the intensity of displacement fields near the crack tip. Consequently, the regression analysis measures the *effective* stress intensity factor, which is not directly comparable to the theoretical stress intensity factor. As will be expounded in the next chapter of this thesis, crack closure causes curvature at the beginning of the K vs. load plot and making the effective stress intensity factor lower than theory would predict. In this experiment, the length of the fatigue crack was kept relatively short compared to the notch length to lessen crack closure effects, but crack closure still likely accounts for part of the discrepancy between theoretical and regression K values

While the primary purpose of including *T* is to improve the accuracy of the *K* value obtained by regression, it is nevertheless instructive to compare values of *T* obtained from this procedure to theoretical calculations based on load and geometry. Estimates of the biaxiality ratio, β, which relates the *T*-stress to the stress intensity factor, have been calculated for many geometries. From Anderson (1995), the biaxiality ratio for a single edge notched tension specimen with this geometry is -0.5. The *T*-stress can be calculated from the biaxiality ratio and the stress intensity factor by:

$$T = \frac{\beta K}{\sqrt{\pi a}}, \tag{2.6}$$

Given that the stress intensity factor at peak load (*i.e.*, in Figs. 2.5 through 2.7) is 18 MPa√m and the crack length is 1.19 mm, the theoretical *T*-stress is -147 MPa. The values of *T*-stress at peak load obtained by regression are -379 MPa and -214 MPa for the 1.1 and 3.2x measurement cycles, respectively. It is important to emphasize that the *T*-stress is not expected to agree well with theoretical values since its primary purpose is to improve the accuracy of the *K* value from regression. Nevertheless, it is somewhat reassuring that the regression *T*-stress values have the same sign and order of magnitude as theoretical calculations. Perhaps including the third term in the regression analysis would improve the agreement between regression and theoretical *T*-stress values. Even without further analysis, it is clear that the *T*-stress is on the order of -150 MPa for this experiment. This relatively large value of *T*-stress (in absolute terms) may explain why regression results changed so dramatically with the inclusion of *T*-stress. Stress intensity factors for specimen geometries with lower *T*-stress values could probably be accurately measured with the *K* regression.

Because the *KT* regression provides more accurate *K* values and a better fit to experimental data at all magnifications, the *KT* regression was used for the results shown in this

work. The effects of higher order terms in regression analyses on DIC data was investigated by McNeill et. al. (1987) in Plexiglas 3-point single edge notch bending specimens. Those authors found that up to 3-11 terms (in addition to rigid motion terms) were required to make regression *K* values converge depending on specimen geometry. However, a similar analysis performed for this work indicates that terms higher than *T*-stress have negligible effects on both regression contours and *K* values. Furthermore, the physical significance of higher order terms is questionable.

2.6 Overload Cycle

After four measurement cycles, the specimen was subjected to an overload cycle at 1.1x magnification up to a theoretical *K* value of 30 MPa√m (Fig. 2.4c). A plot of *K* vs. load for this cycle is shown in Fig 2.9a. The onset of large scale plasticity occurs when the regression curves turn upward to deviate from theoretical values (around 5 kN), and at that point the stress intensity factor K (inherently a linear elastic quantity) ceases to have physical meaning, although it can still be computed in the fashion described earlier. A comparison of *v* displacement contours for experiment and *KT* regression are plotted at peak load in Fig. 2.9b. Although the regression and experimental contours in front of the crack tip agree well in certain areas, the match between contours is poor behind the crack tip and far ahead of the crack tip. This illustrates the importance of considering the entire field of view before determining whether regression results are accurate. The *K* value determined from this peak load regression is 78 MPa√m, which is clearly incorrect and is far above the theoretical values shown in Fig. 2.9a (which peak at 30 MPa√m). Plasticity in the specimen is so large in this case that the boundary of the theoretical plane stress plastic zone is largely outside of the region of observation. As Fig 2.9c shows, the region of interest at this magnification (1.1x) is roughly the width of the

specimen. Therefore, the entire cross section of the specimen has presumably yielded. The peak load image of the 1.1x magnification cycle is shown in Fig. 2.9c. This image is digitally magnified in Fig. 2.9d to give a clearer picture of crack tip blunting. This amount of crack tip plasticity was large enough that, the crack tip remained visibly open even after removal of the load.

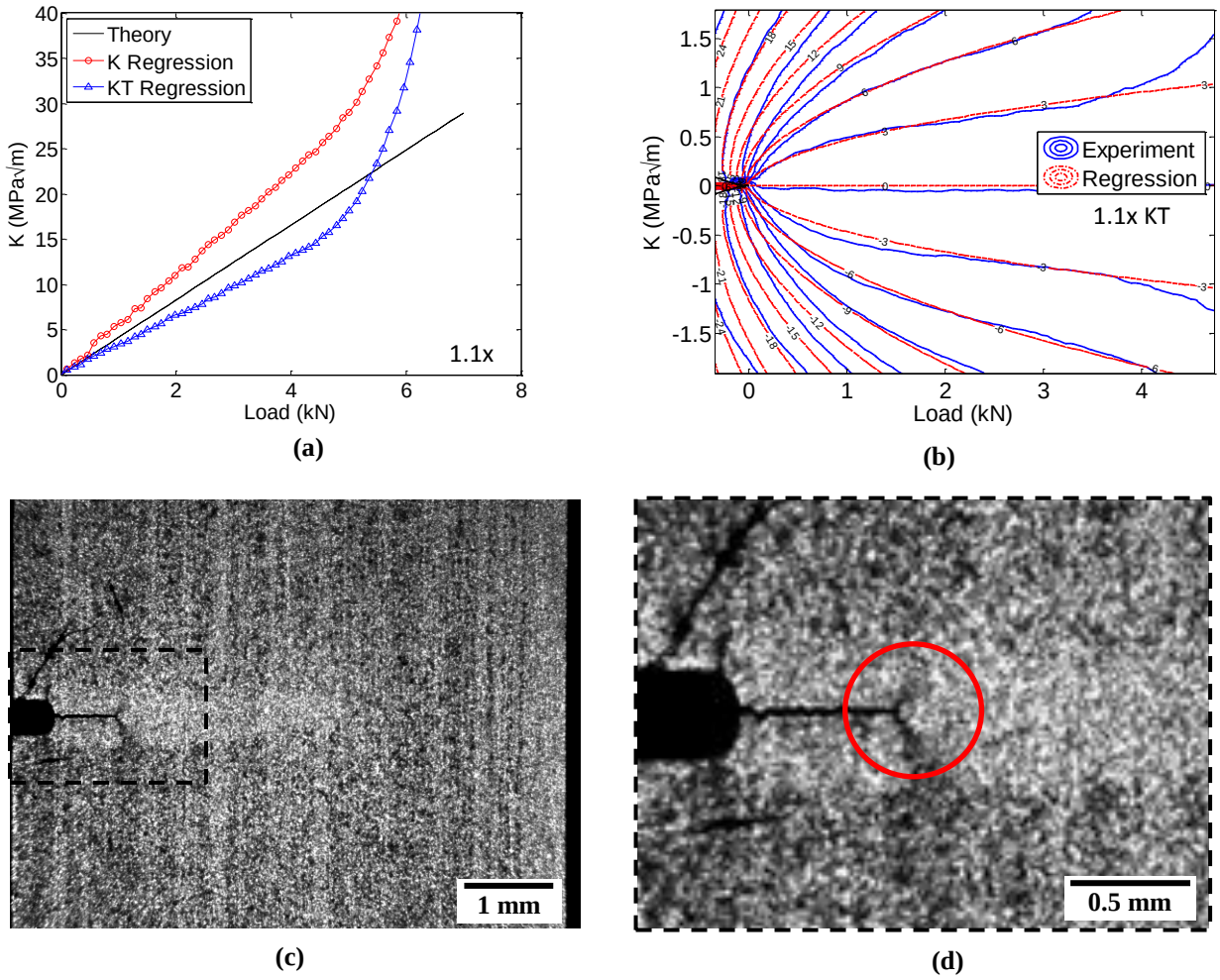

Fig. 2.9: (a) *K* vs. load plot for overload cycle at 1.1x magnification. The onset of large scale plasticity is around the load when the regression curves turn upwards. (b) Experimental and regression contours at peak load (7 kN). (c) Image of the specimen at peak load. The crack tip has blunted and will not close upon unloading. The black line above the notch is only a scratch on the surface, not a crack. (d) Digitally magnified image showing crack tip blunting (circled) at peak load.

2.7 Strain Fields

Up to this point, only displacement fields have been analyzed. DIC strain fields can also be obtained either directly from the DIC minimization or by differentiating the displacement field. In this case, the we employ the second approach. Taking the gradients of the displacement field shown in Fig. 2.5 can yield the strain field perpendicular to the crack line ε_{yy}, strain parallel to the crack line ε_{xx}, and the in-plane shear strain ε_{xy}. Contour plots of these three strain fields are shown in Figs. 2.10(a-c). The ε_{xx} and ε_{yy} plots in Figs. 2.10(a,b) illustrate well the typical strain field near a crack. There are two lobes emanating from the crack tip an angles between roughly ±(30° to 60°), which have tensile ε_{yy} strain, compressive ε_{xx} strain, and alternating shear strain. From these strain fields, other important fields can be calculated such as the Von Mises stress field shown in Fig. 2.10d. The Von Mises stress is calculated by:

$$\sigma_{mises} = \frac{1}{\sqrt{2}}\sqrt{(\sigma_{xx}-\sigma_{yy})^2+(\sigma_{yy}-\sigma_{zz})^2+(\sigma_{zz}-\sigma_{xx})^2+6(\sigma_{xy}{}^2+\sigma_{zx}{}^2+\sigma_{yz}{}^2)}\,. \qquad (2.7)$$

In eq. 2.7, the stresses are calculated from the constitutive equations and the σ_{zz}, σ_{zx}, and σ_{yz} terms are eliminated by the assumption of plane stress is. The Von Mises stress field at 1.1x magnification is shown in Fig. 2.10d. The yielded region is then identified as any point with a Von Mises stress higher than the yield stress of the material (σ_{yield} = 400 MPa for Ti). The crack tip plastic zone, calculated from experimental data using eq. 2.7, is outlined in black in Fig. 2.10d. This method was applied earlier to regression data to draw the yield zones on contour plots such as those in Fig. 2.6; however, this calculation uses experimental data instead of an assumed *K* field. The plastic zone in Fig. 2.10d extends roughly 0.7 mm above and below the crack tip. Even though this calculation of the yielded regions does not account for redistribution of stress within the plastic zone, it provides reasonable estimates of plastic zone size. The good agreement of experimental contours with the elastic *KT* solution in Figs. 2.6 and 2.7 very close to

the crack tip could be evidence that the true plastic zone size is smaller than the Von-Mises estimate. However, a more likely hypothesis is that deformation within the plastic zone is constrained by the surrounding elastic material and displacement contours cannot change very much in such small distances.

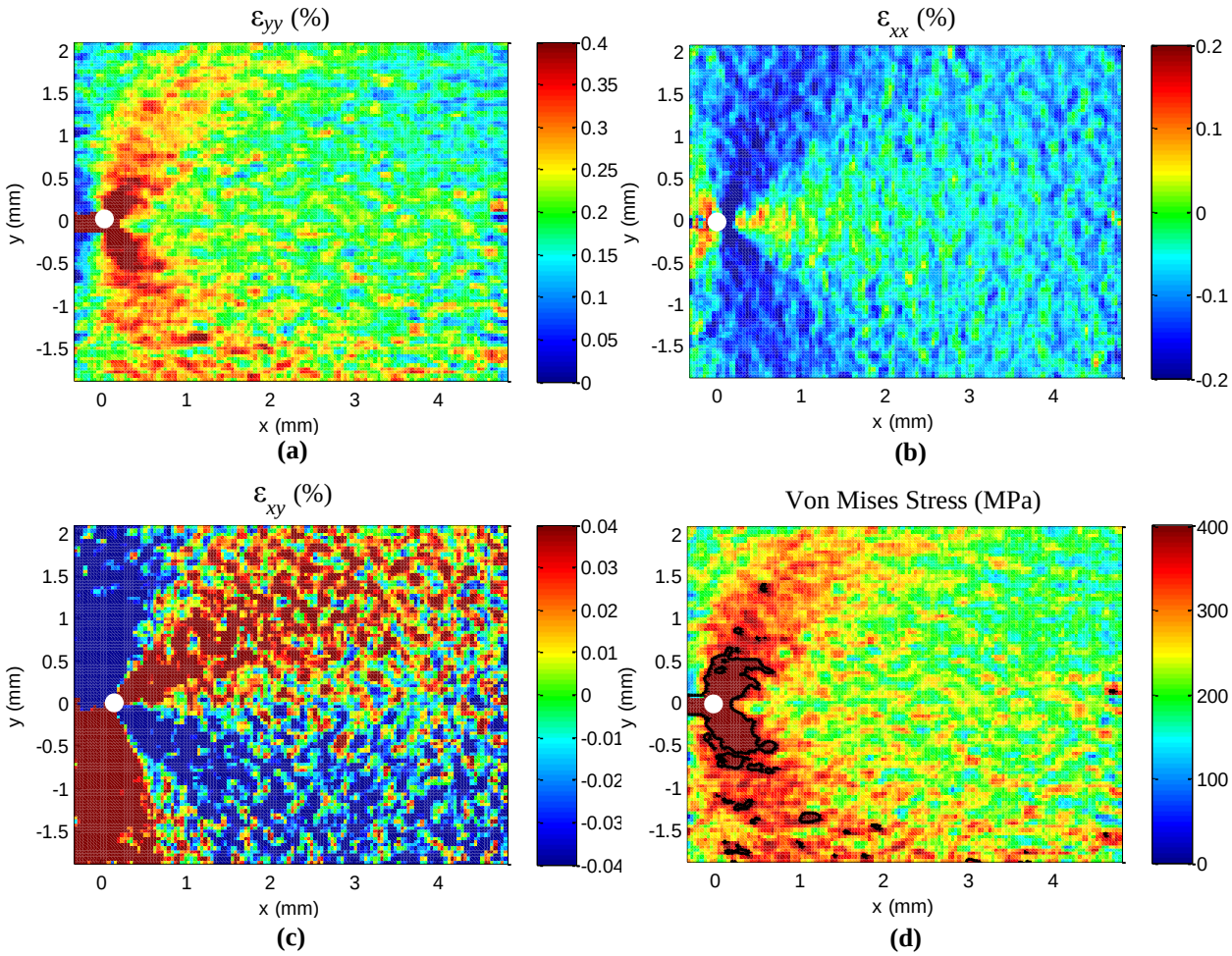

Fig. 2.10. Stress and strain fields near the crack tip. (a) ε_{yy} (b) ε_{xx} (c) ε_{xy} (d) Von Mises stress. The crack tip is indicated by a white dot.

A least squares regression can be performed on *strain* fields to measure the stress intensity factor. This would have the benefit of not requiring rigid body motion terms, but regressions using strain fields are generally less accurate than those using displacement fields because of the added noise, clearly visible in Fig. 2.10(a-c) generated by the differentiation of the displacement field.

2.8 Summary

Two types of DIC fatigue strain measurements will be shown in this thesis: the details of strain accumulation in a single cycle is studied by capturing images *within* a single cycle, but capturing images *between* multiple cycles gives measurements of fatigue strain accumulation over time.

A method was demonstrated for extracting stress intensity factor measurements from DIC displacement fields. The importance of *T*-stress was found to be crucial for obtaining accurate measurements of stress intensity factor for this geometry (as was also seen in Abanto-Bueno and Lambros, 2005, and Anderson 1995). *T*-stress values themselves were found to be on the same order of magnitude as theoretical calculations. The field of view used in obtaining data for the regression technique, which changes with magnification, was found to play an important role since the amount of data within the plastic zone, and within the *K* dominant region, can affect the values of *K* returned by the regression.

Chapter 3: Multiscale Study of Fatigue Crack Closure using DIC[2]

3.1 Background

It is widely accepted that precise knowledge concerning failure mechanisms allows designers to use increasingly aggressive structural designs. The safe life design paradigm is no longer acceptable for many applications since it leads to conservative designs that are too heavy, exhibit poor performance, and/or require excessive maintenance. Modern aviation requirements have necessitated a damage tolerant design approach wherein a structure is designed to withstand a certain amount of damage without failure. Such an approach strongly depends on accurate predictions of fatigue crack growth rates. In the 1960s, Paris and Erdogan (1963) and McEvily and Boettner (1963) related the fatigue crack growth rate, *da/dN* to the stress intensity factor range, ΔK, through the Paris relationship:

$$\frac{da}{dN} = C(\Delta K)^m, \tag{3.1}$$

where *C* and *m* are empirical material and loading dependent constants. The advent of the servo-hydraulic load frame allowed McEvily and Boettner (1963) to conduct a large number of experiments necessary for validating the Paris relationship (eq. 3.1). The load ratio, *R* (minimum load divided by maximum load), was also found to have a major effect on crack growth rates.

In the early 1970s, Elber (1970, 1971) discovered the crack closure phenomenon. As a fatigue crack grows, it leaves behind a wake of plastically deformed material. This plastic

[2] This chapter closely follows a paper by Carroll *et al.*, 2009

deformation causes the crack flanks to come stay in contact throughout a significant portion of the fatigue cycle (*i.e.,* the crack does not open immediately above minimum load). The point at which the crack flanks separate upon opening is termed the crack opening load; likewise, the crack closure load is defined as the point at which the crack flanks make contact during unloading. Crack closure acts as a shielding mechanism that reduces the effective stress intensity factor range at the crack tip, thereby decreasing crack growth rates. Elber modified the Paris relationship to use only the portion of the stress intensity range above the crack opening level, ($\Delta K_{eff} = K_{max} - K_{open}$), as follows:

$$\frac{da}{dN} = C\left(\Delta K_{eff}\right)^{m}. \tag{3.2}$$

Using ΔK_{eff} largely eliminated the direct dependence of crack growth rate on the load ratio such that one parameter, ΔK_{eff}, could be used instead of two (K and R), thereby demonstrating that plasticity-induced crack closure was the mechanism responsible for the effect of *load ratio* on crack growth rates. Elber (1970, 1971) showed that crack opening would be accompanied by a change in specimen compliance (due to a configuration change when the crack opens). He found the load level corresponding to this compliance change by using a displacement gage 2 mm behind the crack tip to measure the relative displacement of the crack flanks. Since Elber's discovery, several other techniques have been developed for measuring crack closure. Some researchers use visual observations and/or replica techniques to determine closure levels (Sehitoglu, 1983, 1985). Other methods for measuring crack closure such as the electrical potential drop method, ultrasonic/acoustic methods, and the eddy current method have been used with limited success. Schijve (1988) provides a brief comparison of these and other methods.

Despite these newer techniques, using displacement gages to detect a compliance change remains the most popular method for finding crack closure levels. Back face strain gages, crack mouth gages, or clip gages anywhere on the specimen can be used (Allison *et al.*, 1988). Following the pioneering work of Elber (1970, 1971), displacement gages are typically placed across the crack faces within a few millimeters of the crack tip. These displacement gages need not physically contact the specimen. Non-contact displacement gages make it relatively easy to place many gages along the crack line so that the variation in local crack opening levels with distance from the crack tip can be observed. Macha *et al.* (1979) used laser interferometric displacement gages, which track indentation marks near the crack flanks, to measure local crack opening displacement along the crack length. Adams (1972) computed local crack closure strains by manually comparing micrographs and noting the displacements of markers near the crack flanks. In a very similar technique (although with a much higher degree of automation and accuracy), Digital Image Correlation (DIC) displacement gages were introduced by Riddell *et al*. (1999) and Sutton *et al.* (1999). These displacement gages use DIC to track two subsets, one on each crack flank, to measure the crack opening displacement. As the crack opens, the subsets move apart from each other and the crack opening displacement at the gage location is measured as the relative motion between the two subsets. This work uses DIC displacement gages on the crack flanks to measure both *local* and *crack tip* opening levels.

Although crack opening occurs gradually from the crack mouth to the crack tip, a single opening level must be defined to obtain a single value for ΔK_{eff}. The crack tip opening level is typically used since it is thought that crack growth cannot occur until the crack is fully open. However, it is difficult to precisely identify the crack tip opening level due to scatter in experimental measurements and the fact that crack opening is a continuous process. This

difficulty has spurred several analysis techniques of the load versus displacement curve to obtain ΔK_{eff} (Donald and Paris, 1999; Paris *et al.*, 1999, 2008). A review of seven of these analysis methods is given in Donald and Paris (1999) The partial closure model of Paris *et al.* (1999) appears to give slightly better results than other models under the circumstances considered by Donald and Paris, but with the amount of scatter in the measurements, a clearly superior model has yet to emerge.

Adding to the ambiguity is the fact that crack closure is three-dimensional in nature because of constraint condition variations (Chermahini *et al.*, 1989) (*i.e.,* plane stress on the surface versus plane strain in the specimen's interior). Budiansky and Hutchinson (1978) provided one of the first analytical studies of crack closure, and countless numerical models of the crack closure process have followed (Lalor and Sehitoglu, 1987; Fleck and Newman, 1988; Chermahini *et al.*, 1989; Sehitoglu and Sun, 1991). Numerical models have also been influential in the debate over the existence of plasticity-induced crack closure under plane strain conditions (Fleck and Newman, 1988; Sehitoglu and Sun, 1991). The three-dimensional aspect of crack closure was also studied by Riddell *et al.* (1999). By comparing a finite element analysis of crack closure to rate-calculated opening loads, the researchers showed that, for their specimens, crack tip closure levels on the interior of the specimen (which are lower than those on the surface of the specimen due to constraint effects) dominated the crack closure effect on fatigue crack growth. They argued that surface crack closure measurements at the crack tip overestimate the crack closure effect.

Further complicating the study of crack closure is the existence of multiple closure mechanisms. These mechanisms include plasticity-, roughness-, phase transformation-, viscous fluid-, and oxidation-induced crack closure (Suresh and Ritchie, 1984). Measured crack closure

levels are generally due to a combination of mechanisms. Since the effects of different closure mechanisms could not be delineated in this work, the cited closure levels are most likely a combination of plasticity-induced and roughness-induced crack closure. However, plasticity is thought to be the primary closure mechanism in these experiments since, as will be seen later, very little shear motion of the crack faces is observed.

In summary, it is clear that crack closure is an extremely important effect that needs to be accounted for to predict crack growth rates accurately, but it is highly complicated in nature and dependent on the scale of observation – as the crack tip is approached, different amounts of local closure are observed. The objective of this chapter is to combine some of the techniques that have individually been used in the past in a *multiscale* framework that will allow experimentally linking measures of crack closure at locations close to and far from the crack tip. Specifically, full-field displacement measurements at the macroscale (order of mm) can be used to calculate the effective stress intensity factor range and, in turn, calculate closure levels. At the microscale, (order of μm) non-contact displacement gages can be used to quantify local and crack tip closure. The DIC technique, which does not possess an inherent length scale, is highly suitable for such multiscale experimentation and will facilitate direct linking between the scales. Section 3.2 of this chapter describes the experimental approach used to obtain measurements. In section 3.3, stress intensity factors are calculated through the procedure described in chapter 2 are used to obtain a full-field global measurement of crack closure values. Microscale measurements of crack closure are shown in section 3.4, and a multiscale comparison is discussed in section 3.5.

3.2 Experimental Procedure

The experiments shown in this chapter use the same material, specimen preparation, and experimental setup as the experiment in chapter 2 with minor modifications. Here, three

specimens were fatigue loaded at rates between 1 and 8 Hz to initiate and grow a crack from the EDM notch tip at the constant load amplitude and load ratio given in Table 3.1, which classifies the three experiments as having a "low", "medium", or "high" stress intensity factor. Since the load amplitude was kept constant, the stress intensity factor slowly increased throughout the crack growth process. After a period of fatigue crack growth, (see Table 3.1 for the number of crack growth cycles for each specimen), several measurement cycles were applied to the specimen at a much slower rate of 240 seconds per cycle allowing 120 images to be captured throughout the loading cycle. Except for frequency, measurement cycles were equivalent to the last high frequency cycle.

Table 3.1. Details of each crack closure experiment. Load ratio R is P_{min}/P_{max}.

Experiment	K_{max} (MPa√m)	*R*	Width (mm)	Thickness (mm)	Notch Length, c (mm)	Crack Length, *l* (mm)	*l/c*	Crack Growth Cycles
Low K	9.7	0.05	6.33	3.11	0.980	0.680	0.69	24,894
Medium K	15.4	0.05	6.34	3.10	0.969	0.906	0.93	15,752
High K	18.9	0	6.30	3.12	1.374	0.351	0.26	2,753

An IMI Rhein series digital camera with a resolution of 1600 by 1200 pixels was used to capture images throughout the measurement cycles. Optical magnifications from 1.1x to 28x (3.8 to 0.17 μm/pixel, respectively) were achieved with a Navitar 12x long working distance microscope lens and a 2x adapter tube. As illustrated in Fig. 3.1c, each measurement cycle was viewed with a different magnification. The two "macroscopic" magnifications of 1.1x and 4.3x (3.8 and 1.1 μm/pixel, respectively) are comparable to the magnifications used in chapter two. Additionally, a "microscopic" magnification of 14x (0.33 μm/pixel) was also captured in these experiments. A comparison of the fields of view and speckle patterns at each of the magnifications is shown in Fig. 3.1(a,b). Using multiple cameras would allow images to be captured at multiple magnifications simultaneously within a single cycle (Abanto-Bueno and

Lambros, 2005). However, for simplicity, one camera was used with a different measurement cycle for each magnification (see Fig. 3.1c). The scales cited in Fig. 3.1b are approximate since several cycles were run at each magnification. The exact scale used in calculations was determined for each measurement cycle individually.

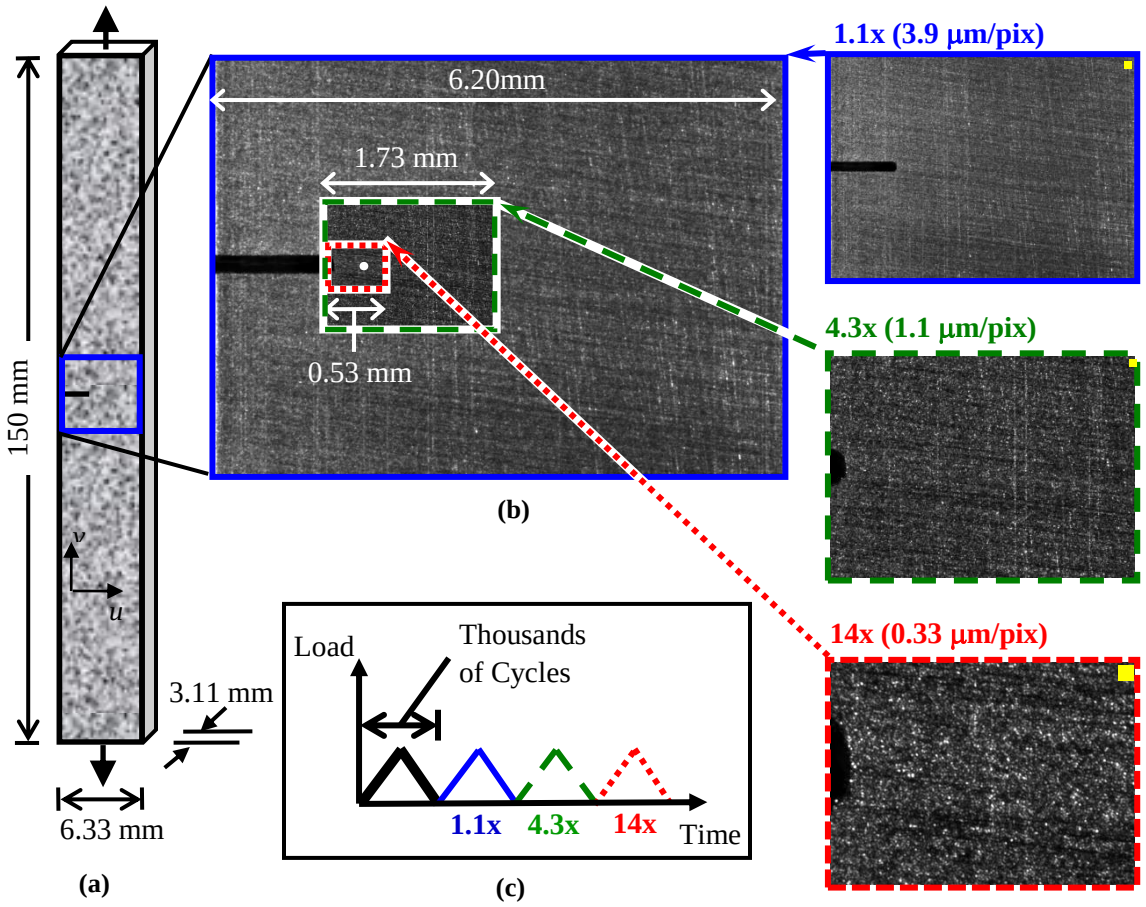

Fig. 3.1. (a) Specimen geometry and dimensions. (b) Field of view and resolution at each magnification level. The crack tip is shown as a white dot in the center set of images. Images are shown at the same size at the right to allow comparisons of speckle patterns. DIC subset sizes are shown by a square in the top right corner of each image. (c) Typical loading history. Data gathered from each magnification level was from a different cycle.

For loading cycles observed at the microscopic magnification (14x), DIC displacement gages spanning the crack faces (Riddell *et al.*, 1999; Sutton *et al.*, 1999) were used, as opposed to the full-field correlations used at the other two scales and described in chapter 2. Several gages were placed along the crack length as shown in Fig. 3.2, which is a 14x image of a fully

open crack at peak load. In Fig. 3.2, each gage is represented as a line connecting the centers of two DIC subsets (shown as boxes for the third gage from the crack tip). Subset sizes of 81 by 81 pixels were used corresponding to a gage width of 27 μm. A typical gage length, *i.e.*, distance between subsets above and below the crack, was 40 μm. Gages used in this work were placed from 10 μm *ahead* of the crack tip, where no opening is expected, to 700 μm *behind* the crack tip. For both of the macroscopic loading cycles (1.1x and 4.3x), DIC was used to obtain full-field displacements for each image throughout the cycle. Correlations were performed using a subset size of 41 by 41 pixels and a spacing of 15 pixels between subset centers.

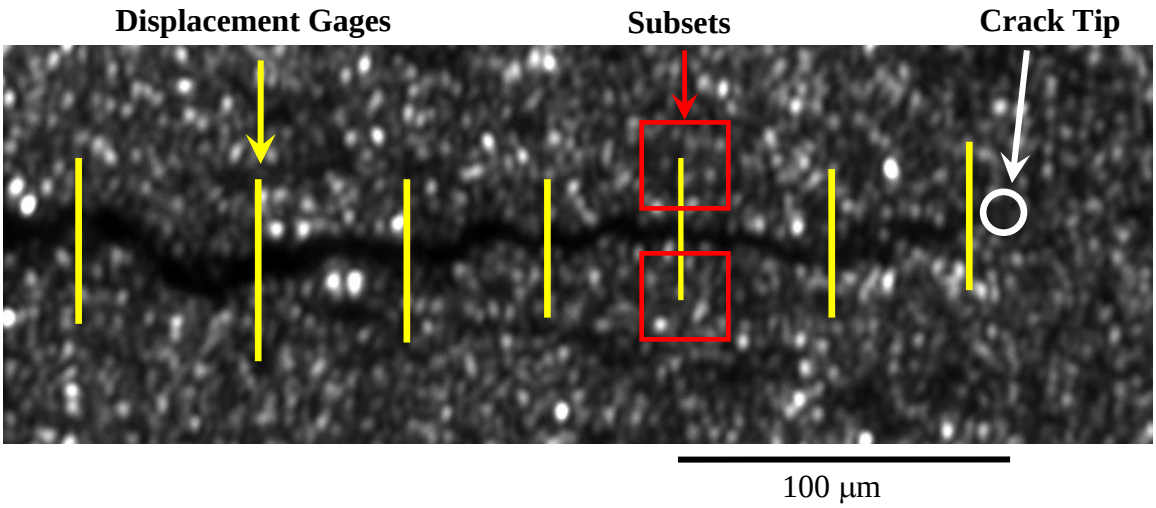

Fig. 3.2. Illustration of seven DIC displacement gages across open crack faces imaged at 14x. Each gage consists of two subsets—one on each of the crack flanks as illustrated for one gage. By measuring the difference in displacement of these two subsets, the opening and shear at each location can be determined.

Each measurement cycle was observed at a different magnification (*i.e.* the 1.1x images were captured over a different cycle than the 4.3x or the 14x images). All measurement cycles were within eight cycles of each other (some cycles are not discussed here). From our measurements of crack growth rates, the amount of crack growth throughout eight cycles was less than one pixel at 14x magnification, and no crack growth was observed during this small number of cycles. Therefore, the data from each measurement cycle are considered to be from

equivalent cycles and are assumed to be representative of previous fatigue cycles. After the measurement cycles, the specimen was held at peak load and photographed at an even higher magnification of 28x (0.17 μm/pixel). DIC was not performed on these images; rather the peak load images were simply inspected to identify the crack tip location accurately. Identifying the crack tip on a speckled surface can be difficult, and without an accurate estimate of the crack tip location, the error in these analyses becomes unacceptably large.

To investigate the effects of stress intensity range, notch length, and fatigue crack length on crack closure, three experiments were performed, each with a separate specimen. Each of these three specimens had slightly different geometry and loading (Table 3.1). Because the loading ratio, of each of the specimens was roughly zero, the stress intensity range calculated from theory (eq. 2.1), is roughly equivalent to the maximum stress intensity factor, K_{max}. The "low K", "medium K", and "high K" experiments had K_{max} values of 9.7, 15.4, and 18.9 MPa√m at the end of fatigue cracking. In each case, measurement cycles were performed under load control with the same load limits as the cycles used for fatigue cracking. Other details of each experiment such as specimen geometry, loading specifications, and the number of cycles of fatigue crack growth can also be found in Table 3.1.

3.3 Microscale Measurements (14x)

Gage displacement is defined here as the relative *vertical* displacement of the gage's two subsets ignoring in-plane shearing displacements. Shearing displacements (relative motion of the subsets parallel to the crack line) were found to be extremely small (less than one pixel), were about two orders of magnitude less than opening displacements, and were near the lower resolution limit of DIC. A load versus displacement plot, such as the one shown in Fig. 3.3, was created for each DIC displacement gage. Each data point in Fig. 3.3 represents the gage

displacement at a specified load level (one image per point) with the loading portion of the cycle represented by circles and the unloading portion by triangles.

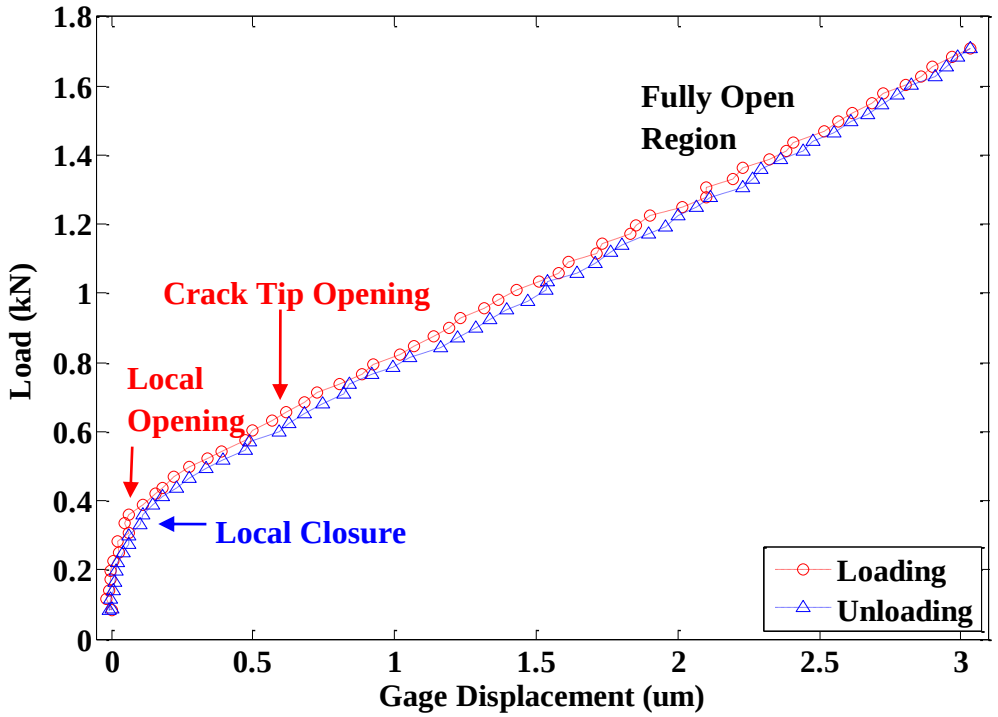

Fig. 3.3. Load versus displacement curve for a typical DIC displacement gage (Low K). Local opening levels are defined by the sharp knee in the curve while the compliance offset method is required to detect the more gradual compliance change caused by crack tip opening. Local closure values are found from the sharp knee of the unloading portion of the curve.

Elber noted that a change in slope of the load versus displacement curve represents a change in specimen compliance. He also showed that this compliance change must be due to crack opening and not other factors such as plasticity. When the specimen is first loaded, the gage displacement remains nearly zero indicating the crack is closed at this gage location. Any gage displacement in this low-load region is due to material strain between the gage points, not crack opening. As the crack opens at the gage location, the gage displacement begins to increase at a significant rate (this is the load denoted by the "local opening" arrow in Fig. 3.3). As the crack opens ahead of the gage, a gradual compliance change occurs until the crack is fully open up to the crack tip (see "crack tip opening" in Fig. 3.3). Because the crack is fully open, loading

the specimen further results in a linear relationship between load and gage displacement (no further compliance change), at least before large scale plasticity effects begin.

The *local* crack opening level is identified by the load at which the gage displacement begins to increase significantly. This load level is computed by fitting a straight line to the upper linear portion of the loading curve in Fig. 3.3 and visually determining where the gage displacement first deviates from this line. The *crack tip opening level* can also be identified from the load versus displacement curve, but is more difficult to do so since it usually induces a more gradual compliance change. The ASTM compliance offset method (described in detail later in this section) is used to identify the end of this gradual compliance change. The local closing load can be determined similarly to the local opening load; however, the crack tip closure load cannot be determined from this method since reverse plasticity affects the apparent compliance change upon unloading.

Load versus displacement curves for several gages along the crack length illustrate how local crack opening loads vary with position. Fig. 3.4 (a,b,c) show load versus gage displacement curves for three different gages (in the low K experiment). These three gages are located (a) 665μm (b) 236 μm and (c) 64 μm behind the crack tip. Note that the stiffness increases and the local crack opening and closure levels increase as the crack tip is approached. This behavior is expected since cracks generally open first at the mouth and last at the crack tip.

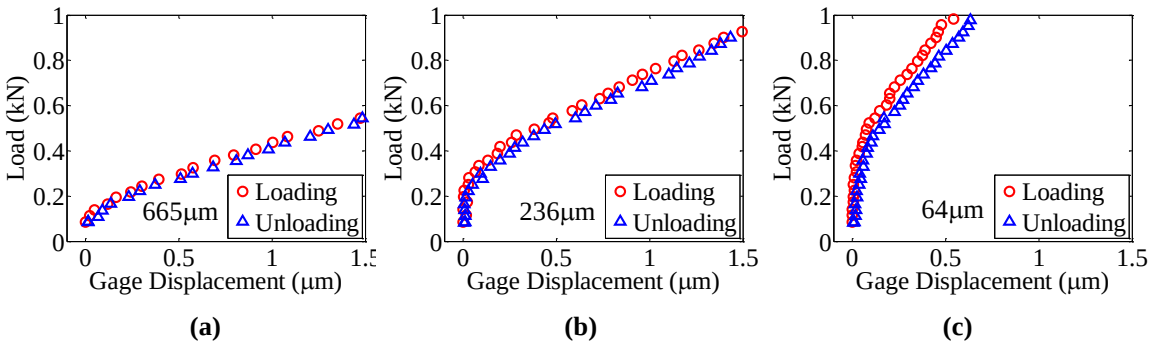

Fig. 3.4. Load versus displacement curves for (a) 665 μm, (b) 236 μm, and (c) 64 μm behind the crack tip. (Data from low *K* experiment). These plots only include the lower portion of the data to emphasize curvature due to crack closure.

Since several subsets were placed along the crack flanks, a visualization of the crack profile can be created by measuring the vertical displacement of each individual subset (not the gage displacement). Vertical subset displacements are plotted in Fig. 3.5 (with rigid translation subtracted) to show the shape of the crack profile at four different load levels within a typical fatigue cycle. This particular cycle is for the low *K* experiment, and the load level is shown as a percentage of peak load. Fig. 3.5 indicates that the majority of the crack (beyond 150 μm *behind* the crack tip) appears open by 18% of peak load, and the entire crack is fully open, to the extent imaged at the magnification used here, by 31% of peak load. The single gage on the right is about 10 μm *ahead* of the crack tip and, as expected, never appears open. These profile plots give a visual representation of the crack opening process, but it is important to note that the visual and mechanical crack tip opening do not necessarily coincide. It is the mechanical opening, as measured in Fig. 3.3, when the crack faces become truly traction free that determines ΔK_{eff}.

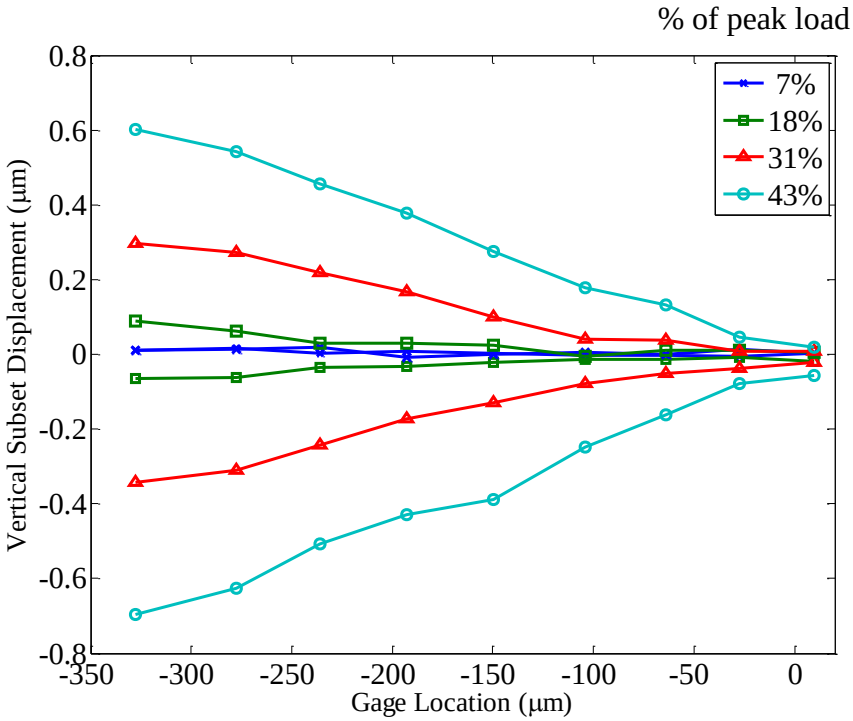

Fig. 3.5. Crack profiles constructed from vertical subset displacement measurements at 14x for several load levels of the low *K* experiment. The crack tip is located at 0 μm. Note that the single gage *ahead* of the crack tip never appears open.

While local crack opening measurements do provide insight as to the mechanics of crack opening and closure, an unambiguous measure of the crack opening level at the tip is ultimately necessary for using the modified Paris relationship (eq. 3.2). Elber (1970, 1971) showed that crack tip opening (and closure) results in a global compliance change that can, in theory, be measured with a gage at *any* location on the specimen—not just a gage on the crack flanks. In the load vs. displacement plot for each displacement gage along the crack line (*e.g.*, Fig. 3.3), the majority of the change in slope represents a local compliance change associated with local crack opening at the gage location. However, crack opening at any location causes a global compliance change that affects these plots. When the crack first starts to open near the mouth, each displacement gage should exhibit some slight compliance change (*i.e.*, curvature starts). Likewise, the load vs. displacement plots for each gage should not be perfectly linear until the crack is fully open (*i.e.*, curvature ends). Detecting the compliance change related to the crack tip

opening level is more difficult than detecting the local opening level since the compliance change associated with crack tip opening is less abrupt. Hence, a more rigorous method of identifying the compliance change is necessary to measure crack tip opening loads.

To this end, the compliance offset method outlined in appendix X2 of ASTM standard E647 (ASTM E647, 2005) was followed. For a detailed description of the procedure, the reader is referred to the ASTM standard; the method is briefly outlined below to provide specifics. A line is fit to the top linear portion of the unloading curve (the top 25% of the curve was used here) using least squares regression, and the inverse of this slope is defined as the compliance of the specimen with the fully open crack. The unloading slope is used in order to avoid any plasticity effects associated with loading. In a similar manner, lines are fit to fractions of the loading portion of the curve (in this case, a fit was made to 10% of the load range at intervals of 5% so that each line fit overlapped by 5% of the load range). The compliance at each of these load levels is found and compared to the unloading compliance. The load at which the compliance difference exceeds 4% is defined as the crack tip opening level.

Values of local and crack tip opening loads are plotted against gage position in Fig. 3.6(a-c) for the low, medium, and high K experiments, respectively. The horizontal axis represents the distance behind the crack tip while the vertical axis represents the opening or closure load, P, normalized by the peak load, P_{max}, expressed as a percentage. Local crack opening levels are shown as filled symbols while crack tip opening levels calculated from the ASTM compliance offset method are shown as crosses in Fig 3.6. As expected, local crack opening loads increase as the crack tip is approached (also observed by Riddell *et al.*, 1999). This rise is expected since cracks open at the crack mouth before the tip. On the other hand, crack tip opening levels are expected to be independent of gage location (Elber, 1970, 1971). In all three sets of results, a

slight increasing trend in crack tip opening load is observed as the crack tip is approached. This trend could be due to noise in experimental measurements, but a more likely scenario is that local crack opening is affecting the calculations of crack tip opening. Another possible cause for the rise in crack tip opening values is that, for gages closest to the crack tip (within 150 μm), plasticity effects may be interfering with measurements, even at low loads. In addition, the higher opening levels near the crack tip could be due to three-dimensional aspects of crack closure. Even with the many possible sources of error, crack tip opening levels can be reasonably identified with roughly ±5% accuracy. From Fig. 3.6, crack tip opening levels appear to be around 32%, 36%, and 24% for the low, medium, and high K experiments, respectively.

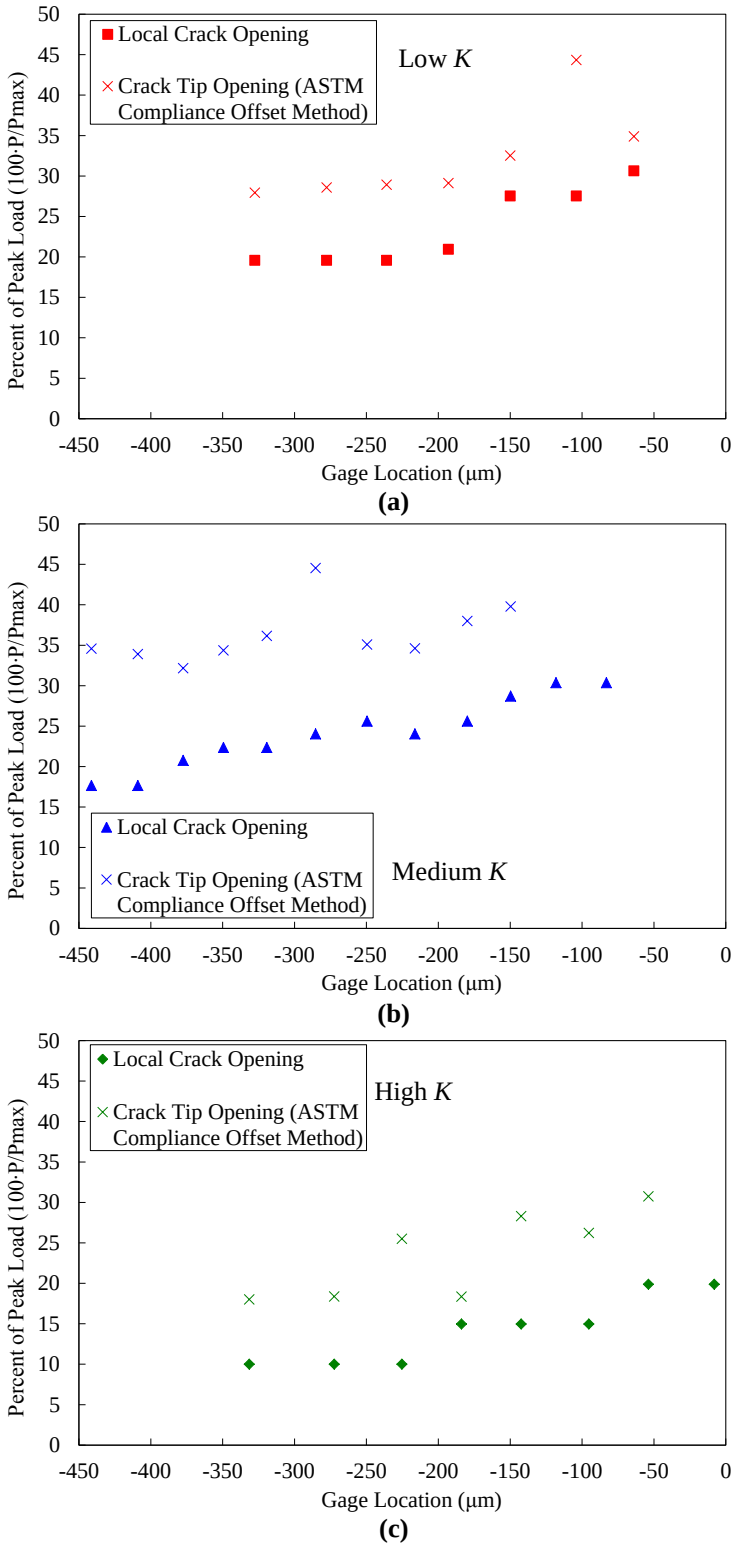

Fig. 3.6. Local crack opening levels and crack tip opening levels (determined from the compliance offset method) obtained from load versus displacement curves of several gages. The horizontal axis represents gage distance behind the crack tip. The vertical axis represents the percentage of the opening (or closure) load, P, divided by the peak load, P_{max}. (a) Low *K*, (b) Medium *K*, (c) High *K*.

Local crack opening and closure values determined from DIC displacement gages for all three load levels are compared in Fig. 3.7. The low, medium, and high *K* experiments are shown as squares, triangles, and diamonds, respectively. Filled symbols represent opening levels and empty symbols represent closure levels so that each pair of filled and empty symbols represents one displacement gage. Note that the data from the low *K* experiment cover a larger distance behind the crack tip because two 14x measurement cycles were performed for the low *K* experiment: one with the imaged area near the crack tip, and a second with the imaged area behind the crack tip by several hundred micrometers.

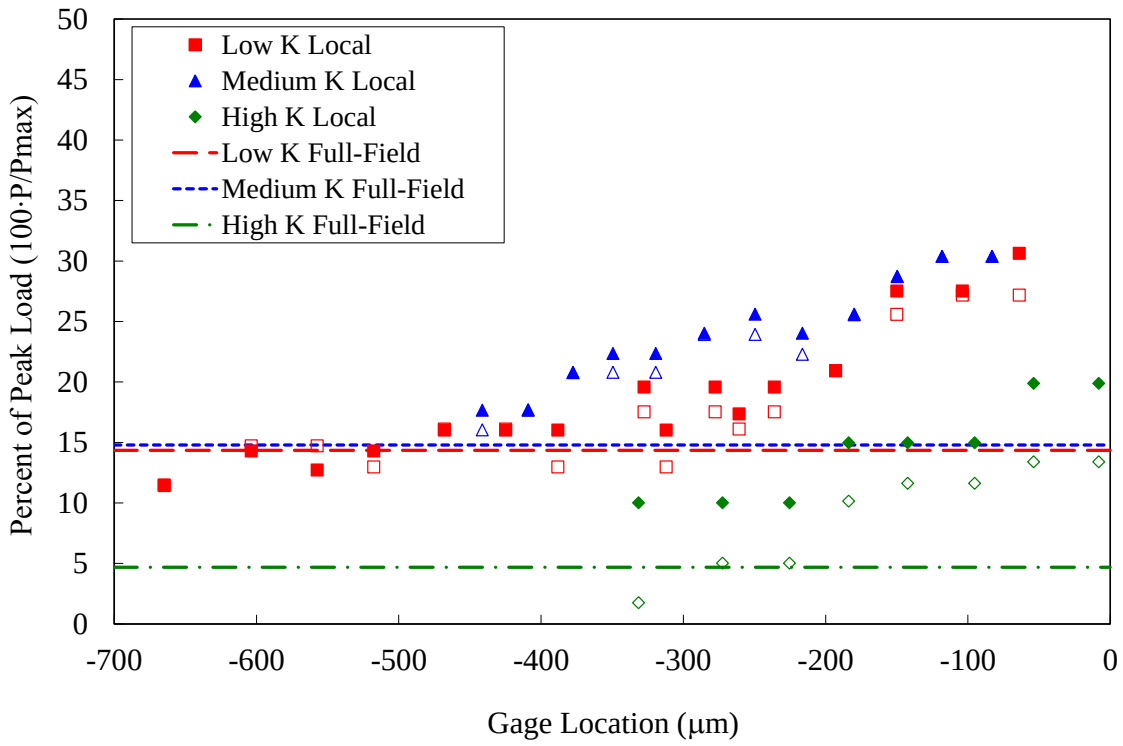

Fig. 3.7. Local opening and closure levels from the microscale measurements (points) and macroscale measurements (lines) for three different K_{max} values. 0 μm denotes the crack tip location. Symbols indicate displacement gage measurements while lines indicate measurements from the full-field effective *K* method. The horizontal axis represents gage distance behind the crack tip. The vertical axis represents the percentage of the opening (or closure) load, P, divided by the peak load, P_{max}.

In agreement with Macha *et al.* (1979) and Riddell *et al*. (1999), the local crack opening (and closure) levels for the low *K* experiment exhibit two regions. The first region is far behind

the crack tip (between 350 and 700 μm behind the tip) where closure levels remain constant. This implies that a large portion of the crack opens at roughly 16% of the peak load. This value agrees with estimates from the crack profile plot of Fig. 3.5 where the majority of the crack appeared open by 18% of the peak load. The second region of crack opening is near the crack tip (within 350 μm) where closure levels increase as the crack tip is approached. If local crack opening levels are extrapolated to the crack tip location, they can provide an estimate of the crack *tip* opening level. Extrapolating local low *K* opening values provides a crack tip opening estimate of 35% of the peak load. This value is in agreement, within experimental error, with crack profile observations in Fig. 3.5 (31%) and with the crack tip opening level calculated from the ASTM compliance offset method (Fig. 3.6). By extrapolating local crack opening measurements to the crack tip for all three experiments, opening levels at the crack tip are 35%, 34%, and 21% for the low, medium, and high *K* experiments, respectively. These values agree reasonably well with crack tip opening levels calculated from the ASTM compliance offset method reported earlier.

Limited crack closure data on grade 2 titanium exists with which to compare. However, Takao *et al.* (1985) used the electrical potential drop method and replica techniques on grade 2 titanium to obtain crack closure levels between 27% and 42% ($R = 0$). Measurements from gages closest to the crack tip for the low and medium *K* experiments are within this range. Measurements from the high *K* experiment are lower due to the short crack effect explained below.

In Fig. 3.7, it is clear that displacement gage measurements from the low and medium *K* experiments are close to one another. Therefore, no conclusions can be drawn concerning the effect of K_{max} on crack opening/closure levels as described in the literature (Shih and Wei, 1974).

By observing Fig. 3.7, it is evident that the opening/closure levels for the high *K* experiment are below the low and medium *K* experiment values. This is because the high *K* experiment has a lower crack-to-notch ratio, *l/c* (see Table 3.1). Since the notch surfaces never come into contact, only the fatigue crack contributes to the crack closure phenomenon. With a shorter fatigue crack in the high *K* experiment, there is less residually stressed material that contributes to crack closure; hence, the high *K* specimen exhibits lower closure levels. The effect of crack length on crack closure levels was previously observed by Sehitoglu (1985).

3.4 Macroscale Measurements (1.1x and 4.3x)

In the macroscale experiments, full-field displacements, such as those shown back in Fig. 2.5, were obtained from DIC. The *KT* regression procedure outlined in chapter 2 was applied to the v displacement field from DIC on each image throughout the measurement cycle. To check the validity of regression results, experimental and regression v displacement contours were compared for each image. An example of this is shown in Fig. 3.8, which compares contour plots resulting from the *K* and *KT* regressions at magnifications of 1.1x and 4.3x for the peak load image of the high *K* experiment. In agreement with results shown in chapter 2 (Figs. 2.3 and 2.4), the contour plots in Fig. 3.8 show better agreement using *KT* regression and less dependence on *T*-stress at higher magnification.

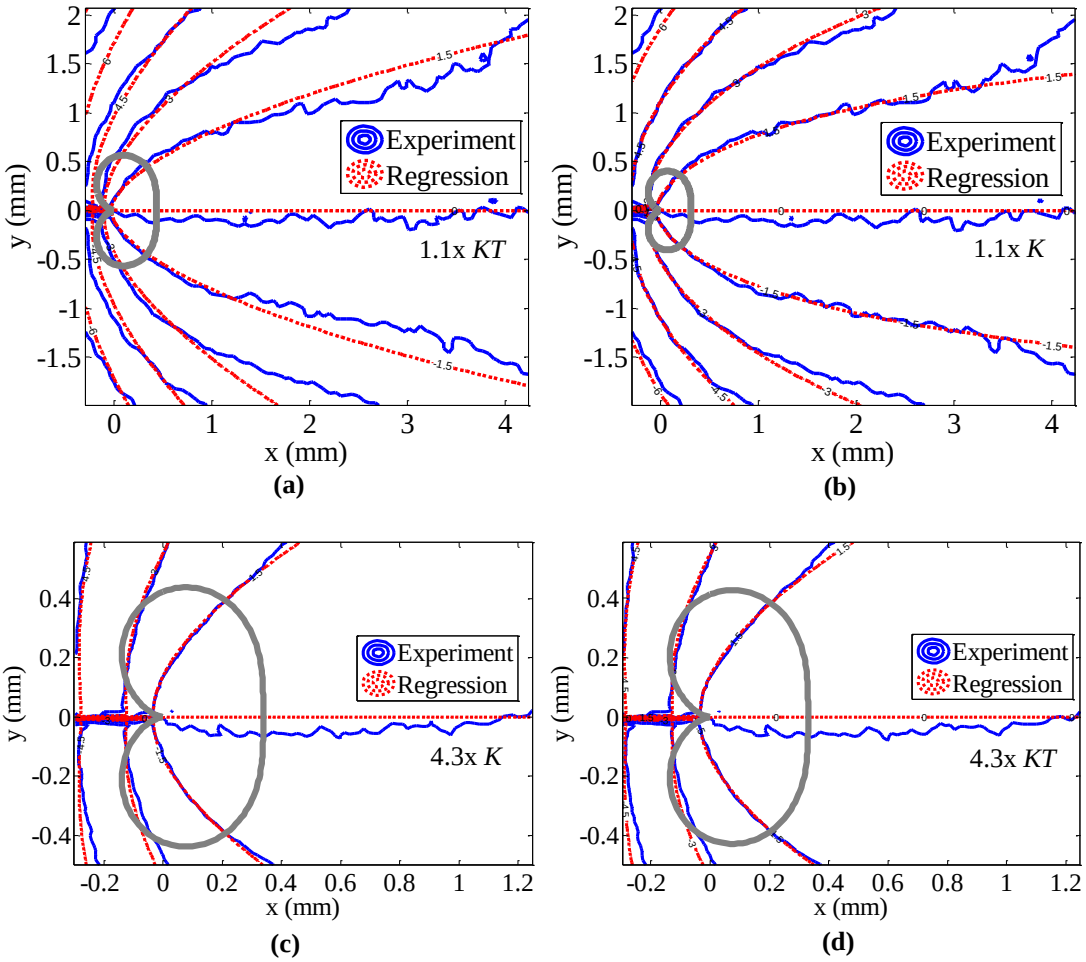

Fig. 3.8. Comparison of experimentally measured and regression *v*-displacement contours for (a) *K* regression at 1.1x, (b) *KT* regression at 1.1x, (c) *K* regression at 4.3x, (d) *KT* regression at 4.3x. The thick solid gray contour represents the approximate Von-Mises plastic zone size. Contour spacing is 1.5 μm.

Several researchers (McNeill *et al.*, 1987; Abanto-Bueno and Lambros, 2006) have performed regressions to obtain stress intensity factors; however, they did not perform such regressions in crack closure situations. Because the reference DIC image is taken at the minimum load of each measurement cycle (not necessarily at zero load), and because DIC measures the displacement of the specimen as a reaction to the applied load, the regression *K* value is actually the *effective change in stress intensity factor* (not simply the stress intensity factor) at each load. This effective change in stress intensity factor calculated from the *KT* regression will be referred to as ΔK_r. Results of ΔK_r are plotted against load throughout a typical

loading cycle in Fig. 3.9a as triangles. The load-based theoretical stress intensity factor from eq. 2.1, $K_{theory,}$ is also shown in Fig. 3.9a as a straight line passing through the origin. The experimental measurements lag behind the theoretical solution since they exhibit a region at low loading during which the effective stress intensity factor remains nearly zero. This is reminiscent of the response of individual displacement gages in the microscopic experiments, which showed little displacement with initial loading. The curve in Fig. 3.9b, which is the transpose of Fig. 3.9a, has a similar shape to the curve in Fig. 3.3 (load versus gage displacement). The similarity between these plots is due to the fact that ΔK_r is calculated through measurements of the displacement field. When the crack is closed, displacements change very little and the effective stress intensity factor remains near zero. Therefore, the curvature at the beginning of the ΔK_r curve is an indication of crack closure. Once the crack is completely open, ΔK_r increases linearly with load. This effect was also seen in elastic-plastic finite element simulations of crack closure by Zhao *et al.* (2004).

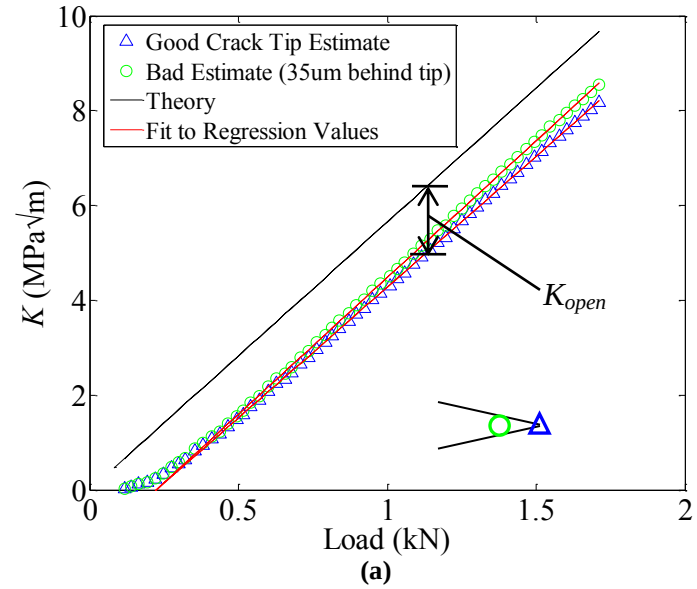

(a)

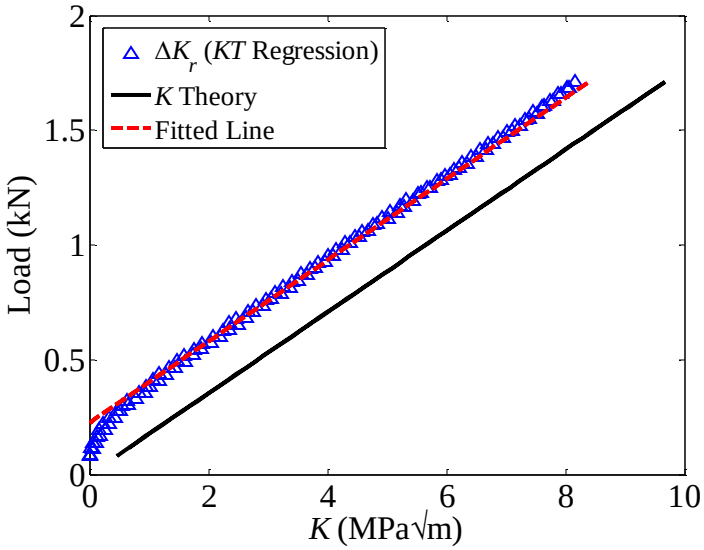

(b)

Fig. 3.9. (a) Finding K_{open} from full-field measurements. Since the value of K obtained from regression is the effective change in stress intensity factor, the opening stress intensity factor can be calculated by the difference between theoretical and regression values. Regression values are shown as triangles while the circles show the effect of making a bad guess for the crack tip location. The fit to each set of regression data illustrates that the main effect of a bad crack tip guess is a change in slope of the data. (b) The transpose of Fig. 10a illustrating the closure effect through a global specimen compliance change.

The effective stress intensity range, ΔK_{eff}, used in the modified Paris relationship, (eq. 3.2), is ideally just the maximum value of ΔK_r. However, as alluded to in chapter 2, a small amount of error in identifying the crack tip can have a pronounced effect on the slope of the

linear portion of ΔK_r so that taking the maximum value of ΔK_r can have significant uncertainty. To demonstrate this effect, a *KT* regression was performed using an intentionally bad estimate of crack tip location that was 35 μm behind the identified crack tip (a typical misidentification level). The results of this regression are shown in Fig. 3.9a. Lines were fit to the top half of the ΔK_r data for both cases of a correctly and an incorrectly identified crack tip. The slope corresponding to the correctly identified tip is noticeably closer to the slope of the theoretical line than the slope for the badly estimated crack tip data is.

In order to obtain results that are more reliable, and in order to compare these measurements to displacement gage crack closure measurements made earlier at the microscale, crack opening/closure levels are calculated from ΔK_r as follows: Elber (1970, 1971) defined the effective stress intensity range, ΔK_{eff} as the difference in the peak stress intensity factor, K_{max}, and the opening stress intensity factor such that

$$\Delta K_{eff} = K_{max} - K_{open}. \tag{3.3}$$

Since the crack is fully open throughout the linear portion of the ΔK_r versus load curve, the opening level can similarly be calculated at any load by the instantaneous difference in the load-based theoretical stress intensity factor and the change in stress intensity factor ΔK_r as follows:

$$K_{open} = K_{theory} - \Delta K_r. \tag{3.4}$$

It is posited that K_{theory} is the stress intensity factor that would be experienced by the specimen if closure effects were not present. The slope of the linear portion of the ΔK_r curve does not necessarily match the slope of the K_{theory} due to crack tip identification problems leading to a different calculated opening level value depending on the load at which it is calculated. Since this situation is only an artifact of the difficulty of crack tip identification, the opening stress intensity factor, K_{open}, was instead calculated by taking the difference between K_{theory} and a line

of the same slope fitted to the linear (fully open) portion of the ΔK_r experimental results as shown in Fig. 3.9a. The crack opening level can then be compared to displacement gage values by dividing K_{open} by the maximum stress intensity factor from theory, K_{max}. This method of finding crack closure levels using (eq. 3.4) will be referred to as the "*full-field effective K*" method. Each of the *K* vs. load plots used for this method gives one measurement of crack opening level.

Fig. 3.10 collects the ΔK_r results for each of the low, medium and high *K* experiments at the two different macroscale magnifications (1.1x and 4.3x), as available. A few observations may be made from this figure. First, the low and medium *K* experiments have regression values further below theory than the high *K* experiment, indicating less closure in the high *K* experiment. This is consistent with displacement gage observations (Fig. 3.7) of less crack closure in the high *K* experiment. Second, the high *K* regression data also show some hysteresis; this could be an indication of notch tip plasticity effects due to a very short fatigue crack and high loads. Third, the medium *K* regression data appear to be at a slightly different slope than the *K* values predicted by theory. As mentioned earlier, this effect is due to measurement error in identifying the crack tip. Identification of the crack tip is done at a magnification of 28x, but there is still some error in this measurement. The crack is not generally shorter than these measurements, but it could be up to 35 μm longer depending on how much of the crack is obscured by the speckle pattern. However, the averaging approach described earlier for computing K_{open} from such macroscopic results is more robust to crack tip position errors. Fourth, as Fig. 3.10(a,c) demonstrate, magnification level is shown to have negligible effect on stress intensity factor values, as long as a *KT* regression is used, although results from 4.3x magnification have less noise than results from 1.1x.

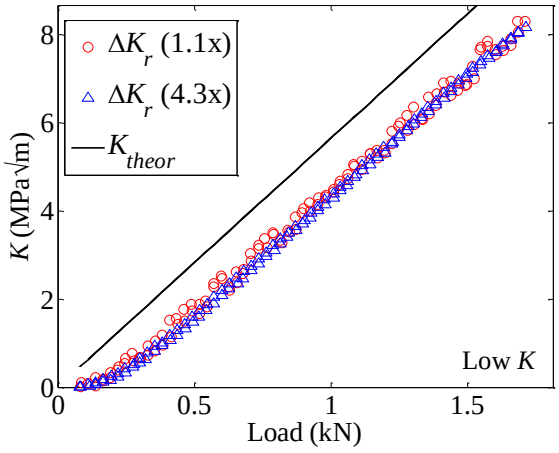

(a)

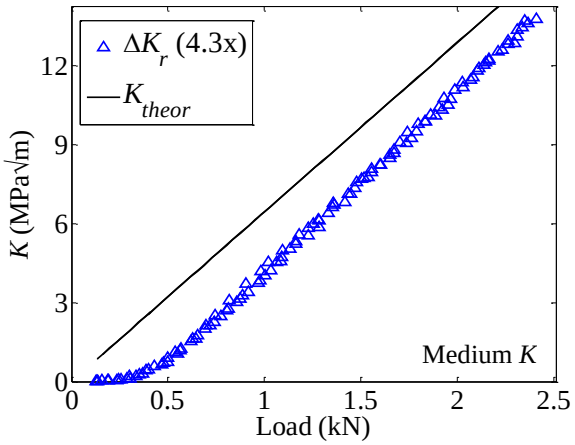

(b)

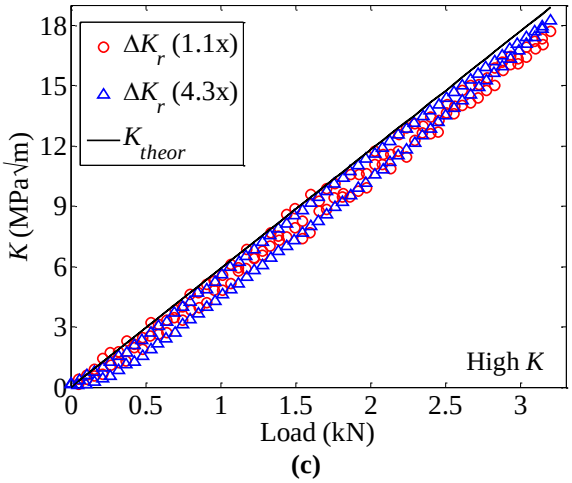

(c)

Fig. 3.10. *K* versus load plots for the (a) low *K*, (b) medium *K*, and (c) high *K* experiments. Results from two magnifications are shown (1.1x magnification images were not obtained for the medium *K* experiment).

3.5 Linking the Length Scales

At this point, two different DIC based methods for obtaining opening (and closure) load levels independently from macroscale and microscale experimentation have been described. Crack closure levels calculated from the macroscale full-field effective K method are shown as horizontal lines in Fig. 3.7 where they are compared to the microscale displacement gage results. Since the opening and closure values obtained through the macroscale method were very close to each other (due to the small hystereses in the ΔK_r versus load curves) the lines shown in Fig. 3.7 represent both opening and closure levels. The opening/closure levels computed with the full-field effective K method are 14%, 15%, and 5% of peak load for the low, medium, and high K experiments, respectively. For the low K experiment, full-field effective K closure levels agree with displacement gages far from the tip (in the region of constant opening level). The effective K method gives a measure of local crack opening far from the tip in the plateau region. It is believed that a measure of crack tip opening load could be estimated from full-field measurements. It appears from Fig. 3.7 that a similar agreement between the two methods is likely for the medium and high K experiments as well. Note, however, that in all three experiments, closure levels from the full-field effective K method are lower than almost all displacement gage measurements. Consequently, the full-field effective K method is more conservative since it would predict a higher crack growth rate by the modified Paris relationship shown in (eq. 3.2).

As mentioned earlier, the regression value of K is essentially a measure of displacement in the specimen, and the ΔK_r versus load curve behaved similarly to the load versus displacement curve (compare Figs. 3.3 and 3.9b). Since the slope of the ΔK_r versus load curve is similar to a compliance measurement, Elber's technique of defining crack closure through compliance

change can be applied to the ΔK_r versus load plots (Fig. 3.10) exactly as it was for the load versus displacement plots. The result is a *second full-field method* for measuring crack closure; this method will be referred to as the "full-field *K*-compliance method". This method was used to estimate crack tip opening levels by adapting the ASTM compliance offset technique to use the (global) load versus *K* curve instead of the (local) load versus displacement curves of each gage.

The results of this technique performed on the full-field data at 4.3x are compared to results of the other two methods (DIC displacement gages and full-field effective *K* method) in Fig. 3.11(a,b,c) for the low, medium, and high *K* experiments, respectively. Crack opening values obtained from the full-field *K*-compliance method (at 4.3x) are higher than the other full-field method (effective *K* method) and closer to crack tip opening levels calculated from the microscale displacement gage method. This is in contrast to the full-field effective *K* method that gives opening levels that are more representative of local values far from the crack tip. Analyzing the DIC displacement field as if it was a displacement gage gives results that represent an average of the local opening levels within the imaged region. Thus, the full-field *K*-compliance method can be thought of in some sense as providing average local crack opening levels using a larger, full-field displacement gage. Consequently, this method gives crack opening values slightly below what are thought to be crack tip opening levels due to effects of averaging over the correlation region.

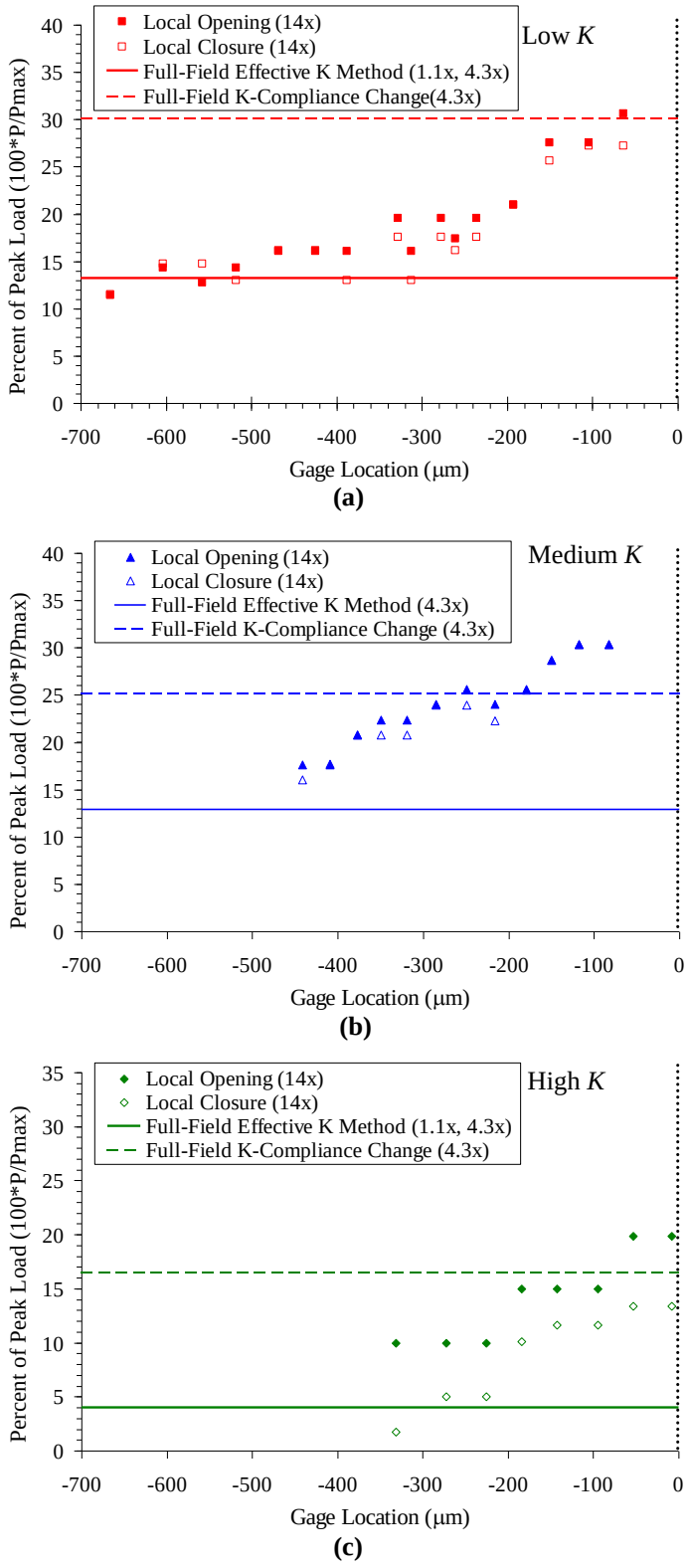

Fig. 3.11. Crack opening levels from the full-field *K*-compliance method and the full-field effective *K* method with local displacement gage results for comparison. (a) low *K*, (b) medium *K*, (c) high *K*. The horizontal axis represents gage distance behind the crack tip. The vertical axis represents the percentage of the opening (or closure) load, P, divided by the peak load, P_{max}.

3.6 Summary

Two full-field DIC methods for measuring crack closure levels during fatigue crack growth in titanium were introduced and compared to a DIC based displacement gage method. Results from the three techniques were compared for low, medium and high K experiments (with maximum K values of 9.7 MPa√m (with R = 0.05), 15.4 MPa√m (with R = 0.05), and 18.9 MPa√m (with $R \approx 0$), respectively). Crack opening levels calculated from the full-field effective K method agree with displacement gage closure levels far from the crack tip in the constant opening level region. The second full-field method, the full-field K-compliance method, gives crack opening levels that are an average of local values over the correlated region and are closer to crack tip opening levels. The use of these full-field methods would allow effective stress intensity factors to be measured on a full-field basis circumventing some of the drawbacks of placing displacement in contact with the sample near the crack tip.

A comparison of the low and medium K experiments indicates there could be some small influence of the maximum stress intensity factor as described in Shih and Wei (1974); however, the current experiments are inconclusive in this regard. The ratio of fatigue crack length to notch length was found to affect crack closure levels, confirming the results of Sehitoglu (1985). Displacement gage measurements of crack tip closure levels (35% and 34% for low and medium K experiments) agree with the limited published values for this material (27–42%) by Takao *et al.* (1985). In the high K experiment (ΔK = 18.9 MPa√m), the crack tip opening level was around 21%, somewhat lower than the other experiments due to the short crack effect.

At this time, it is unclear how to predict crack growth rates from the full-field measurements of crack closure presented here. An extensive testing program could help shed light on this issue but is beyond the scope of this work. The focus here is to introduce full-field crack closure measurement techniques and to use a multiscale experimental approach to compare

closure levels obtained through microscale and macroscale experiments on the same sample. The full-field crack closure techniques demonstrated here use lower magnification images than the DIC displacement gage technique (in this case, 1.1x compared to 14x). Since high quality, high magnification images for DIC can be difficult to obtain, these full-field techniques could be a valuable, easier method for estimating closure levels. This could be of great use in many engineering applications where obtaining approximate answers with less effort is desired.

Chapter 4: High Magnification *In situ* Fatigue Crack Growth Measurements

A large part of this thesis is focused on multiscale measurements of strain with DIC. As mentioned earlier, the subset size controls the spatial resolution of DIC measurements. Consequently, the relative size of the subsets and the grains in the material is a crucial factor in determining whether grain level measurements can be obtained. At low magnifications and/or small grain sizes, subset sizes are several times the grain size. This is illustrated in Fig. 4.1a in which the subset size at 14x magnification (used in the work presented in this chapter) is drawn as a red box on top of a micrograph of the etched material. Consequently, macroscale DIC results are obtained in such experiments. For grain level experiments, the subset size must be smaller than the grain size as illustrated in Fig. 4.1b. In this chapter, the results from an experiment using large grain titanium will be shown. As shown in Fig. 4.1b, the subset size at 14x magnification used in this work is half of the grain diameter, allowing for grain level DIC measurements. Valuable information is gained from both macroscale and microscale strain measurements, and the fatigue crack growth process will be examined at both of these scales in this and subsequent chapters.

Results from two multiscale experimental set-ups are discussed in this chapter. The first, involves fatigue crack growth in large grain titanium, and demonstrates the interplay between crack closure, fatigue crack growth, and microstructure at the grain level. In the second experimental set-up, simultaneous DIC measurements of fatigue crack growth in Hastelloy X are

made at multiple length scales to exploit the improved spatial resolution in DIC measurements that results from increased magnification.

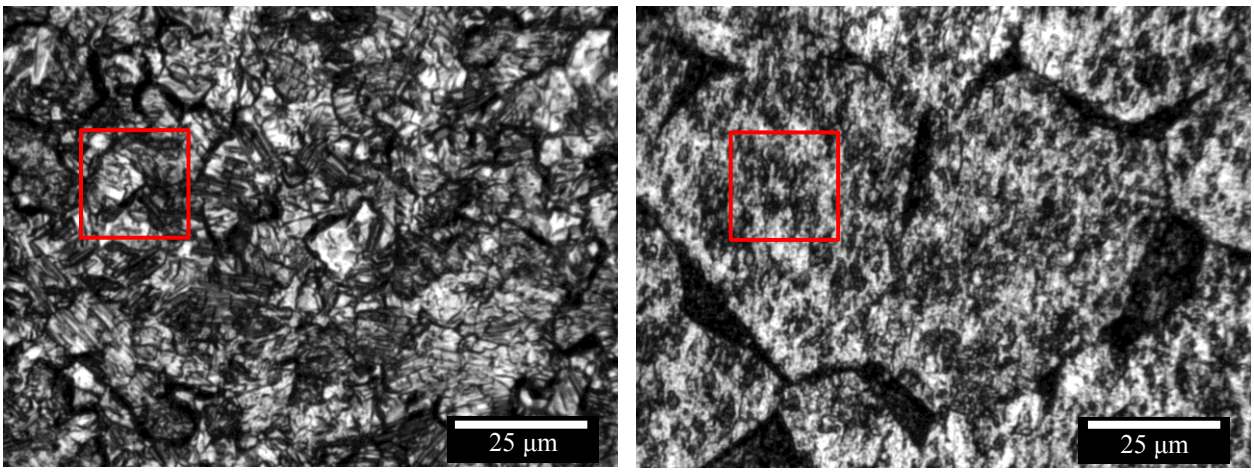

(a) **(b)**

Fig. 4.1. Grain level resolution of DIC measurements can only be achieved if the subset size is smaller than the grain size. (a) The 14x subset size shown here is several times the grain size for as-received grade 2 titanium, but (b) it is less than one-half of the grain diameter for large grain titanium.

4.1 Linking Fatigue Strains to Microstructure in Large Grain Titanium

To obtain DIC measurements of strain fields during fatigue crack growth with grain level spatial resolution, a specimen made of grade 2 titanium with enlarged grains was used. This is the same material used by Efstathiou (2008) and Efstathiou *et al.* (2010) in their study of the representative volume element needed for plastic deformation. Here, a single edge notched tension specimen was machined to nominally the same dimensions as those in chapters 2 and 3. The specimen was then heated in an oven in an air environment at 850 °C for 24 hours and quenched in water. In this process, the grain diameter grew to an average of 50 μm, from 10 μm (Fig. 4.1). At the same time, however, the heat treatment process created an oxide layer on the specimen surfaces, including the exposed surfaces surrounding the notch. Since the goal of this test is to study large grain titanium, not titanium coated with titanium oxide, wire EDM was used to cut 0.5 mm from the front and back faces of the specimen thus eliminating the oxide but also reducing the specimen thickness by 1 mm. These cuts ensured that the entire oxide layer was

removed from the surface since the effective oxide layer thickness was less than 0.2 mm thick (shown later). However, the oxide layer that built up on the interior of the notch surfaces was not removed. The specimen was then polished and swab etched with Kroll's Reagent to reveal the microstructural geometry. The appearance of the etched specimen in the microscope is shown in Fig. 4.2, which shows the final fatigue crack path originating at the notch and terminating near the opposite end of the sample. The final specimen dimensions after removing the front and rear surface oxide layers were 145.9 mm by 6.17 mm by 2.46 mm with a through thickness notch of 0.912 mm. As mentioned above, since the notch was machined before heat treatment, an oxide layer in front of the notch tip (with a thickness of roughly 150 μm) was generated during heating and is clearly visible in Fig. 4.2 as the amorphous area surrounding the notch. While this oxide layer is expected to have an effect on fatigue crack *initiation* from the notch tip, it is not expected to affect crack growth far ahead of the notch, which is of interest in this study.

Before fatigue loading, a series of images covering the expected crack path was captured in a microscope at 10x magnification (Fig. 4.2). Since the microscope provides better lighting and resolution than *in situ* imaging, the microscope images were useful for determining grain boundary locations with more confidence. The crack path was drawn onto this series of microscope images a posteriori to allow for a comparison of crack path and microstructure (Fig 4.2).

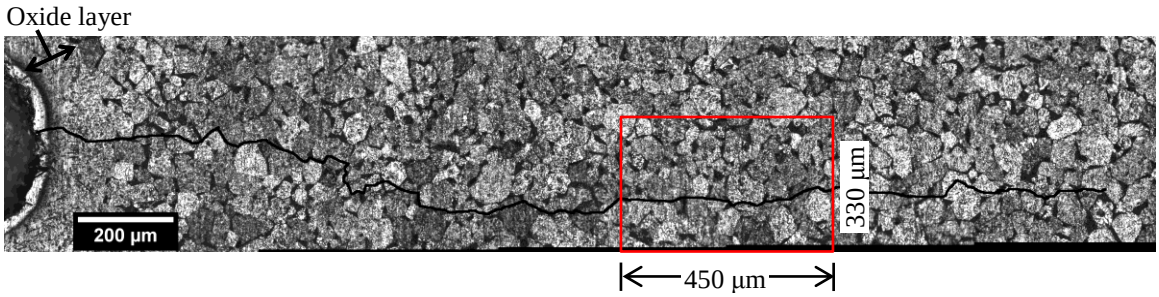

Fig. 4.2. Large grain titanium microstructure revealed by etching. The notch tip is shown on the left and the final crack line is drawn on the image in black. The region imaged at 14x is outlined by a red box.

The specimen was fatigue loaded sinusoidally at a frequency of 1 Hz and a constant load amplitude of 1.33 kN with an *R* ratio of 0.5 (*i.e.*, minimum load was half of the peak load). Crack initiation took roughly 10,000 cycles, which was followed by 80,000 cycles of fatigue crack growth to specimen failure. Throughout fatigue loading, images of the crack tip region were captured at 14x magnification (0.349 μm/pix) using a Navitar 12x lens with a 2x adapter tube and Sony xcd900 camera (1280 x 960 pixels). Without pausing or slowing down the fatigue loading, real time measurement cycles identical to the regular fatigue cycles were observed at 100 cycle intervals. During each of these cycles, images were captured at 7.5 frames per second to yield 8 images per measurement cycle (Fig 4.3). As mentioned in chapter 2, these images can be correlated within a single cycle (Fig. 4.3a) to measure quantities such as crack closure levels, or between cycles (Fig. 4.3b) to measure fatigue strain accumulation. Results from both methods will be shown here.

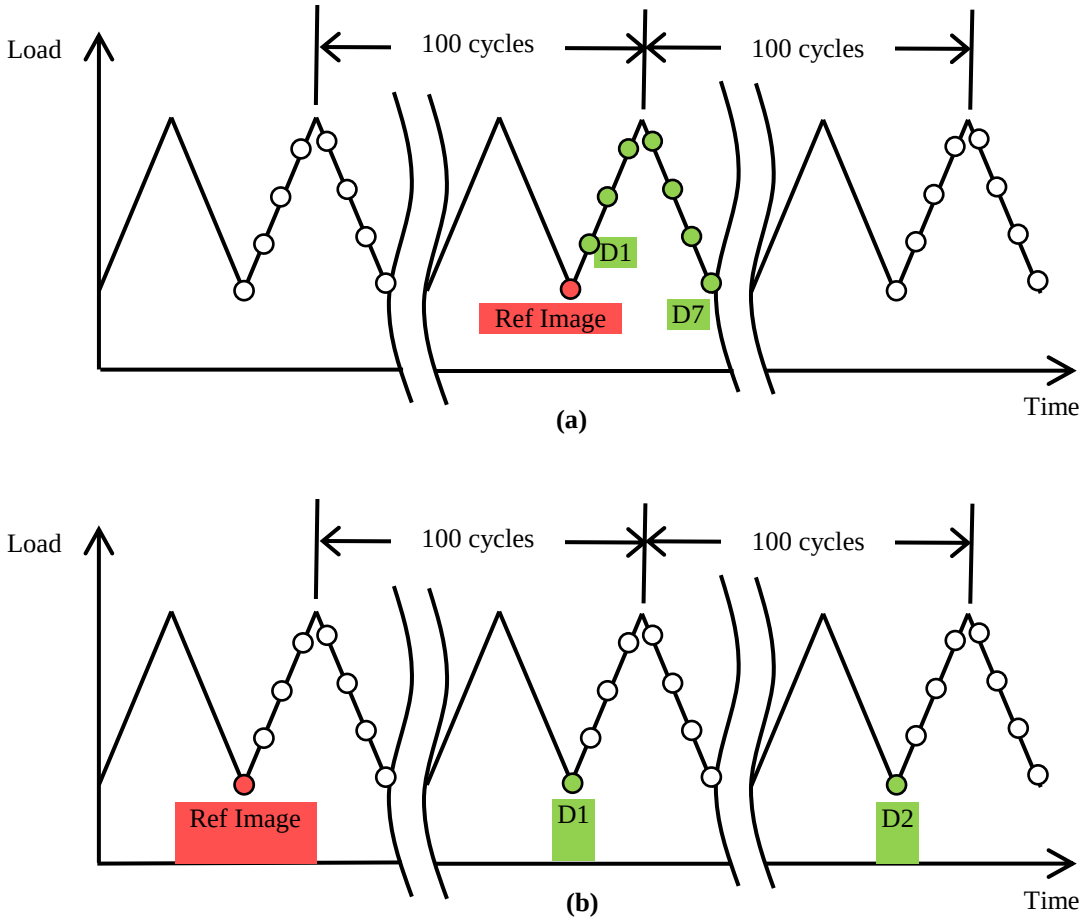

Fig. 4.3. In the large grain titanium experiment, eight 14x magnification images of the crack tip were taken every 100 cycles. DIC can be performed (a) within a cycle to measure quantities such as crack closure levels or (b) between cycles to measure fatigue strain accumulation.

Because the size of the 14x imaging region (450 μm by 330 μm as shown by the red box in Figure 4.2) is too small to capture the entire crack, the camera was moved periodically to keep the crack tip in the field of view. Several regions were imaged in this way, each for periods of thousands of cycles. Consequently, DIC correlations can only be performed on cycles within the same imaging region, *i.e.*, DIC results from the first cycle to a specific cycle number is not available. Results from the particular region shown in Figure 4.2 will be discussed here. This region was imaged for 1000 cycles as the crack grew at an average rate of 290 nm/cycle through the region.

Full-field DIC measurements can also be made from the images within a cycle. The ε_{yy} strain field for cycle 300 is shown in Fig. 4.4a on top of the reference image (minimum load image from cycle 300). The contour plot is made semitransparent in Fig. 4.4b to show the relation between the underlying reference image and strains. Because the specimen was etched to show microstructure, this strain field can be related to microstructural geometry. Two contours of high strain are outlined in Figs. 4.4 (a,b) for comparison with microstructure. The crack tip is indicated by a white dot. A clearer relation with microstructure can be found by plotting these contour outlines on the microscope image in which grain boundaries are more visible (Fig. 4.4c). This overlay shows that strain contours appear to be largely independent of microstructure although in some cases, such as the right edge of the top outlined contour (indicated by the arrow in Fig. 4.4c), strain transmission appears to be blocked at grain boundaries. However, keep in mind that the spatial resolution of DIC strain measurements is determined primarily by the subset size. Consequently, for sub-grain level DIC strain measurements, the subset size must be significantly smaller than the grain size. The subset size used in this correlation is 71 x 71 pixels, corresponding to a physical size of 25 μm. As Figs. 4.1 and 4.4c demonstrate, the average grain diameter of large grain titanium is roughly 50 μm. Therefore, although some promising information is obtained in this case regarding the influence of microstructure on fatigue damage accumulation, the resolution in this experiment is fairly coarse for sub-grain level measurements. In subsequent parts of this thesis, (Chapters 5 and 6) experiments with considerably improved resolution, based on microscopy imaging, will be discussed. Unfortunately, the natural tradeoff of increased spatial resolution is decreased field-of-view. So the results shown here are still of interest to determine fatigue damage accumulation at the mesoscale.

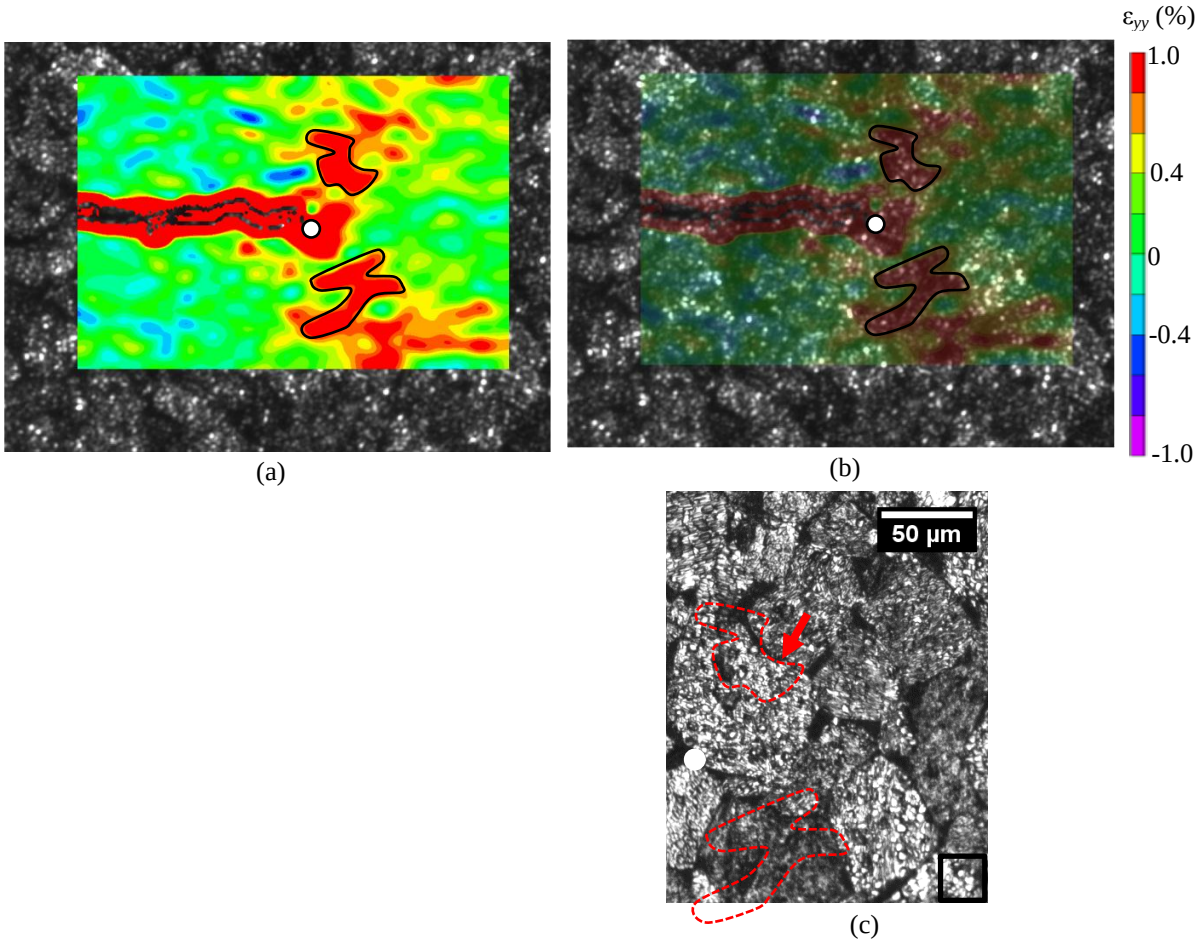

Fig. 4.4. (a) Peak load strain field, ε_{yy}, in cycle 300. (b) Semitransparent image showing relation between strain contour plot and grains in reference image. (c) Microscope image with selected strain contour outlines. Some strain localizations end at grain boundaries. The subset size is illustrated as a square. The crack tip location is indicated by a white dot in each figure.

Fatigue strain accumulation can be measured by correlating images *at the same load level* of subsequent cycles using the first cycle in the imaging region as the reference image, as shown by the colored dots in Fig. 4.3b (in this case, both the reference and deformed images are taken at minimum load). Two examples of full-field fatigue strain accumulation perpendicular to the crack are shown in Fig. 4.5(a,b) for cycles 200 and 900 respectively at the unloaded state, when correlated to the unloaded state at 0 cycles (set arbitrarily at the cycle at which imaging first started). These contour plots are at the same scale as the reference image shown in Fig. 4.5c, and the crack tip at the deformed image cycle is indicated by a white dot in Fig. 4.5(a,b,c). Here we

see that some fatigue damage accumulation, in the form of plastic strain, has been accumulated even in as little as 200 cycles. If no plastic strain were present, the correlation shown in Fig 4.5a would be the null field. However, the levels measured are well above the resolution limit for DIC (~0.05% strain) and appear to be generally concentrated, although in a highly inhomogeneous manner, into two lobes at angles near ±60° to the crack line. These lobe shapes are reminiscent of a macroscale plastic zone for a ductile material (Dodds, 1991). The significant inhomogeneities present however, indicate that although the aggregate response of the grains near the crack tip is approaching a homogenized plastic field, the local response is still influenced by microstructural inhomogeneities. This will be probed further in subsequent chapters where higher resolution experiments will be performed. Behind the crack tip in Fig. 4.5a, a plastic wake is seen forming from the current crack tip to the location of the tip at the image in cycle 0. Clearly, although the plastic wake exists to the left of this location, it cannot be captured by these DIC measurements since the crack tip had already grown that far through the imaging region before the reference image. Only strain accumulation from that time forward is captured. However, as the crack propagates, the plastic wake extends along with it, as can be seen by comparing figures 4.5a and 4.5b. When the crack exits the field of view at cycle 900, as seen in figure 4.5b, the residual plastic strain is clearly engulfing the crack line.

Two contours of high strain regions are outlined for cycle 900 (Fig. 4.5b). These regions are overlaid onto the reference image and a microscope image for comparison with microstructure (Figs. 4.5(c,d)). Some regions of these contours seem to indicate that strain does not transmit across some grain boundaries, but no strong assertions can be made because of the limited number of high strain regions. Another area for improvement is the etching process. Etching does not always give sharp indications of grain boundaries and can sometimes lead to a

less-than-ideal speckle pattern. These issues will be addressed by the *ex situ* procedure presented in chapter 5.

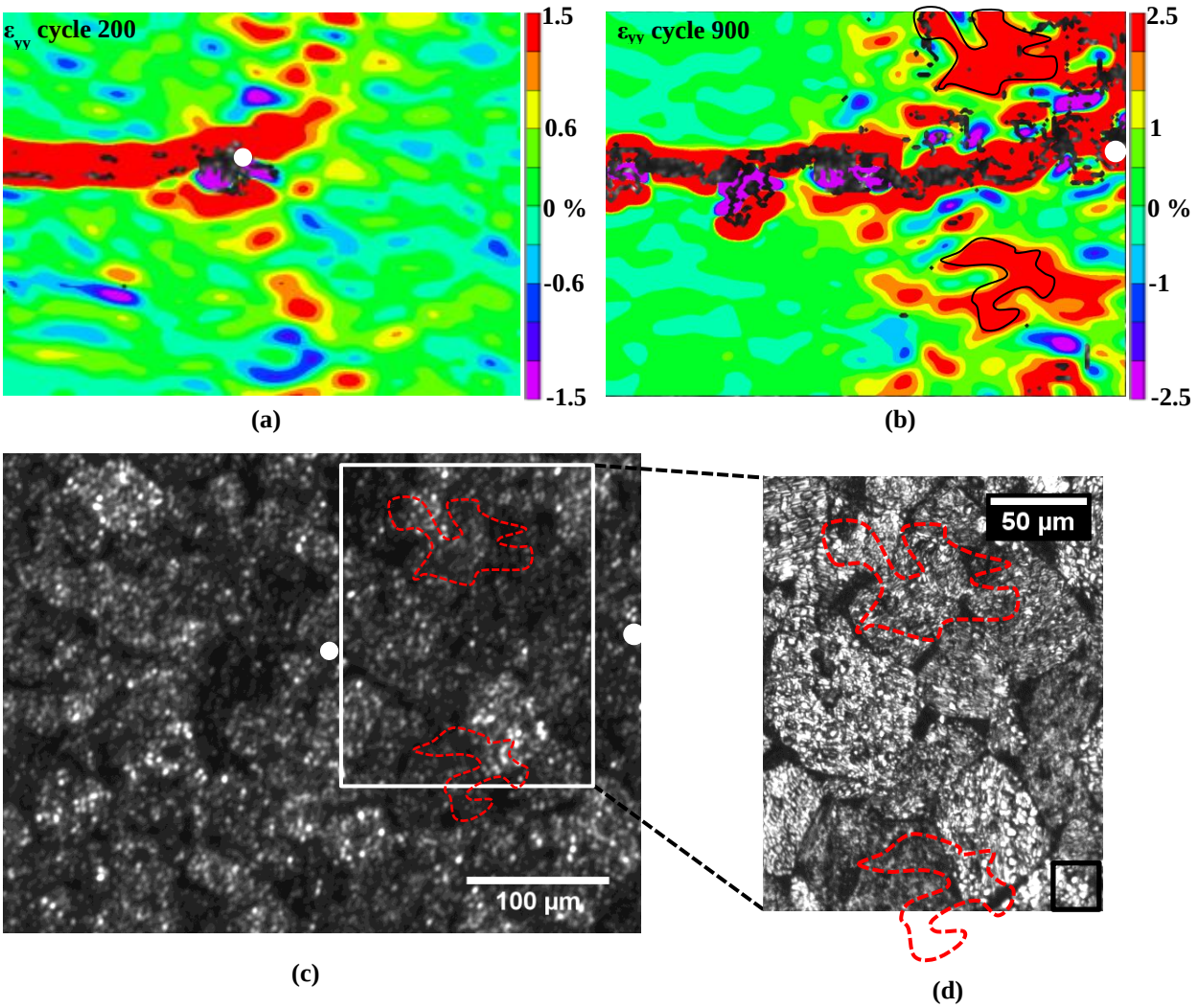

Fig. 4.5. Strain accumulation, ε_{yy} (perpendicular to the crack line), as the crack grows across the 14x region of interest. (a) Cycle 200, (b) cycle 900 with a contour outlined for comparison to microstructure. (c) Reference image with contour outline. (d) Microscope image with contour outline. Crack tip locations are indicated by a white dot in each figure.

4.2 Multiscale Fatigue Crack Growth in Hastelloy X

Fatigue crack growth in an SENT specimen made of Hastelloy X was studied at multiple scales to compare microscale and macroscale fatigue damage accumulation *simultaneously*. Hastelloy X is a nickel-based superalloy. Although the average grain size of this material is cited as 95 µm, the effective grain size is around 50 µm due to the presence of annealing twins that

divide nearly every grain. The composition of Hastelloy X is given in Table 4.1. Specimen dimensions were 50 mm x 6.96 mm x 1.47 mm with a 0.99 mm edge notch. Using a Navitar 12x lens, a 2x adapter tube, and an IMI Tech 202ft camera (1600 x 1200 pixels), a microscale region of interest was imaged at 14x magnification (0.322 μm/pix) on the front side of the specimen. On the back side of the specimen, the same lenses were used with an IMI Tech 1200ft camera (1600 x 1200 pixels) to image a macroscale region of interest at 2x magnification (2.12 μm/pix). Two labeled pictures of this two camera experimental setup is given in Fig. 4.6. Lighting on the back surface of the specimen (2x) was provided by a fiber optic ring light. At high magnifications, it is difficult to obtain adequate lighting; consequently, fiber optic gooseneck lights were used in addition to a fiber optic ring light on the front surface of the specimen (14x). Even both of these lights at full power were minimally sufficient for acquiring adequate DIC images in real time.

Table 4.1. Chemical Composition of Hastelloy X.

Element	Weight %
Nickel	47 (balance)
Chromium	22
Iron	18
Molybdenum	9
Cobalt	1.5
Manganese	< 1
Silicon	< 1
Carbon	< 0.1
Boron	< 0.008

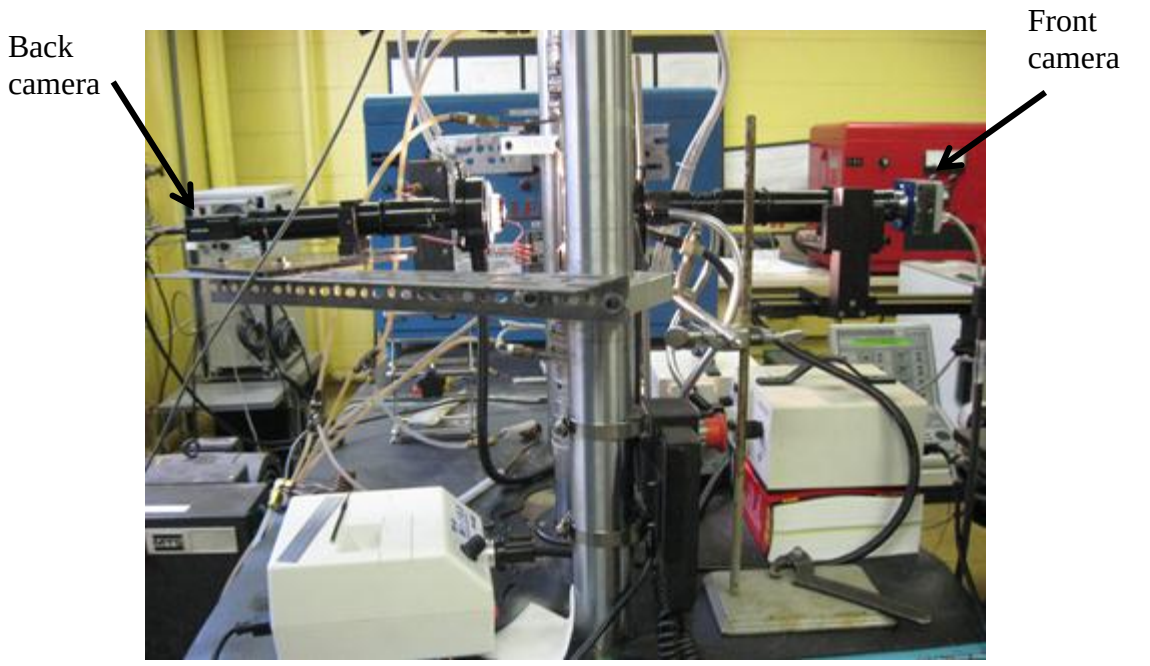

(a)

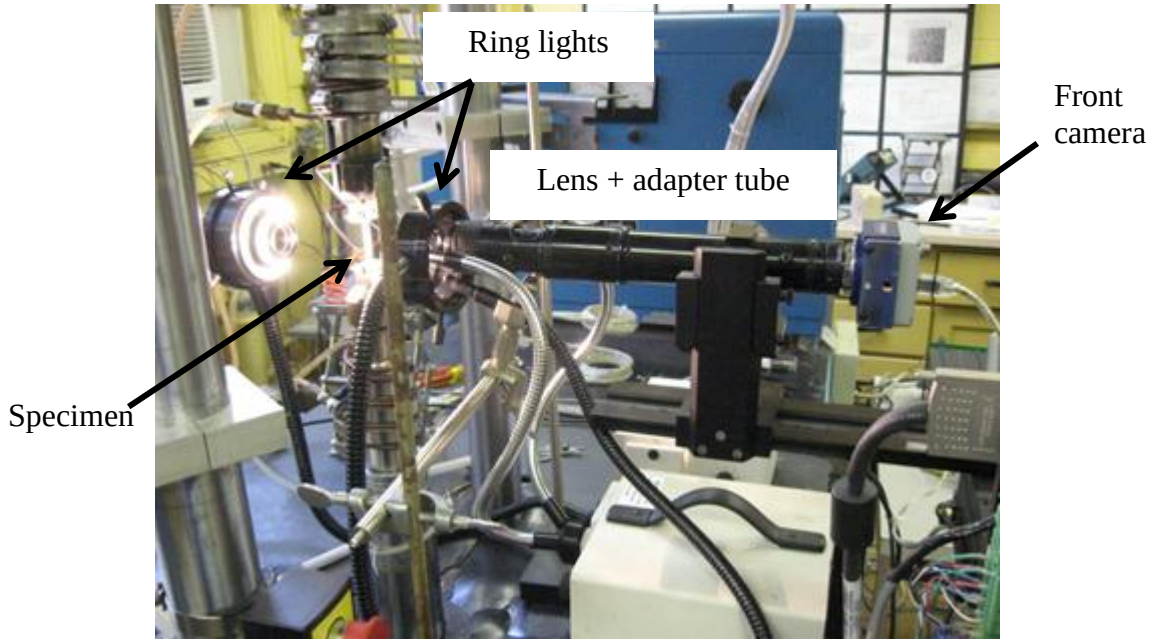

(b)

Fig. 4.6. Two views of the experimental setup for the multiscale crack growth experiment.

The speckle pattern on the front of the specimen (imaged at 14x magnification) was created by finely polishing the specimen using 0.3 μm silicon carbide powder and then depositing 1 μm silicon particles onto the specimen surface with compressed air as described in

Jonnalagadda *et al.*, 2010a. On the back side of the specimen (imaged at 2x), a roughly polished surface (achieved with 800 grit polishing paper) was sufficient to provide a speckle pattern.

The specimen was fatigue loaded with a sinusoidal load at constant ΔK of 19.5 ± 1.5 MPa$\sqrt{m}$ and $R \approx 0.1$. The fatigue crack was grown at a loading rate of 2 Hz before entering the microscale region of interest. While the crack traveled through this region, a loading frequency of 1 Hz was used to allow more images to be captured per cycle. Real time measurement cycles were observed every 512 cycles without slowing or stopping the fatigue loading. During each measurement cycle, two images were captured at 2x magnification, one at minimum load and one near peak load. Simultaneously, 16 images were captured at 14x throughout the cycle at a frame rate of 15 frames per second. Image capture times are illustrated as the white or red dots in Fig. 4.7.

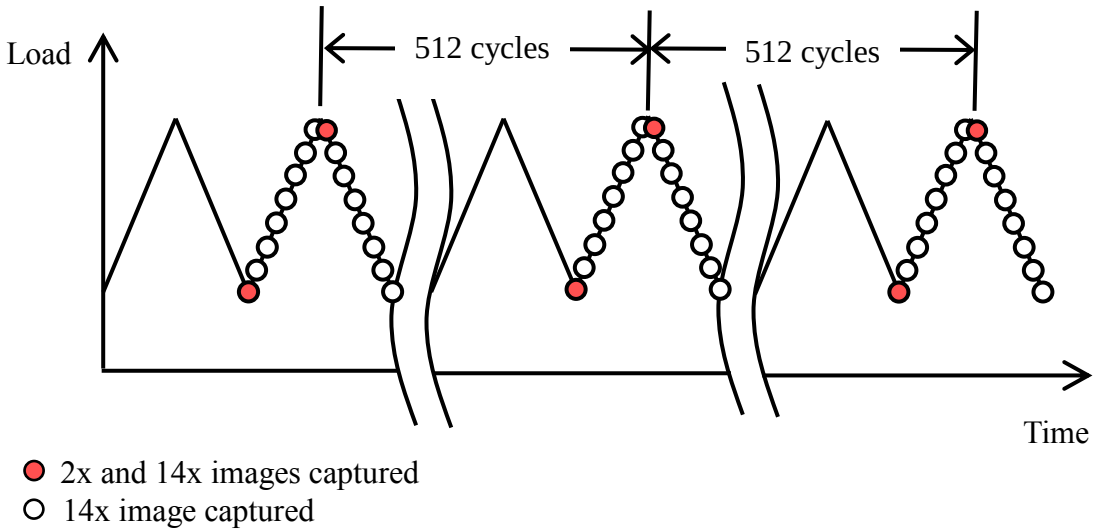

Fig. 4.7. Images of the specimen were taken during measurement cycles at intervals of 512 cycles as shown. At 14x magnification, 16 images were taken per cycle while two images were taken at 2x magnification.

Typical images at both magnifications near peak load are shown in Fig. 4.8. Because the 2x images were captured on the back side of the specimen, the image in Fig. 4.8a (and the 2x DIC results in this chapter) has been flipped horizontally to allow for comparison to measurements at 14x magnification on the front of the specimen. The box drawn on the 2x image

in Fig 4.8a corresponds to the location of the 14x region of interest. Fig. 4.8b shows the 14x region of interest (but on the opposite face of the specimen). Vickers indentation marks outlining the region are faintly visible in the four corners of this image. These marks will be used to align DIC measurements of the 14x region with optical micrographs and associated *ex situ* DIC results discussed later. The crack path is visible at both magnifications in Fig. 4.8. At 2x, the crack path appears black, while it appears white at 14x.

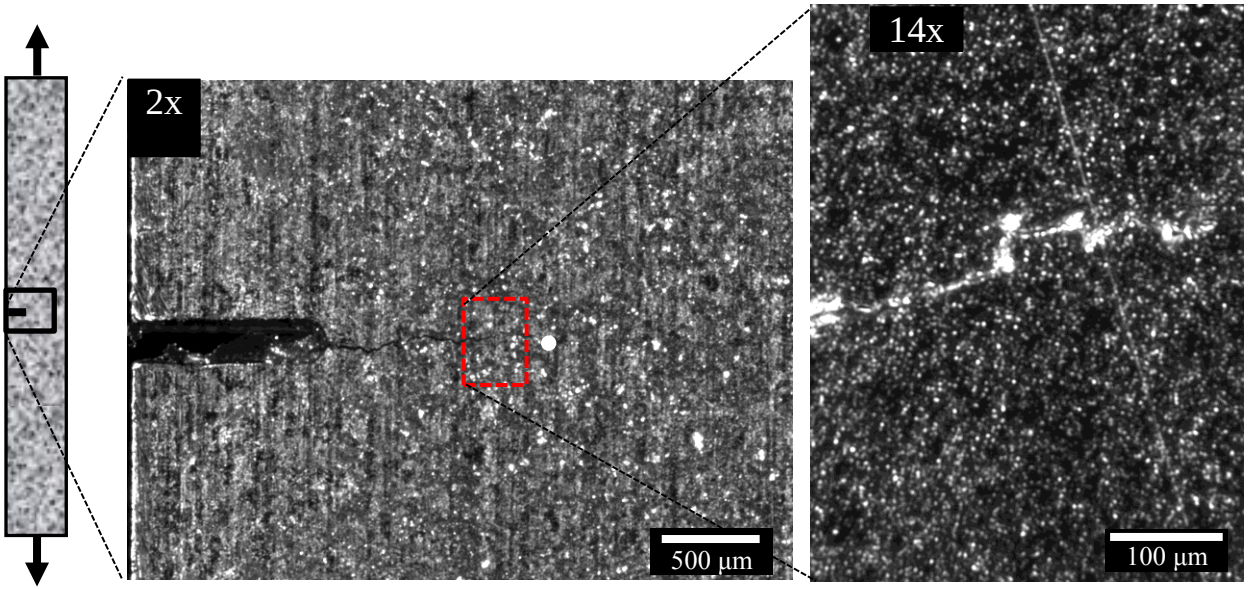

(a) **(b)**

Fig. 4.8. Images obtained from (a) 2x and (b) 14x cameras after the crack had grown through the region of interest. Because 2x images were captured on the back side of the specimen, the image in (a) has been flipped horizontally to correspond to the view seen on the front of the specimen (b).

To study fatigue strain accumulation at multiple scales, DIC was performed at both 2x and 14x magnifications using reference and deformed images captured at the same load level (minimum load). Consequently, all the strain fields measured from these correlations are fatigue strain accumulation (essentially plastic strain) associated with fatigue crack growth. Contour plots of fatigue strain accumulation perpendicular to the crack line are shown at both magnifications in Fig. 4.9. For these plots, the reference images were those taken at the minimum load during the first fatigue cycle and the deformed images were captured after the

crack had grown through the 14x region of interest to a total crack length (notch plus fatigue crack) of 2.1 mm. The crack tip is indicated by a black dot in Fig. 4.9a. The wake of plastic deformation left behind by the propagating fatigue crack is evident in the 2x strain contour plot. This wake covers a large region several millimeters wide from the notch tip to beyond the crack tip. There are two lobes of high strain ahead of the crack tip, but the material directly ahead of the crack tip is relatively unstrained.

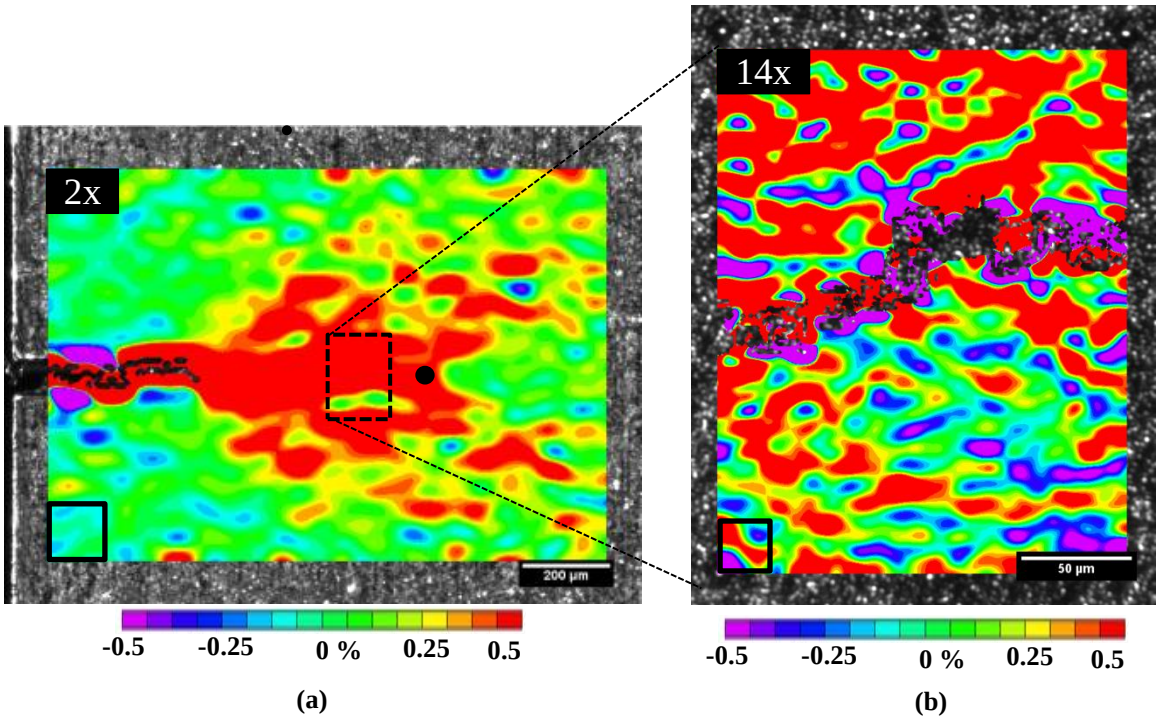

Fig. 4.9. Fatigue crack growth strain field perpendicular to crack line, ε_{yy}. (a) 2x magnification (b) 14x magnification showing greater inhomogeneity of the strain field.

In Fig. 4.9b, the 14x magnification results show a region of the strain field with higher spatial resolution. Because of lighting changes associated with crack propagation, the crack line has many failed correlation points; nevertheless, there is a great deal to be learned from the strain field adjacent to the crack line. At 14x magnification, this strain field is seen to be less homogeneous than would be implied by the 2x magnification DIC results. This is due to the fact that the subset size, and hence the DIC spatial resolution, is smaller at 14x. In this experiment,

the 2x subset size (61 x 61 pixels) is 129 μm whereas the 14x subset size (71 x 71 pixels) is significantly smaller at 23 μm. The 2x subset size is so large it covers over half of the entire imaging region at 14x. Subset sizes are shown as black squares at each magnification in Fig. 4.9.

Although the 14x results have more noise, the smaller physical subset size allows for observation of strain localizations that could not be made at 2x magnification. The material below the crack tip at 14x has less strain than the top, possibly a result of the upwards kink of the crack at that point, but it is not completely unloaded as might be inferred from 2x results. Instead, it has a few areas of localization with gaps of relatively unloaded material.

After the crack had grown beyond the end of the 2x imaging region, the specimen was removed from the load frame, the speckle pattern was washed off, and the specimen imaged in the optical microscope and the scanning electron microscope (SEM). As compared to the *in situ* images, microscope images show the crack more clearly (Fig. 4.10). The crack path in the macroscale region of interest is imaged by the optical microscope at 5x magnification in Fig. 4.10a. The microscale region of interest, outlined by indentation marks, is indicated by a red box in Fig. 4.10a. The SEM image, at roughly 14x magnification in Fig. 4.10b covers this microscale region.

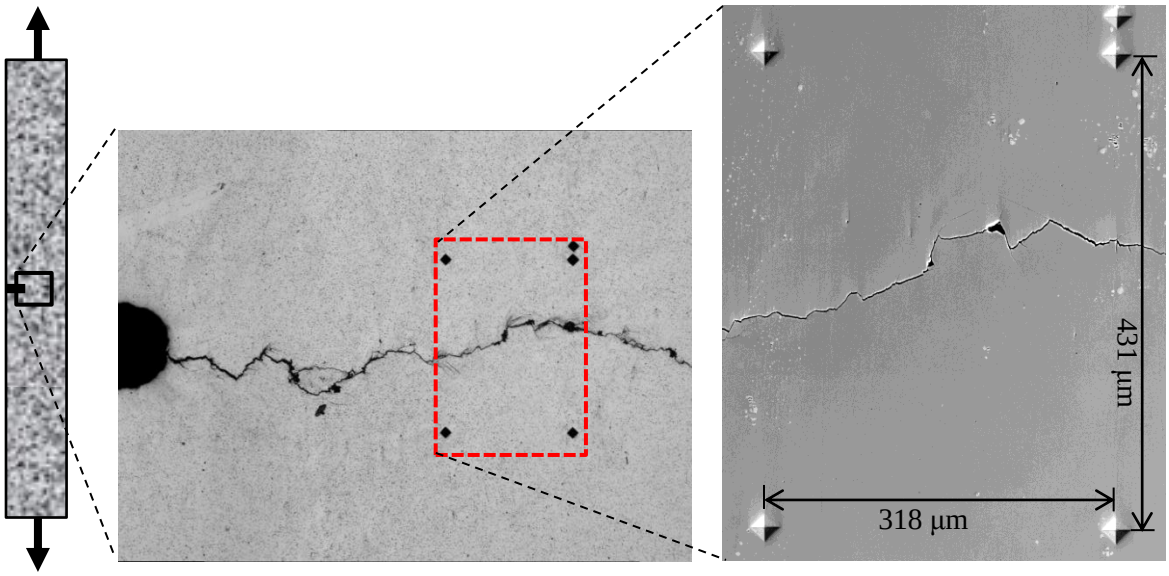

Fig. 4.10. (a) Microscope region showing the 14x region of interest outlined by indentation marks. (b) This region was imaged in the scanning electron microscope to obtain a clearer picture of the crack line.

Ex situ microscope images of the specimen after the crack has grown through the region of interest can be used to identify the crack path more clearly. However, these images have another valuable use in terms of DIC, as illustrated by Efstathiou *et al.* (2010). In addition to capturing images of the specimen after the crack had propagated, the specimen was also imaged in the optical microscope before the start of fatigue loading. Two adjacent microscope images were captured at 5x magnification both before and after fatigue loading to roughly cover the macroscale region of interest. At 20x magnification, three adjacent optical microscope images cover the microscale region. By correlating each pair of images and stitching the DIC results together, an *ex situ* measurement of fatigue strain accumulation over a number of cycles can be obtained from microscope images. The resulting *ex situ* DIC strain fields perpendicular to the crack line are shown for both 5x and 20x magnifications in Fig. 4.11. The strain fields in Fig. 4.11 are in agreement with *in situ* strain fields shown in Fig. 4.9 although they measure fatigue strain accumulation over slightly different time periods (*i.e.*, the *ex situ* images include more

crack growth beyond the imaging region than the *in situ* measurements). Note that the *ex situ* DIC strain fields are more detailed and have less noise than the *in situ* strain fields in Fig. 4.9.

Clearly the *ex situ* methodology can provide higher resolution images of residual plastic strain. However, even the 20x magnification results shown here, sub-grain level resolution is not substantially achieved. This *ex situ* procedure will therefore be developed further in the next chapter to achieve sub-grain residual strain measurements.

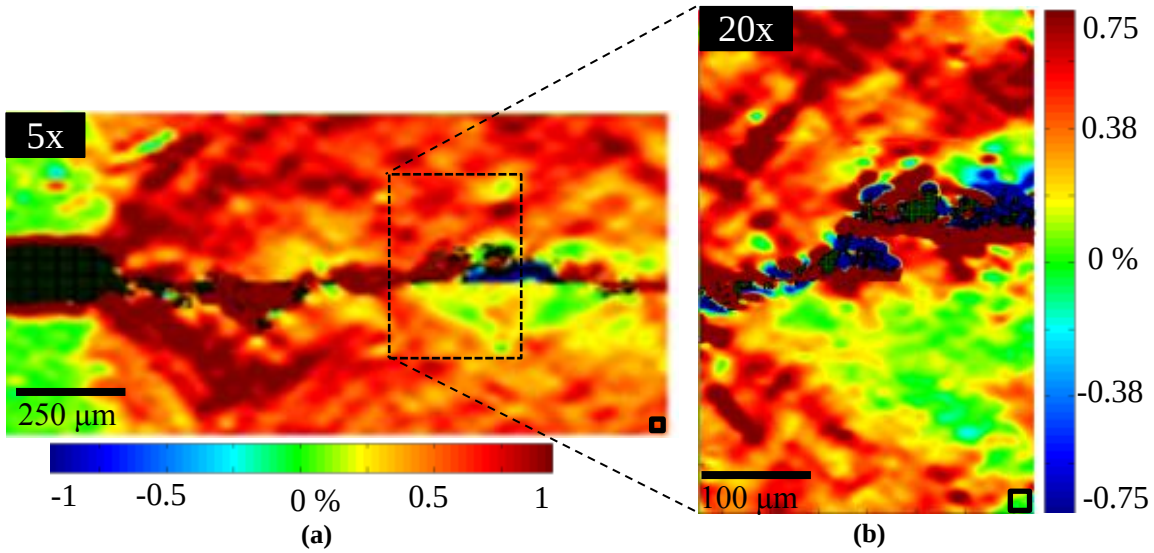

Fig 4.11. *Ex situ* DIC strain fields perpendicular to the crack line from the optical microscope. (a) Results of three correlations at 5x magnification stitched together to roughly cover the macroscale region of interest. (b) Results of three 20x correlations that cover the microscale region of interest.

4.3 Summary

This chapter showed residual plastic strain fields measured at multiple scales associated with material damage accumulated during fatigue crack growth at in large grain titanium (average grain size of 50 μm) and Hastelloy X (average grain size of 95 μm, but effective grain size around 50 μm). By performing DIC on an etched specimen with visible grain boundaries, the experiment on large grain titanium demonstrated one technique for linking fatigue strain accumulation to microstructure. Subset sizes were found adequate for some grain level resolution and some linkage between strain and microstructure was found. While some insight was gained

from this experiment, it is clear that further experiments with better imaging resolution and measurements of microstructural orientation (in addition to the grain geometry information here) could provide a great deal more insight.

The multiscale fatigue crack growth experiment on Hastelloy X demonstrated the relationship between macroscale and microscale DIC measurements. At the macroscale, a wake of plastically deformed material several millimeters wide is left behind the propagating crack. This wake appears to be relatively homogeneous when viewed at low magnifications, but higher magnification studies (at 14x magnification) showed large amounts of strain localization. Higher magnifications, such as those shown in the following chapters, will provide better measurements of these strain inhomogeneities at the microstructural level.

Chapter 5: High Resolution *Ex Situ* DIC Measurement Technique[3]

This chapter outlines a novel methodology for linking high resolution DIC strain measurements to microstructural characteristics. Since spatial and measurement resolution are related in DIC, high resolution DIC measurements (compared to those discussed in the previous chapters) are necessary to achieve sub-grain level resolution. This chapter begins with some background and motivation for the technique in section 5.1. The procedure for using this novel *ex* situ DIC technique is described in section 5.2. The technique is then used to investigate strain localizations surrounding a growing fatigue crack. Section 5.3 explains the specifics of the experimental procedure, and the resulting DIC strain fields are discussed in section 5.4. Section 5.5 and 5.6 focus on incremental strain fields and the relation between strains and microstructure, respectively. Finally, section 5.7 provides a summary of this work.

5.1 Background and Motivation

The two most common experimental methods that have been used for quantitative, full-field, grain level measurements are grid techniques (Delaire *et al.* 2000; Clayton *et al.*, 2002; Héripré *et al.*, 2007) and digital image correlation (DIC) (Tong, 1997; Raabe *et al.*, 2001; Zhao *et al.*, 2008; Bartali *et al.*, 2009; Tschopp *et al.*, 2009; Merzouki *et al.*, 2010; Walley *et al.*, 2010; Efstathiou *et al.*, 2010; Padilla *et al.*, 2011). Grid techniques have proven to work well for large

[3] The first half of this chapter closely follows Carroll *et al.*, 2010 in which this technique was first introduced.

amounts of global strain (on the order of unity), but DIC provides more accuracy at lower strain levels, such as those more commonly found in engineering structures subject to fatigue failure.

In addition to the accuracy of strain measurements, the spatial resolution of experimental measurements is important. Obtaining reliable strain measurements that can be compared to microstructure requires a measurement technique with *sub-grain* level spatial resolution. For the DIC technique, this effectively means that the subset size must be several times smaller than the grain size, thereby allowing many measurement points within each grain. Since subset sizes are typically limited to the range of 31–101 pixels squared, grain size and magnification are the two main parameters that can be varied to attain a large ratio of grain size to subset size. Many researchers have achieved the necessary spatial resolution by using materials with large grain sizes on the millimetric (Sutton *et al.*, 1983; Raabe *et al.*, 2001; Sachtleber *et al.*, 2002; Zhang, 2004; Zhao *et al.*, 2008) or even centimetric (Delaire *et al.*, 2000) scale. Such large grain sizes allow DIC images to be taken at relatively low magnifications while still achieving "sub-grain" resolution. There are many benefits of low magnification DIC when compared to experiments at higher magnification, such as larger optical depth of field, easier speckle pattern creation, and easier alignment of strain fields with microstructure. However, since most structural materials have considerably smaller grain sizes (on the order of 100 μm or smaller), it is not clear whether all conclusions obtained from experiments on large grain size materials are valid for smaller grain size cases.

The other approach to obtaining adequate spatial resolution is to perform experiments at high magnification. A few researchers have attempted to relate *in situ* strains at the grain level to microstructural measurements. Padilla *et al.*, 2011 used *in situ* DIC to measure deformation behavior in dynamically loaded Zr specimens. Strain fields were spatially overlaid with

microstructural information and the effects of microstructure on deformation behavior were investigated on a statistical basis. However, the relatively low magnification used in the experiments (1.2 μm/pix) limited the spatial measurement resolution to approximately the size of the grain diameter (48 μm). This resolution, while adequate for the statistical analysis performed over large numbers of grains in Padilla *et al.* (2011), is not sufficient for a pointwise comparison of full-field deformation behavior to microstructure. Bartali *et al.*, 2009, made higher magnification *in situ* observations of fatigue at the grain level, but were limited by the lack of a good speckle pattern and optical changes to the specimen throughout the test.

Due to difficulties of *in situ* imaging in conventional load frames, including vibrations, optical limitations, and speckle pattern quality, some researchers have built miniature load frames to be used in an optical microscope (Tong, 1997; Zhang, 2004; Zhao *et al.*, 2008). These experiments circumvent the challenges existing in conventional load frames, but they are limited in terms of specimen size and loading capabilities (*i.e.*, it is difficult to perform fatigue or high temperature experiments).

Yet another approach to high magnification experimentation is to perform image correlation with scanning electron microscope (SEM) images (Tschopp *et al.*, 2009; Tatschl and Kolednik, 2003; Zhu, 2011). As with optical microscopy, *in situ* SEM experiments are limited in specimen size and loading type, but the SEM is capable of much higher magnification. Furthermore, since microstructural information is readily obtained in the SEM through electron backscatter diffraction (EBSD), alignment of strain fields with microstructure maps is relatively simple and accurate. However, the use of an SEM for strain measurements using DIC (or grid techniques) does have disadvantages. First, since the image capture process takes several seconds, specimen drift during image capture can generate artifacts in measured strain fields.

Additionally, image correlation techniques can be affected by SEM image noise such as background noise, carbon contamination buildup that causes darkening in imaged regions, and the visibility of grain boundaries, which degrades speckle pattern quality.

One fundamental limitation of *in situ* techniques is their single field of view, or a small number of views with separate cameras (*e.g.*, Abanto-Bueno and Lambros, 2005). With adequate spatial resolution for sub-grain level DIC measurements, this means *in situ* techniques are effectively limited to observations of a small number of grains. *Ex situ* DIC, in which the specimen is imaged before and after an applied loading, allows multiple imaging regions to be studied at the desired magnification. These regions can be stitched together to provide high resolution DIC data over a larger number of grains. Efstathiou *et al*., 2010 demonstrated that this *ex situ* technique can be used to determine the size of a representative volume element for plastic strain accumulation in Ti. The primary drawback of *ex situ* techniques is that they require interruption of the experiment and removing the specimen from the load frame for each measurement. Consequently, these techniques are only capable of measuring accumulated strain. Despite their shortcomings, *ex situ* measurements have high spatial resolution, which is particularly useful in certain cases, such as measuring fatigue damage accumulation.

To relate to measured strain fields, microstructural information must also be obtained on a full-field basis and aligned with the strain fields. Alignment can be accomplished with features that are visible in both microstructure maps and correlation images. For low magnification experiments, specimen edges are commonly used. At higher magnifications, the use of fiducial markers or grain boundaries is more typical. A straightforward approach to alignment is to etch specimens to visualize grain boundaries in the correlation images (Bartali *et al.*, 2009; Efstathiou *et al.*, 2010). This method provides excellent alignment of DIC fields with microstructure;

however, etched specimens usually have a less-than-ideal speckle pattern. Furthermore, etching only provides one aspect of microstructural information – grain geometry. Another important aspect of the microstructure is grain orientation, which is typically measured using EBSD. Despite its aforementioned disadvantages, using SEM images to measure strain fields is particularly attractive since it allows easy alignment of strain fields with EBSD grain orientation maps. Tschopp *et al.,* 2009 describe a technique for linking strains to microstructure in a scanning electron microscope with alignment provided by a combination of grain boundaries and fiducial markers.

In this chapter, a new technique is presented for measuring strain accumulation over a region covering hundreds of grains, but with sub-grain level resolution, and linking those strain fields to microstructural measurements. This method was developed with great consideration to the details and tradeoffs of the techniques discussed earlier. In this method, *ex situ* optical microscopy DIC is used to measure strain fields. Through the techniques of image and data stitching, high resolution fields are obtained over relatively large regions of the specimen. Fiducial markers are then used to align strain fields with microstructural information from EBSD. Clearly, this technique is only valid for surface measurements. Internal measurements combining DIC and EBSD are more cumbersome since they would require sample sectioning, but are also possible (Groeber *et al.*, 2008; Field *et al.*, 2010). The experimental technique described here was first was introduced and demonstrated in Carroll *et al.*, 2010.

5.2 High resolution *Ex Situ* Image Correlation Procedure

The *ex situ* DIC procedure consists of six important steps which are meant to ensure that high resolution DIC strain field maps can be precisely combined with comparable resolution microstructural information. These six steps, which will be discussed in detail in the next six

sub-sections, are to: (1) place fiducial markers on the sample for spatial alignment of the various datasets to be collected; (2) gather microstructural information through EBSD measurements; (3) apply a speckle pattern to the specimen and capture reference images in the optical microscope; (4) load the specimen (mechanically, thermally, *etc.*) such that permanent deformation is achieved, and capture images of the deformed specimen again in the optical microscope; (5) perform DIC and stitch the resulting fields; (6) align the DIC strain field from step (5) with the microstructure obtained with EBSD from step (2) using the fiducial marks placed in step (1).

5.2.1 Fiducial Markers

One of the major challenges in successfully implementing the *ex situ* DIC technique is to spatially align the data from both sources, mechanical and microstructural, and to do so with sub-grain level accuracy. Such alignment requires fiducial markers—features that appear in both sets of data—be placed on the sample under investigation. While any features can be used as markers, certain characteristics are required to guarantee accuracy and precision of the experimental results. Markers should be numerous so that location, scale, and rotation between the two sets of data can be determined. The markers must also be permanent so that they do not change their shape or position on the specimen between the times that each of the datasets is collected. In addition, the fiducial markers should have features small enough to ensure sub-grain level alignment. Finally, the markers must not affect measurements or material behavior for the particular loading used.

Vickers marks were chosen as fiducial markers, because they satisfy the four criteria discussed above and because they can be placed easily and precisely. To satisfy the first criterion, an asymmetric pattern of five marks (Fig. 5.1) was used to allow for placement, scale, and rotation alignment of the datasets generated from multiple devices. Second, Vickers marks

are permanent, unlike other marking methods that may be altered chemically or physically. Third, the sharp edges of Vickers marks and the ability to separate them by some distance allow for precise alignment. The fourth criterion is not strictly met since indentation marks leave residual stresses in the material in the vicinity of the indentation marks. However, this effect is made relatively insignificant by ensuring that the affected regions are a small portion of the region of interest and by avoiding results very close to marker locations. A typical use of Vickers indentation marks is shown in Fig. 5.1 where indentation marks are visible in optical images (Fig. 5.1a), secondary electron imaging (Fig. 5.1b) and in EBSD results (Fig. 5.1c). These marks are approximately 25 μm wide each and spread out so that the region bounded by them is 700 by 800 μm. The sharp corners of the marks will later allow for precise alignment of EBSD with DIC results (with alignment accuracy better than 5 μm).

5.2.2 EBSD Measurements

The second step of the *ex situ* procedure is to characterize the microstructure using EBSD (Randle and Engler, 2000). Because standard EBSD sample preparation techniques remove material from the specimen surface due to the subsequent grinding and polishing, Vickers indentation marks are made *after* sample preparation is completed and before placing the specimen into the SEM. Depending on the size of the area of interest, multiple EBSD scans may be needed to span the entire region. In this study, EBSD data were collected using a JEOL 7000F SEM with measurement points spaced by 1 μm. Fig. 5.1c shows a typical EBSD result consisting of 9 individual maps stitched together. The five fiducial Vickers marks are circled in the image of Fig. 5.1c.

After performing EBSD, and before capturing reference images, a speckle pattern is placed on the specimen. The powder speckle method described in chapter 4 has been found to work well at the high magnifications used in this *ex situ* method.

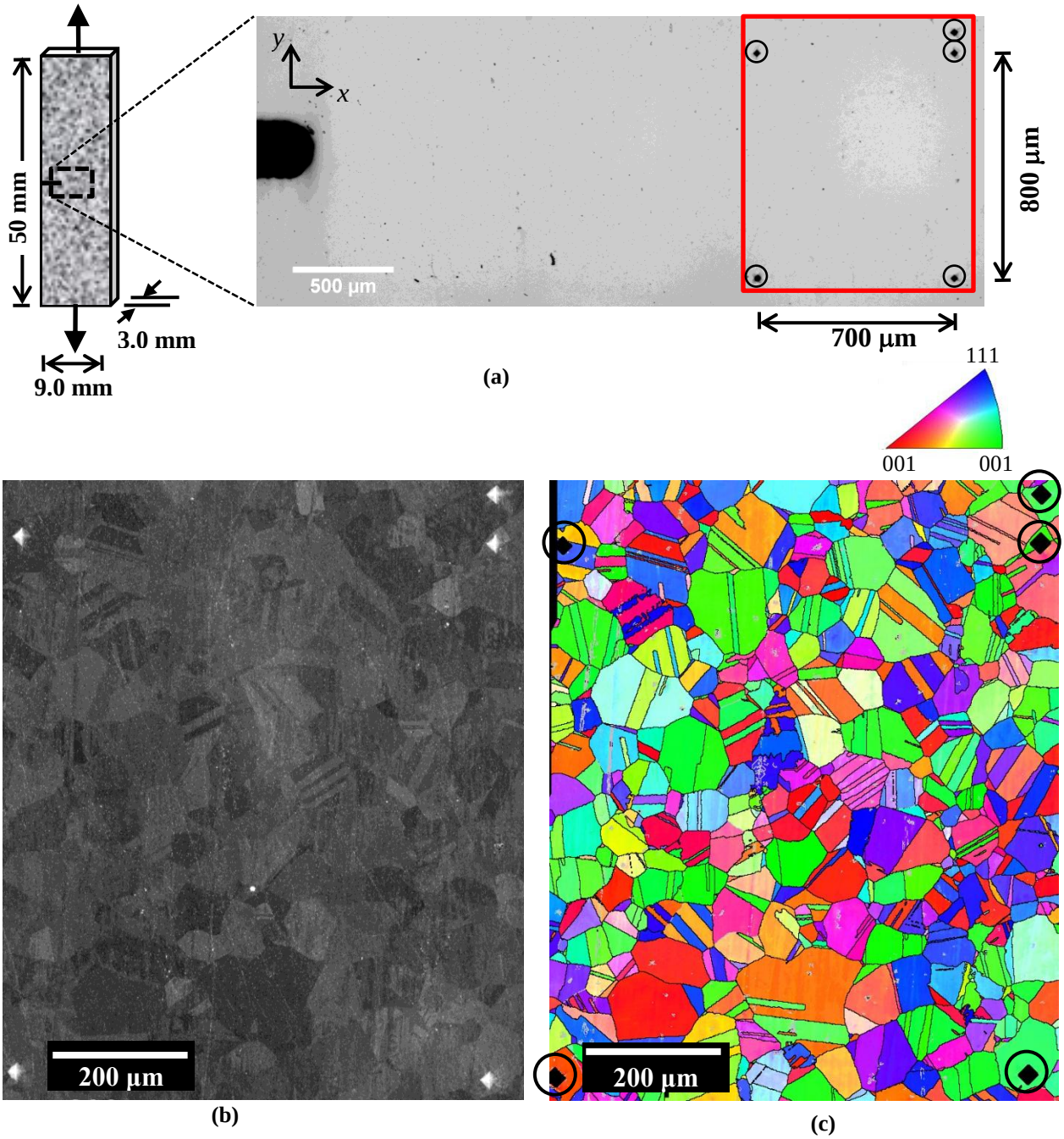

Fig. 5.1. (a) Specimen dimensions for the SENT specimen used here. The notch is 1.5 mm long. A micrograph of the unspeckled specimen shows the region of interest, outlined by a red box, with Vickers indentation marks at the corners (circled in black). (b) Secondary electron image of the region of interest showing grain boundaries and Vickers indentation marks. (c) EBSD results over the region of interest comprising of the combined results from nine EBSD scans.

5.2.3 Reference Images for DIC

In order to relate material deformation to microstructure, the reference images have to be acquired with a high enough magnification to guarantee deformation measurements with sub-grain level resolution. This DIC resolution requirement, which can be quantified by subset size, is dependent on the magnification level at which images are taken. Higher magnification leads to improved resolution, but smaller fields of view. Several magnifications are listed in Table 5.1 along with their corresponding field of view (compare to Fig. 5.2), image resolution, subset size, and ratio of grain area to subset area. These specifications are dependent on a camera's pixel size; hence, the magnification values in Table 5.1 are only valid for the camera used in this study

At 14x magnification, the highest magnification used so far in the load frame setup, the optical resolution is only 0.31 μm/pix resulting in subset sizes around 33 μm (see Table 5.1). At 50x magnification, the optical resolution is 0.087 μm/pixel, but a single image covers an area of only 140 x 104 μm (Table 5.1). To observe a larger region, an array of images is taken, with significant overlap among neighboring images, to cover the entire region of interest including the fiducial marks (Fig. 5.2). A subset size on the order of one-half the grain diameter or smaller (in the linear dimension) is required for resolving grain level strains in the material. This corresponds to a ratio of grain area to subset area of roughly four which implies that 20x magnification would be required for grain level DIC resolution when using a 101 pixel subset size (although smaller subset sizes are more typical). It is important to note that there is often significant overlap between subsets; consequently, the number of correlation points within a grain is significantly larger than the ratio of grain area to subset area. For example, at 50x magnification with a subset spacing of 10 pixels, there would be 2600 correlation points within a typical 50 μm grain.

Table 5.1: Measurement resolution properties at several magnifications for a camera with a pixel size of 4.4 µm.

Magnification	Field of View (µm)	Scale (µm/pix)	Subset Size at 101 pix (µm)	Ratio of Grain Area to Subset Area*
1x	7000 x 5200	4.4	440	0.01
5x	1400 x 1100	0.88	89	0.32
10x	700 x 500	0.44	45	1.2
14x	530 x 400	0.31	33	2.3
20x	350 x 250	0.22	23	4.7
50x	140 x 100	0.087	9	31

***For a grain size of 50 µm**

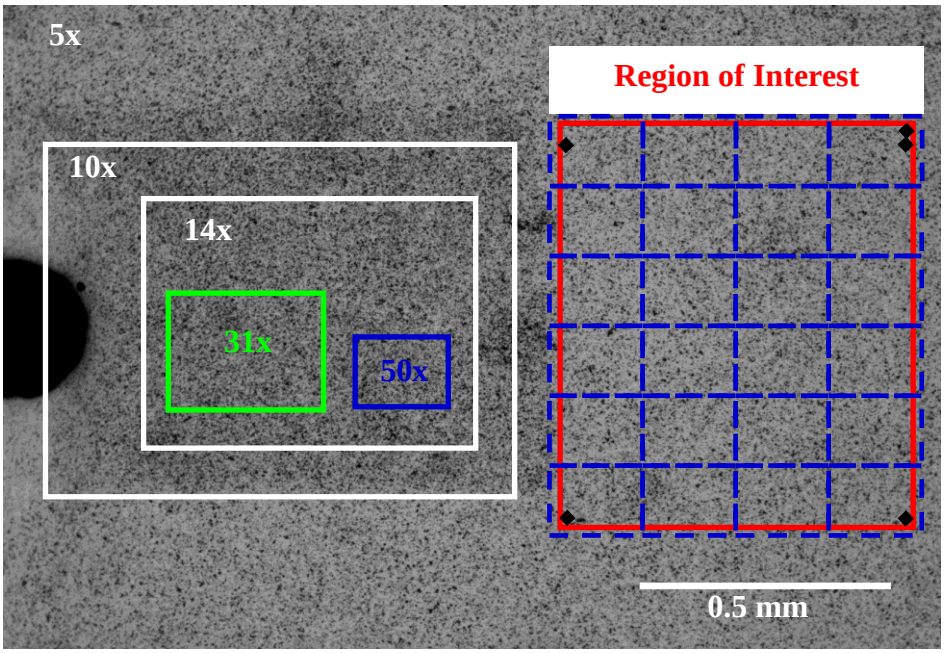

Fig. 5.2. Relative image sizes at several magnifications. The region of interest is imaged at high resolution using an array of high magnification images to cover the region outlined by the indentation marks.

It is emphasized that the required resolution depends on the grain size or other microstructural features present in the material. As those features get smaller in size, higher magnification images are required for sub-grain level resolution. Because the depth of field at high magnifications is limited, and because the distance from the lens to the specimen changes slightly with position, it may be necessary to refocus before capturing each image in the image set. This must be done for both reference and deformed images and is a major obstacle to automation of this process.

5.2.4 Deformation

After applying the desired loading to the specimen, *e.g.*, growing a fatigue crack for a number of cycles, the specimen is removed from the load frame, placed in the optical microscope once again, and images of the deformed state are captured at the same locations and magnification as the reference images. The location of each one of those images is determined by visually aligning the observed region with its corresponding reference image. This process of loading and capturing deformed images can be repeated several times, as necessary, to investigate strain evolution with increased loading.

5.2.5 Stitching DIC Results

With reference and deformed image arrays acquired, there are two options available to obtain the strain fields throughout the region of interest: (1) The image arrays can be stitched together to form very large images on which DIC can be performed; or (2) Each pair of reference and deformed images can be correlated individually, and the DIC strain fields resulting from all of the correlations can then be stitched together. For a discussion and comparison of the two stitching techniques, see Carroll *et al.* (2010). The second stitching technique is more time consuming because it requires the user to perform hundreds of DIC correlations instead of just one, but as detailed in Carroll *et al.*, it provides results that are more trustworthy than the image stitching method. Furthermore, the image stitching method generates significant artifacts when accumulated strains are small (less than 1% global strain). For this reason, only the second stitching technique, used in this and the next chapter, will be discussed here.

Each pair of reference and deformed images (individual images, not stitched) was correlated and an in-house code was then used to stitch the results by numerically merging the data from each image location onto a common grid with interpolation. Each deformed image was

inevitably captured at a slightly different location from its reference image, thus each correlation gives a different rigid translation in the DIC displacement field results. Stitching these *displacement* fields together is problematic because very sharp gradients will occur at the seams. However, since *strain* is unaffected by rigid motion, strain fields *do not* have discontinuities at image boundaries. Stitching *strains* takes place after DIC is performed; consequently, there is no chance for the stitching procedure to affect the magnitude of the strain field. The only possible error caused by stitching in this manner is in the location of each individual DIC strain field relative to its neighbor. This can cause disagreement of strain contours on image boundaries, but the error is less than a pixel spatially and in terms of strain magnitude, it is within the inherent error of the DIC technique.

The locations of individual DIC strain fields in relation to one another can be easily obtained by stitching the reference images together to form a single large image. The image stitching program locates images with respect to one another with sub-pixel accuracy, and the locations of the DIC strain fields within these reference images are known exactly. Thus, the position of each strain field with respect to one another is known with sub-pixel accuracy. The relative locations of strain fields are rarely multiples of the subset spacing so strain fields are interpolated to an evenly spaced grid, which makes data processing more efficient.

5.2.6 EBSD and DIC Alignment

Finally, the strain and microstructure fields over the region of interest can be aligned using the fiducial markers from step 1. Because the indentation marks often do not appear very sharply in EBSD results, a more precise overlay is obtained through a two-step approach. First, grain boundaries are used to overlay EBSD results with images captured in the SEM using secondary electron imaging (in which both grain boundaries and Vickers indentation marks are

visible as shown in Fig. 5.1b). Second, the secondary electron image, and the overplayed EBSD data, is spatially aligned with the optical microscope reference images using Vickers indentation marks. Essentially, the SEM image is used as an intermediary to align the EBSD images with the optical microscope images.

Finally, the locations of DIC fields are, by definition, known with respect to the optical microscope reference images resulting in alignment between DIC and EBSD fields. Images of the region of interest from the optical microscope, secondary electron imaging, and from EBSD, are shown in Fig. 5.1(a-c), respectively.

Alignment between the secondary electron image and the optical microscope image can be achieved by adjusting the location, scale, and rotation of the SEM image to match the locations of the fiducial markers in both images. However, the three parameters of location, scale, and rotation alone are inadequate to align EBSD data with the SEM or optical microscope images. This is likely due to a number of factors including imperfect stitching of multiple EBSD scans, specimen drift during EBSD measurements, and perspective effects (*i.e.*, the effective imaging surface is not exactly parallel to the specimen surface). A more accurate alignment of EBSD data with the secondary electron image is achieved by using a local weighted mean transformation. With this method, 12 points are identified in the same physical locations in the SEM image and in an image of the EBSD data. The EBSD data is then transformed nonhomogeneously until the points in both data sets are aligned. As opposed to simply overlaying grain boundaries on top of strain fields, this technique spatially aligns EBSD and DIC *data* to allow for true quantitative comparisons of microstructure and strain fields.

5.3 Multiscale DIC Results for an *Ex Situ* Fatigue Crack Growth Experiment

The procedure detailed above was used to investigate the relationship between microstructure and strain accumulation in fatigue crack growth. A single edge notch tension specimen was machined with dimensions of 50 x 9 x 3 mm as shown in Fig. 5.1a. The 1.5 mm through-thickness notch was machined using electrical discharge machining with a wire diameter of 0.15 mm. The material is the nickel-based superalloy, Hastelloy X, that was described in chapter 4. To prepare the specimen for EBSD, it was finely polished with polishing powder down to 0.3 μm, followed by vibratory polishing with 0.05 μm colloidal silica. The region of interest, framed by Vickers microindentation marks, has dimensions of 700 by 800 μm and is located 3.05 to 3.75 mm ahead of the notch mouth, as shown in the optical microscope image in Fig. 5.1a.

The specimen was placed in the scanning electron microscope and imaged with secondary electron imaging which shows the grain boundaries and indentation marks. EBSD was then performed over the region of interest in a series of 9 scans. The results of secondary electron imaging and EBSD are shown in Figs 5.1b and 5.1c respectively. These measurements reveal several aspects of the microstructure of Hastelloy X in the as received condition (rolled). The material has equiaxed grains (at least in two dimensions) with an average diameter of 95 μm and a large variation in grain size. This average grain size is effectively reduced by a large number of annealing twins throughout the material (see Fig. 5.1c). Lastly, Fig. 5.1c shows no obvious preferred grain orientation indicated by the multitude of colors in the microstructure map.

After gathering microstructural information, the specimen was speckled using the powder method outlined in section 4.2. The region of interest was then imaged in the optical microscope as described by the procedure in section 5.2. At 50x magnification (0.087 μm/pix), 112 images were used to image the entire region of interest. The region of interest was also imaged at 10x

(0.44 μm/pix) using 4 images. Although a single image at 5x magnification (0.87 μm/pix) is sufficient to cover the entire region of interest, two overlapping 5x images were captured to cover the area from the notch tip to the end of the region of interest.

Using a servohydraulic load frame, the specimen was fatigue loaded at a rate of 2 Hz and a loading ratio, *R*, of 0.1 to initiate and grow a fatigue crack through the region of interest. In order to load the specimen with a relatively constant stress intensity range, the load was decreased periodically as the crack advanced. The nominal stress intensity range, ΔK, was 19 MPa$\sqrt{m}$ ± 2 MPa$\sqrt{m}$.

The crack path from the notch tip through the end of the region of interest is shown in Fig. 5.3. Fatigue loading was periodically interrupted when the crack tip reached points A through F marked in the figure. At these times, the specimen was removed from the load frame (unloading the specimen) to capture images of the region of interest outlined by Vickers indentations marks (circled in white in Fig. 5.3). The crack length and number of cycles for each set of images are given below the image in Fig. 5.3. In total, the crack grew through the region of interest, to a length of 3.7 mm, in 300,000 cycles.

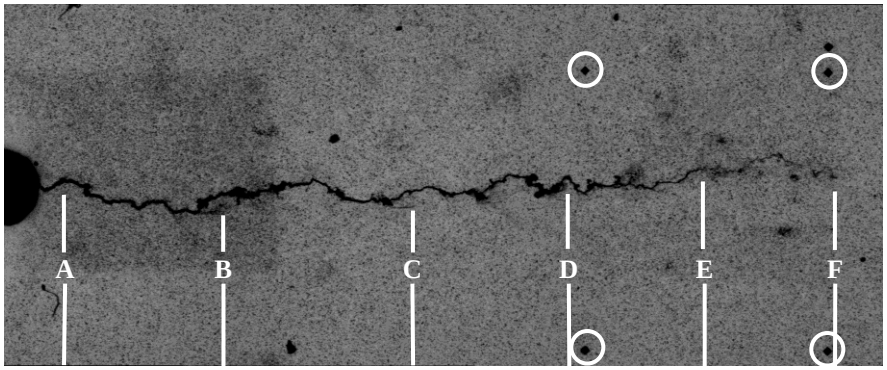

	A	B	C	D	E	F
Crack Length	**1.5 mm**	**2.0 mm**	**2.6 mm**	**3.0 mm**	**3.4 mm**	**3.7 mm**
Cycle	**25,000**	**65,000**	**91,000**	**194,000**	**248,000**	**300,000**

Fig. 5.3. Crack path from notch tip (left) through the region of interest outlined by Vickers indentation marks (circled in white). The specimen was removed from the load frame to image the region of interest when the crack tip was at locations A-F.

DIC was performed on these sets of images following the procedure outlined in section 5.2 in which each corresponding pair of images is correlated and then DIC strain fields are stitched together to obtain the strain field over the entire region of interest. For the DIC results in this chapter, the images captured at time A (just after crack initiation) were used as reference images, and subsequent images captured at times B through F were correlated as deformed images. Because these images (both reference and deformed) were captured at zero load, the strain measured by DIC only includes fatigue strain accumulation (*i.e.*, predominantly plastic strains).

The strain field perpendicular to the crack line, ε_{yy}, is plotted for the two-image 5x region for each removal time, B-F in Fig. 5.4. For reference, the region of interest (from Fig. 5.1a) is outlined by a black box and the crack tip location is marked by a white circle in each plot. These plots provide insight into the macroscopic strain fields associated with fatigue crack growth. The plastic zone is taller than the field of view at 5x as can be determined by noting the contour levels in Fig. 5.4. Because this *ex situ* technique only measures accumulated strain, any region with strain accumulation (say, above a threshold of 0.1% or so) has experienced plasticity. Plot F in Fig. 5.4 shows that nearly the entire imaged area accumulates strain as the crack grows; consequently, all regions shown in this chapter will be completely engulfed by the plastic wake as the fatigue crack grows. The minor exception is the lack of strain near the notch tip. While there is a significant amount of plastic strain in the vicinity of the notch tip, the reference image for these correlations was taken at time A, after crack initiation; therefore, no strain accumulation that occurred prior to time A is shown in these plots.

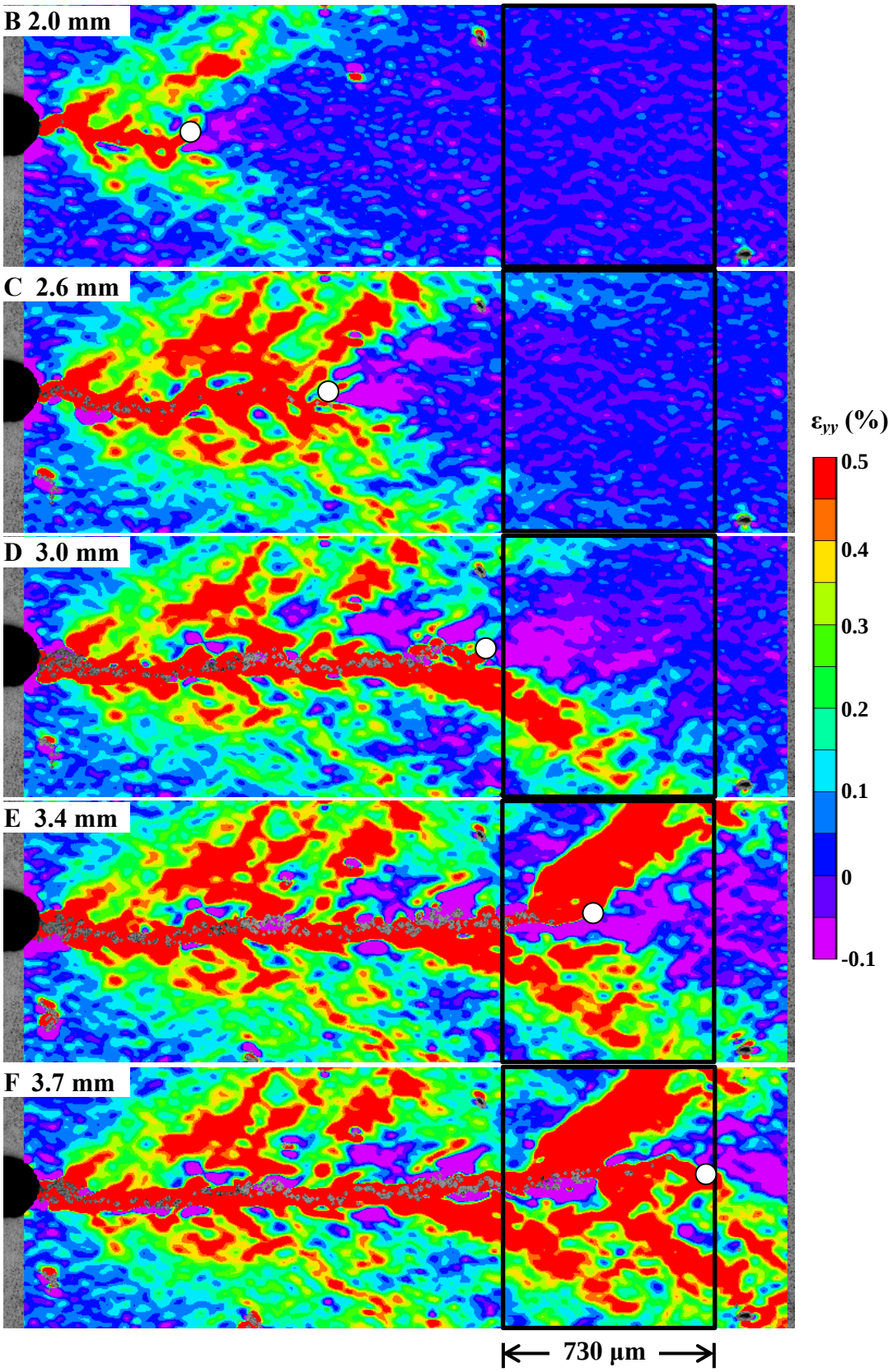

Fig. 5.4. Residual strain field, ε_{yy}, at 5x magnification covering a region from the notch tip past the end of the high magnification region of interest (outlined in black).

Also of interest are the details of the plastic wake seen in Fig. 5.4. When a crack is loaded monotonically, the plastic zone consists of two lobes of high strain emanating from the crack tip between the angles between ±(30° and 60°) (Dodds, 1991). Consequently, as a fatigue crack grows, it is expected to leave behind a continuous plastic wake with a height dictated by these lobes. However, as is seen in Fig. 5.4, the plastic wake consists of bands of material with strain accumulation interspersed with areas of little or no accumulated strain. These strain localizations are reminiscent of plastic zones associated with specific past crack tip locations. From Fig. 5.4, and in results shown later, it is evident that these lobes of high accumulated strain are often asymmetric. In addition, the strain accumulated as the crack tip passes a piece of material appears to be largely unaffected by further crack growth so that behind the crack tip, all of the strain fields in Fig. 5.4 essentially look the same.

At 50x magnification, DIC results were obtained using a subset size of 9 μm x 9 μm and a subset spacing of 0.9 μm producing 2400 correlation points within a typical 50 μm diameter grain. DIC was performed separately on each of the 112 pairs of images and the resulting strain fields were stitched together, as described in section 5.2.5, to obtain the strain fields over the entire region of interest. The improved resolution obtained by stitching 50x DIC strain fields is apparent from the comparison of the 50x ε_{yy} strain field at time E in Fig. 5.5 with results from 5x (with a subset size of 27 μm x 27 μm) and 10x magnifications (with a subset size of 23 μm x 23 μm). Fig. 5.5 clearly illustrates the improved accuracy of the method as magnification is increased by comparing the subset size in each case (shown in the lower left corner of each image). Note that 5x magnification is roughly the highest resolution at which the entire region can be captured with a single image. The 10x result shown in Fig. 5.5 is a combination of four DIC strain fields. The 50x results will be the focus of the remainder of this chapter.

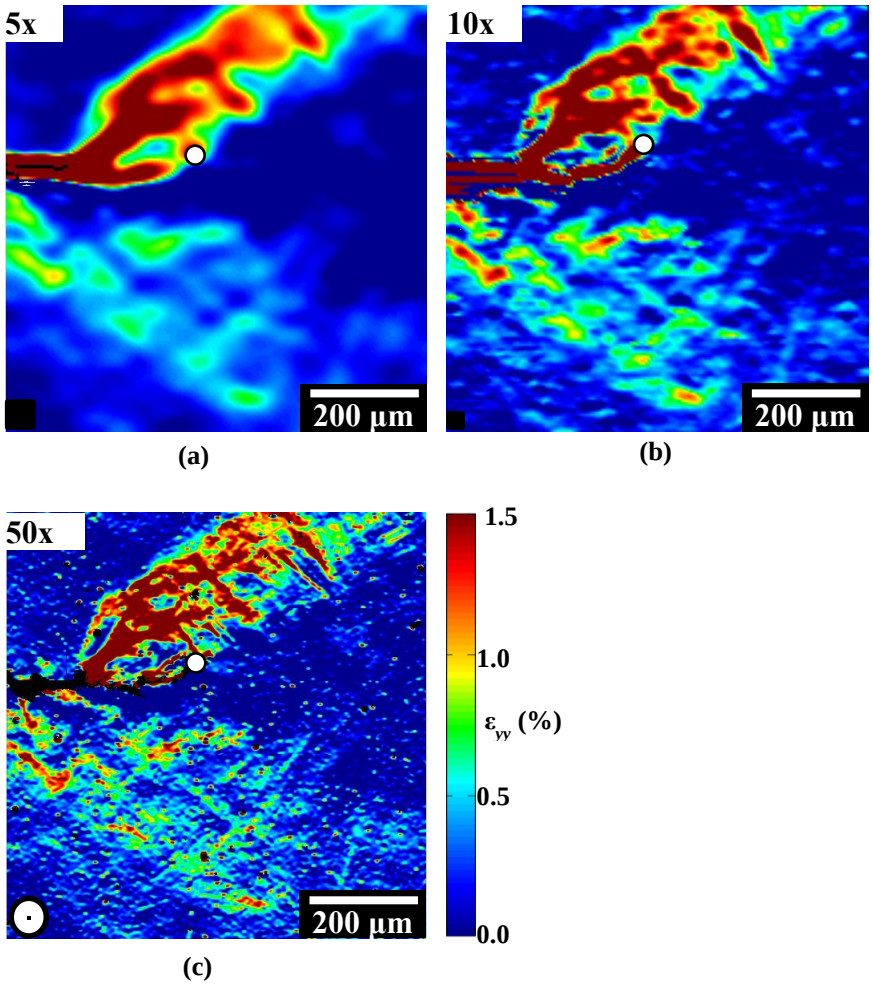

Fig. 5.5. Comparison of ε_{yy} strain fields from DIC obtained from (a) 5x, (b) 10x, and (c) 50x images at crack position E. Subset sizes are shown in the bottom left corner of each plot.

5.4 Strain Fields from *Ex Situ* Measurements at 50x

The 50x magnification stitched DIC ε_{yy} strain fields for crack tip locations C through F are shown in Fig. 5.6 with grain boundaries from EBSD results overlaid on top of them, having been aligned as discussed in section 5.2.6. For comparison, the crack path is drawn in white on plots E and F. As was observed at 5x magnification in Fig. 5.4, nearly all of the strain generated by the growing fatigue crack is contained within lobes of high strain that emanate from the crack tip at an angle near 40°. Consequently, the material directly ahead of the crack tip (between roughly ±25°) is relatively unstrained as illustrated by strain field C in Fig. 5.6 when the crack tip is 0.45 mm from entering the region.

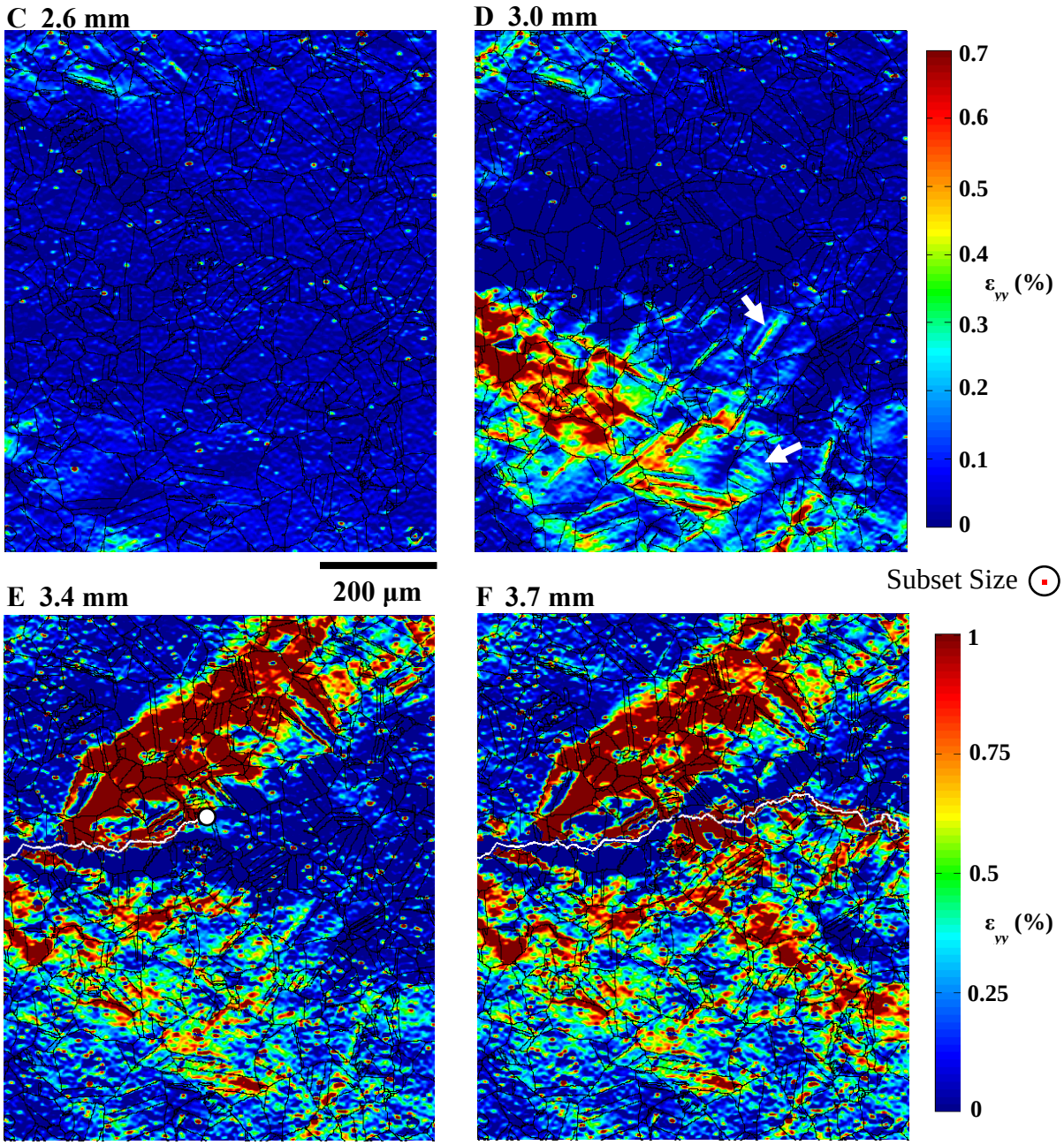

Fig. 5.6. Strain fields, ε_{yy}, with 50x resolution when the crack tip is at locations: C, 2.6 mm; D, 3.0 mm; E, 3.4 mm; F, 3.7 mm. The crack tip in strain field E is indicated by the white dot. The crack tip is no within the region for the other strain fields. The top contour level color bar applies to plots C and D, while the bottom color bar is for plots E and F.

At time C, the region is relatively strain free with the high strain lobes only beginning to enter at the corners. At time D, as the crack enters the region of interest, a lobe of high strain ahead of the crack tip appears within the region of interest. While there are generally two lobes

of high strain ahead of the crack tip, only the one below the crack line is apparent in strain field D since the formation of these lobes can be asymmetric. When the crack is at point E, a high-strain lobe above the crack tip has also developed. By the time the crack tip reached the end of the region of interest, time F, another lobe below the crack line has appeared. Within this region of interest, the strain localizations at angles between ±(30° to 60°) are in an asymmetric, staggered pattern on either side of the crack tip. For example, the strain field at D in Fig. 5.6 only shows a single lobe forming below the crack line with effectively zero strain in the corresponding region above the crack line.

There is a complex relationship between microstructure, strain fields, and crack direction with coupling between each of the factors. Because the crack is loaded under mode I conditions globally, it tends to grow straight. However, microstructural inhomogeneities cause deviations in the crack path that, in turn, lead to local mixed mode loading conditions. Mixed mode loading is likely the cause of the asymmetric strain lobes observed in Fig. 5.6. In turn, the strain lobes have an effect on the amount of mode mixity leading back to changes in the crack path.

In addition to these lobes of macroscopic strain localization, the strain fields in Fig. 5.6 also have inhomogeneities at the sub-grain level. There are localizations that occur on grain (and twin) boundaries, slip bands within grains, and grains that accumulate different levels of strain than their neighbors. These sub-grain level localizations will be further discussed in section 5.6.

Only the strain field perpendicular to the crack line, ε_{yy}, is shown in Fig. 5.6. The other in-plane components of strain, ε_{xx}, and ε_{xy}, are compared to the ε_{yy} strain field in Fig. 5.7 for image time F. Note that the plot of ε_{yy} strain in Fig. 5.7a contains the same exact data as the F plot in Fig. 5.6c, but with different contour levels representing compression as blue and tension as red (green is neutral). The crack path through the region is drawn again in white. A

comparison of Fig. 5.7a and Fig. 5.7b demonstrates that regions of high ε_{yy} strain (perpendicular to the crack line) experience high ε_{xx} strain (parallel to the crack line) as would be expected from a Poisson contraction effect. Shear strain, plotted in Fig. 5.7c, shows that regions with extreme normal strains also have extreme values of shear strain, but the sign of the shear strain varies throughout the high strain region.

A single scalar measurement of strain is the octahedral shear strain. Using the DIC strain fields, the octahedral shear strain field was computed using eq. 5.1:

$$\varepsilon_{oct} = \frac{1}{3}\sqrt{(\varepsilon_{xx}-\varepsilon_{yy})^2+z(\varepsilon_{yy}-\varepsilon_{zz})^2+(\varepsilon_{zz}-\varepsilon_{xx})^2+6(\varepsilon_{xy}{}^2+\varepsilon_{yz}{}^2+\varepsilon_{zx}{}^2)}. \quad (5.1)$$

Because only accumulated, essentially plastic, strain is measured, incompressibility is assumed for calculating the out-of-plane strain components:

$$\varepsilon_{zz} = -\varepsilon_{xx} - \varepsilon_{yy}, \qquad \varepsilon_{yz} = \varepsilon_{zx} = 0.$$

Consequently, the octahedral shear strain is a better measure of damage accumulation since it considers all three in-plane strain components simultaneously (with the assumption of incompressibility for the out-of-plane components). Octahedral shear strain accumulation, ε_{oct}, at time F is plotted in Fig. 5.7d. This plot is scaled from 0 to 1% strain since octahedral shear strain, by definition, cannot be negative. A comparison of this plot with the other plots in Fig. 5.7 shows that ε_{yy} dominates the octahedral shear strain values (Fig. 5.7a is very similar to Fig. 5.7d).

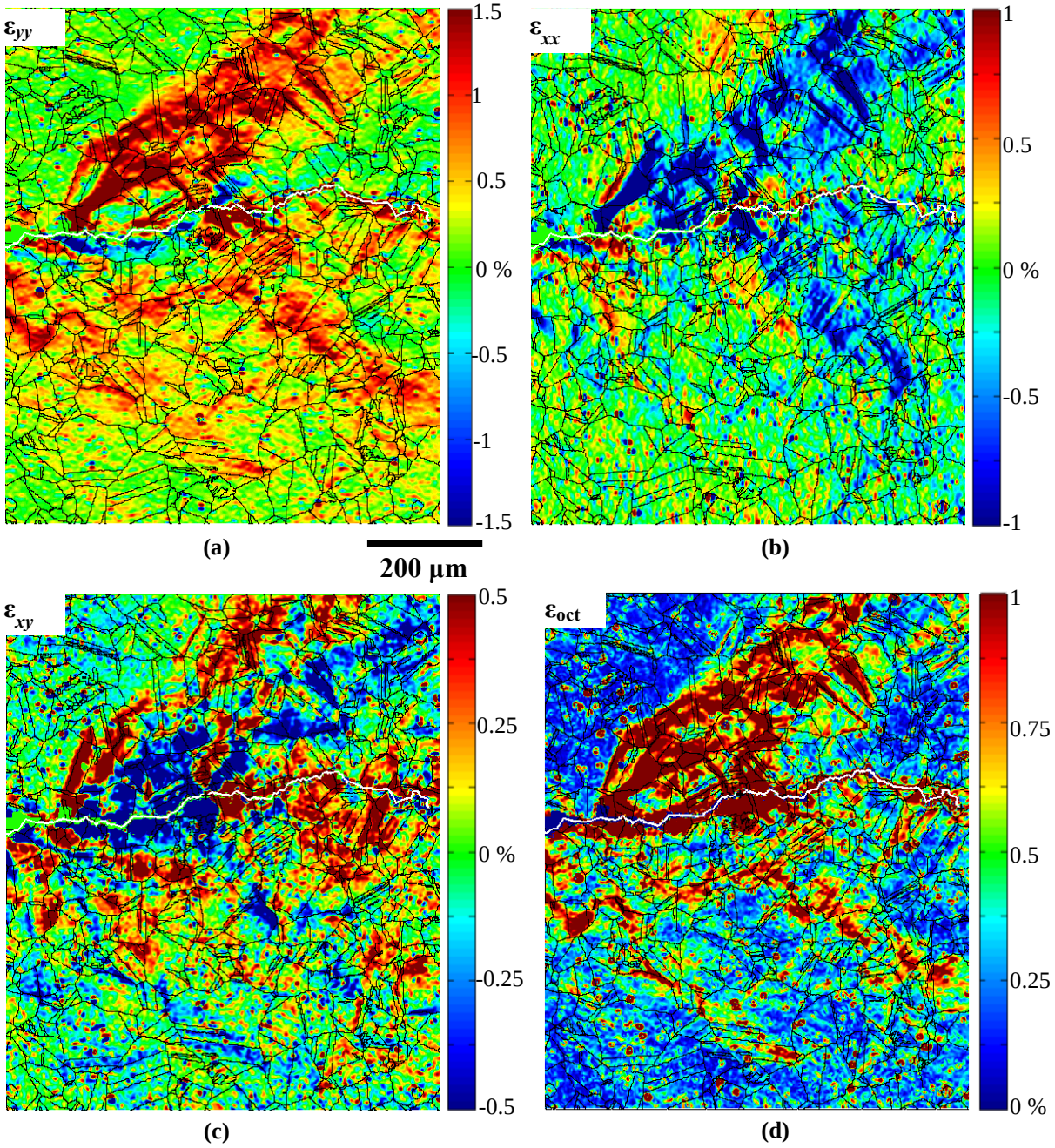

Fig. 5.7. Strain fields at removal time F. (a) ε_{yy} strain. The data in this plot is identical to plot F in Fig. 5.6, but with different contour levels. (b) Normal strain parallel to the crack line, ε_{xx}, (c) Shear strain, ε_{xy}, , and (d) Octahedral shear strain, ε_{oct}.

A more complete and detailed understanding of the octahedral shear strain field in Fig. 5.7d can be obtained by plotting the data with several different contour levels as shown in Fig. 5.8. Note that all four strain fields in Fig. 5.8 contain the same data as Fig. 5.7d. Finer details of

the high strain region can be seen in Fig. 5.8a which has contour levels from 0 to 2% strain. Note that the isolated occurrences of extremely high strain values appearing as red dots that are scattered far from the crack line can be traced back to specific speckles leaving the surface as loading progresses. As the maximum contour level is decreased, such as in Figs. 5.8b-c (with maximum contour levels of 1% and 0.5% respectively), the shape of the low-strain contours becomes clearer. In the extreme, scaling the contours from 0 to 0.25% in Fig. 5.8d shows that nearly the entire region of interest has accumulated fatigue strain.

Without examining the details of the strain field as was done in Fig. 5.8d, one might mistakenly conclude from Fig. 5.7d (and Figs. 5.6) that there are large amounts of unstrained material behind the crack tip. On the contrary, nearly the entire region observed at this magnification is yielded by the time the crack passes through it. Because strain is measured in the unloaded specimen, any measurable strain is essentially plastic strain accumulation. Plastic strain accumulation within the 50x region at times C, D, E, and F are shown in Fig. 5.9. In these binary plots, red represents plastically deformed material, defined as regions with octahedral shear strain above 0.1% (a threshold defined here to be definitely above the resolution of DIC). White areas have strain less than 0.1%, and the grain boundaries and crack line (at F) are drawn in black. Additionally, a binary plot of the 5x data at time F in Fig. 5.9, shows that the vast majority of the 5x region yields as the crack grows through the specimen. Note that this may be expected since the 5x region of interest is roughly 860 μm tall while the plane stress plastic zone size estimated from the Von Mises yield criterion is 920 μm tall.

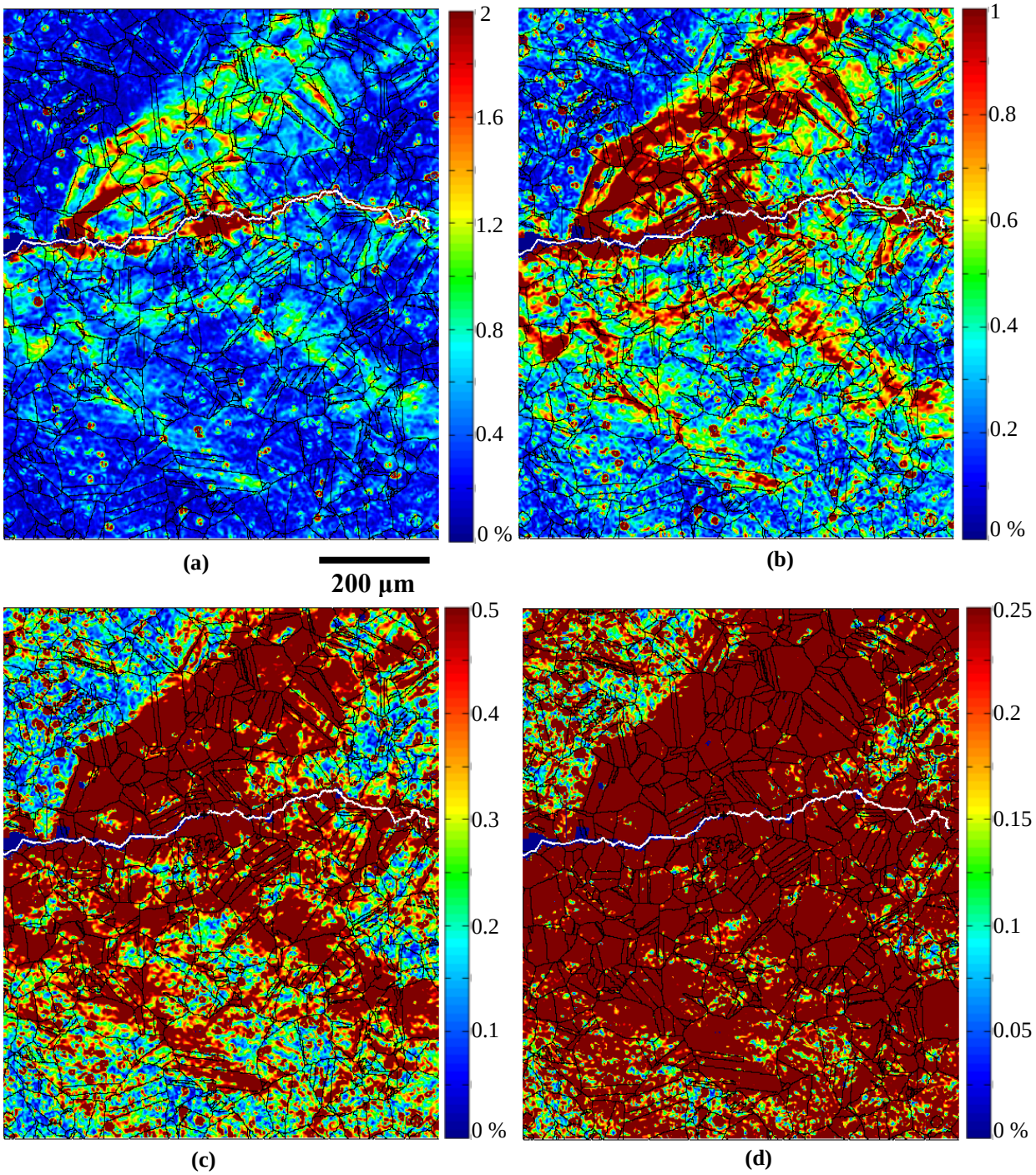

Fig. 5.8. Octahedral shear stress at time F with different contour levels to emphasize the heterogeneity in the strain field. (a) 0 – 2%, (b) 0 – 1%, (c) 0 – 0.5%, (d) 0 – 0.25%.

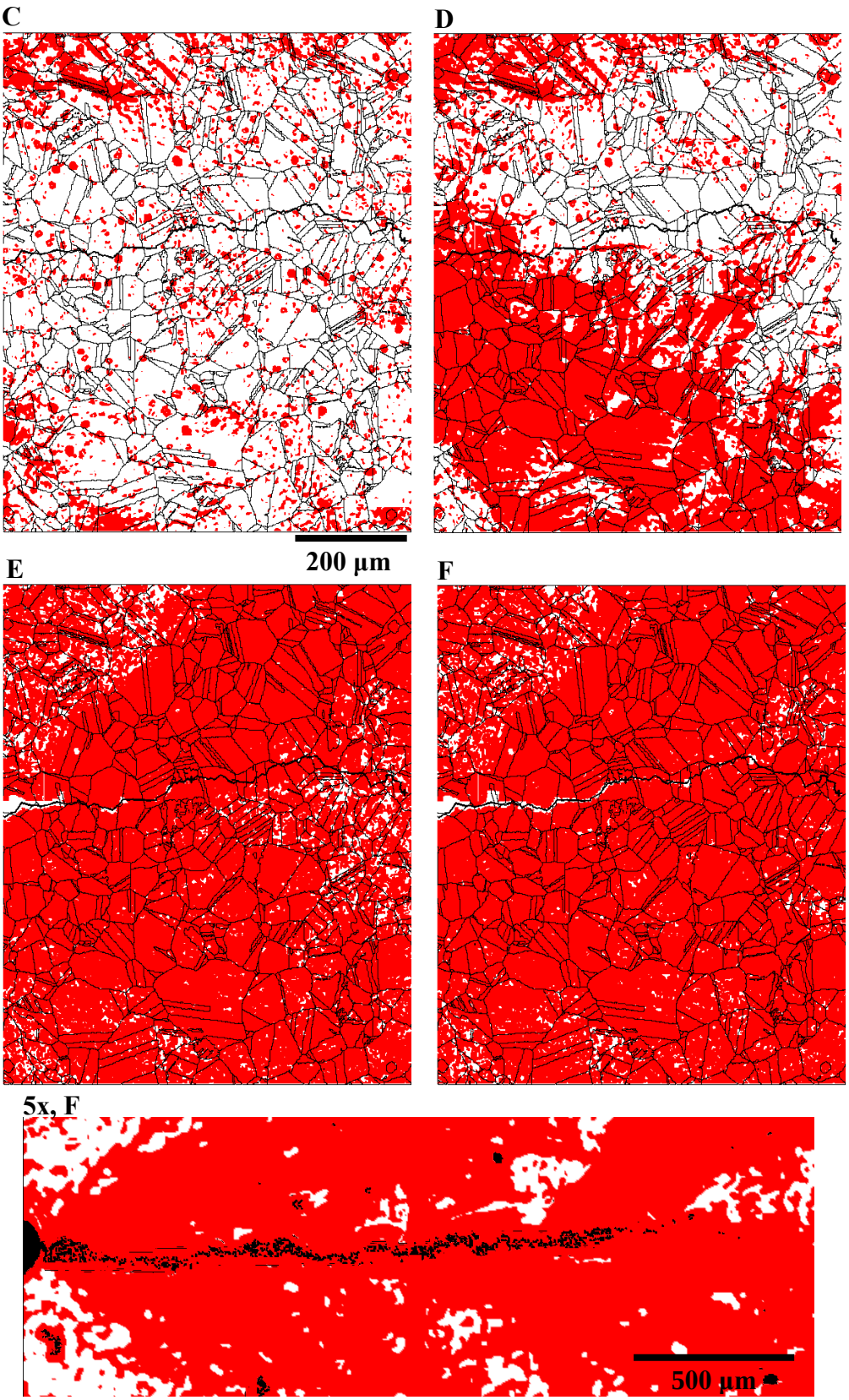

Fig. 5.9 Binary plot of yielded material (based on octahedral shear strain accumulation greater than 0.1%). Yielded areas are shaded red. The final crack location and grain boundaries are drawn in black.

5.5 Incremental Strain Accumulation

To obtain the full-field strain accumulation *between* imaging times, we subtract successive strain fields from one another. This is straightforward since all strain fields are in the coordinates of the reference image set (captured at time A). The octahedral shear strain accumulated between image times C to D, D to E, and E to F, are shown in Figs. 5.10(a-c), respectively. As the crack grew from point C to point D (Fig. 5.10a), a lobe of octahedral shear strain was accumulated below the crack line while very little strain was accumulated above the crack line. In growing from D to E, the crack generated a large amount of octahedral shear strain (note the contour levels in Fig. 5.10) above the crack line. From E to F the strain in the lobe above the crack line *relaxed* and strain was once again accumulated below the crack line. The plots in Fig. 5.10 indicate an alternating pattern of strain accumulation below then above the crack line. The 5x magnification results, strain field F in Fig. 5.4, indicate that this oscillation continues for the majority of the crack length. Additionally, the 5x results show that the oscillations within the region of interest are more extreme than those that preceded them. It appears that the opportunity for strain asymmetry may increase with crack length. On the other hand, the strain fields in the experiment shown in next chapter, with very similar conditions, have relatively symmetric strain lobes (Fig. 6.5). The most likely cause for the asymmetry is deviation of the local crack path resulting in mixed mode loading conditions that favor strain accumulation on one side of the crack (Saka and Tanaka, 1986). This can be seen by comparing the formation of strain localization with the crack path shown in white in Fig. 5.10.

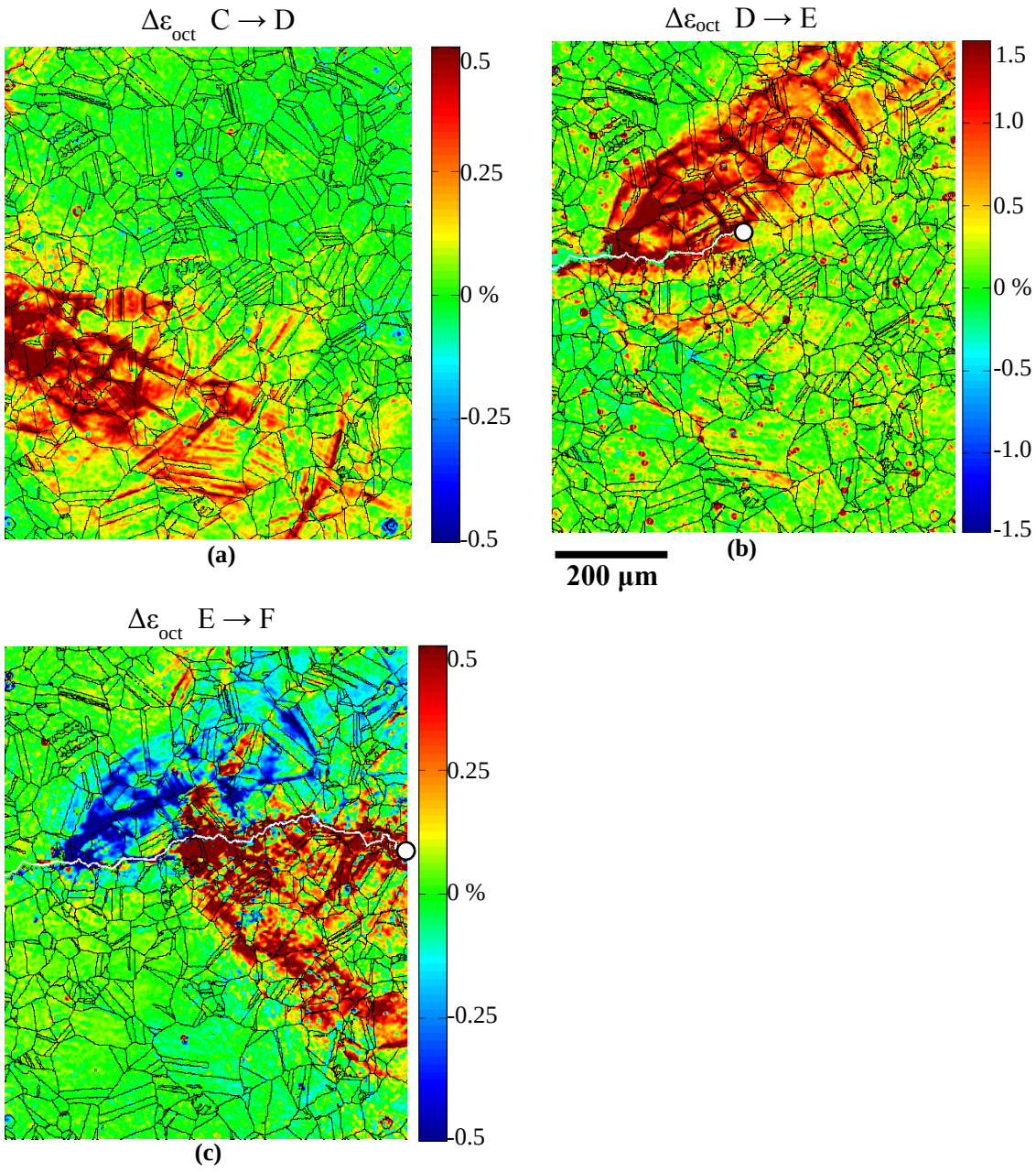

Fig. 5.10. Octahedral shear strain, ε_{oct}, accumulated between times (a) C to D, (b) D to E, (c) E to F calculated by subtracting DIC strain fields. The white dot in indicates the crack tip (when it is within the region).

An interesting feature in Fig. 5.10c is that the octahedral shear strain actually *relaxes* (by an amount on the order of magnitude of the yield strain) as the crack grows between times E and F. Since the strains measured here are accumulated strains captured at zero load, this implies that either reverse plasticity occurred within this region or that constrained elastic strains were dramatically relaxed with crack growth (which is less likely). It is suspected that the large strain

accumulation in lobe E and the subsequent reverse plasticity is associated with the mode I driving force for the crack. Deviations in the crack direction can cause asymmetric strain lobes, which in turn cause the crack to straighten again. As the crack straightens, it creates a strain lobe on the other side while relaxing strain in the first lobe (or, as this case apparently shows, even causing reverse plasticity in the first lobe). Thus, there is a coupling between crack direction and strain in the vicinity of the crack tip (Fagerholt *et al.*, 2010).

5.6 Relating Strains to Microstructure

Although the crack growth is transgranular, there are a considerable number of strain localizations that occur on both grain and twin boundaries. The strain plots in Figs 5.6 through 5.10 have grain boundaries laid on top of them allowing for a consideration of microstructural effects on strain localization in addition to the analysis of macrostructural featured discussed thus far. A portion of the plot of ε_{yy} strain at time E from Fig. 5.6 is magnified and rescaled in Fig. 5.11a to show details of strain localizations within the high strain lobe above the crack line. A region from this plot, outlined by a black box, is enlarged in Fig. 5.11b to show three strain localizations (indicated by arrows). By comparing these strain localizations with the grain boundaries that are overlaid on the strain field and with the portion of the grain orientation map shown in Fig. 5.11c, it is apparent that these localizations lie on both twin and grain boundaries.

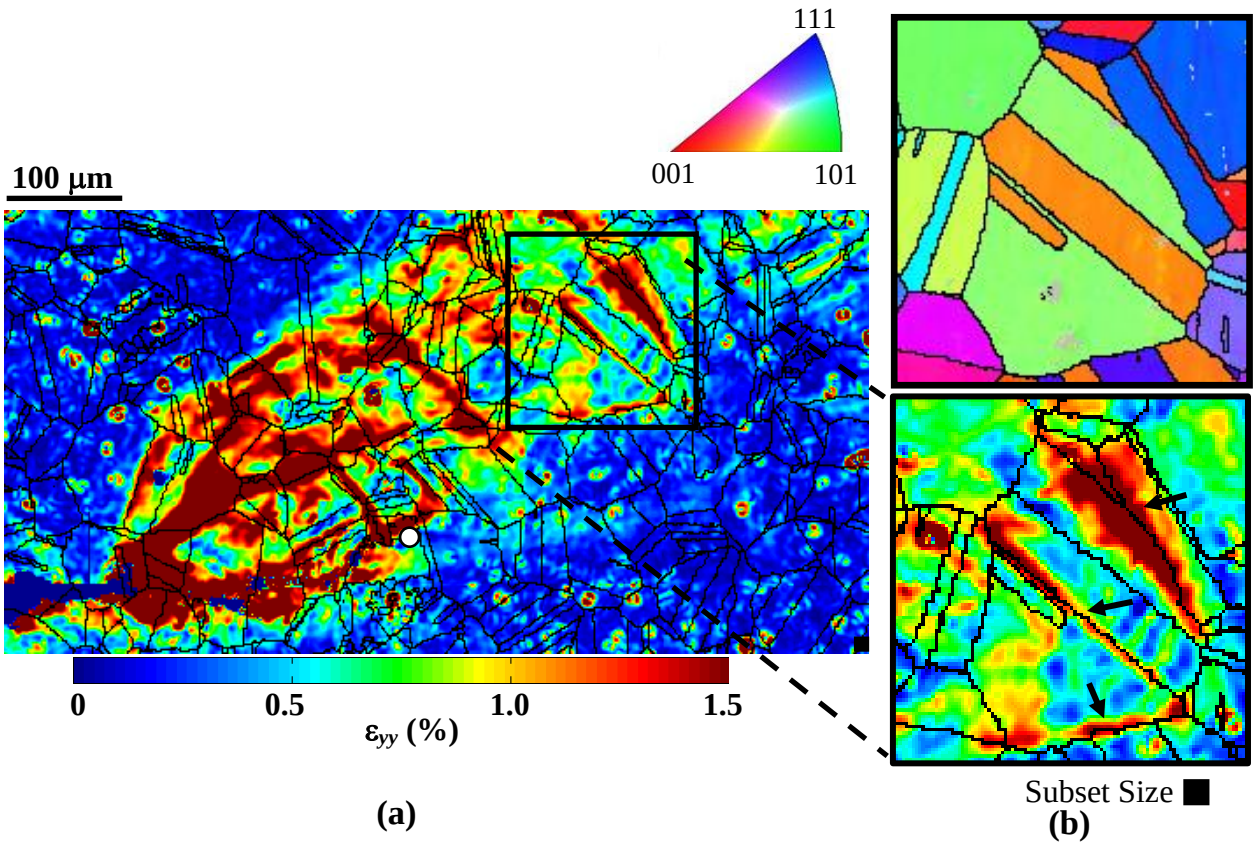

Fig. 5.11. (a) Contour plot of the ε_{yy} strain field at time E. Only the upper half of the field is shown here to increase the visible detail of strain localizations within the lobe of high strain. (b) A magnified portion of (a) outlined by the black box. Note the strain concentrations on two grain boundaries indicated by arrows. (c) Grain orientation map of the region shown in part (b).

Another cause of strain localizations are slip bands within grains. A good example of this is indicated by white arrows in plot D of Fig. 5.6. Within the strain lobe, several grains accumulate strain along slip bands. These appear as thin, parallel strips of high strain within a grain. As will be demonstrated in detail in the next chapter, slip bands often accumulate in the crack path, but they also occur within the strain lobes as shown in this work.

The crack path in relation to microstructure is drawn on the grain orientation map in Fig. 5.12 (which is a subsection of the plot in Fig. 5.1c). Transgranular crack growth is dominant although there are some instances where the crack grows along grain boundaries (circled in white). An interesting feature in this plot is that the crack is seen to abruptly change direction

within a grain. Occasionally, the directional change of the crack occurs as the crack approaches a twin or a grain boundary. Examples of this are illustrated by the black arrows in Fig. 5.12. This direction change is expected since boundaries like these are areas of strain accumulation (as seen in Fig. 5.6d for example) that provide resistance to crack growth. In other instances, the directional change of the crack occurs in the middle of a grain at a considerable distance from boundaries (although many boundaries are always in the extended vicinity). This occurs several times within the small section of material here as indicated by white arrows. In most of these instances, the crack direction follows slip bands at a steep angle compared to mode I loading. This direction soon becomes less energetically favorable and the crack changes direction to follow a different slip band within the grain that is more closely aligned with the mode I direction. Although this crack is long compared to the grain size (hundreds of grains), the local crack direction is still clearly influenced by microstructure.

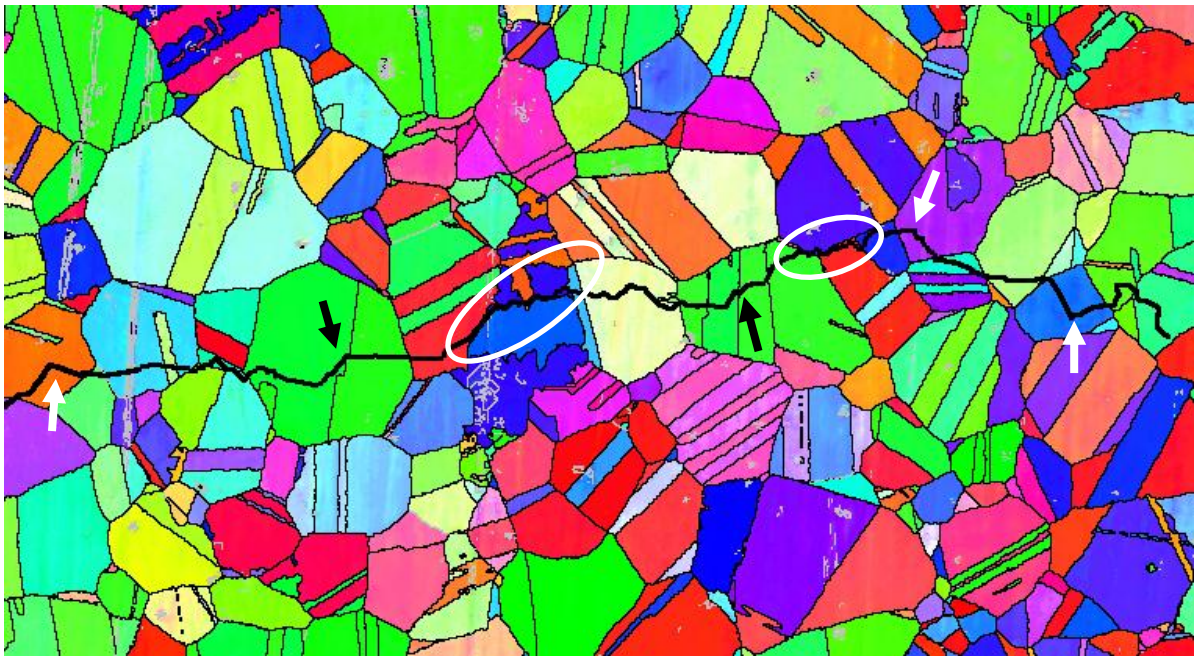

Fig. 5.12. Crack path in relation to grain geometry and orientation. This grain orientation map is a section of the plot in Fig. 5.1c. Crack growth is overwhelmingly transgranular, but occasionally follows grain boundaries (circled). The crack abruptly changes direction within a grain twice (white arrows). The crack changes direction around twin boundaries at the locations indicated by black arrows.

The average octahedral shear strain within a few grains in the dominant strain lobes was tracked as the crack grew through the region. These four grains are highlighted and numbered on the octahedral shear strain plot (at F) and on the grain orientation map in Fig. 5.13(b,c) respectively. The average octahedral shear strain within each grain is plotted against crack tip position in Fig. 5.13a. Grain 121 is below the crack line in the dominant lobe formed at time D. The plot of average ε_{oct} for this grain confirms that strain rose to around 0.9% at time D and remained relatively constant as the crack continued to grow. Grain 366, approximately symmetrically above the crack line from grain 121 shows no strain accumulation at time D due to the asymmetry of the strain lobes at D. However, when the crack grows to point E, the strain raises to 1.3% after which time it decreases by 0.3% as the strain lobe formed at time E experienced reverse plasticity. Grain 1044, in the top region of the dominant strain lobe formed at E, was also tracked. This grain appears to have moderate strain between a strong strain localization and a relatively low-strain region. This grain (1044) behaves in a similar manner to grain 366, but with lower magnitudes around 0.5%. Finally, grain 893 is below the crack in the strain lobe formed at F. This grain differs from the others in that it appears to build strain more gradually over several time increments. If the crack were grown further, the strain in grain 893 would be expected to plateau like the others since strain does not accumulate far behind the crack tip.

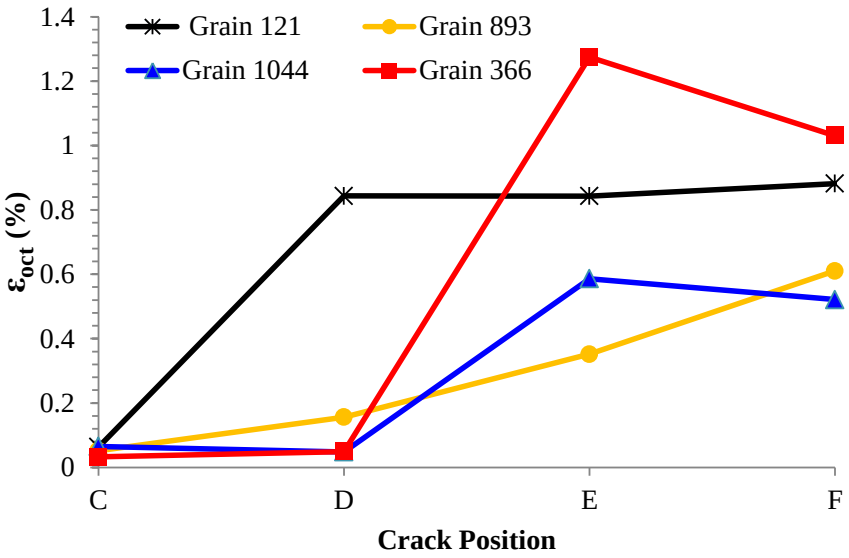

(a)

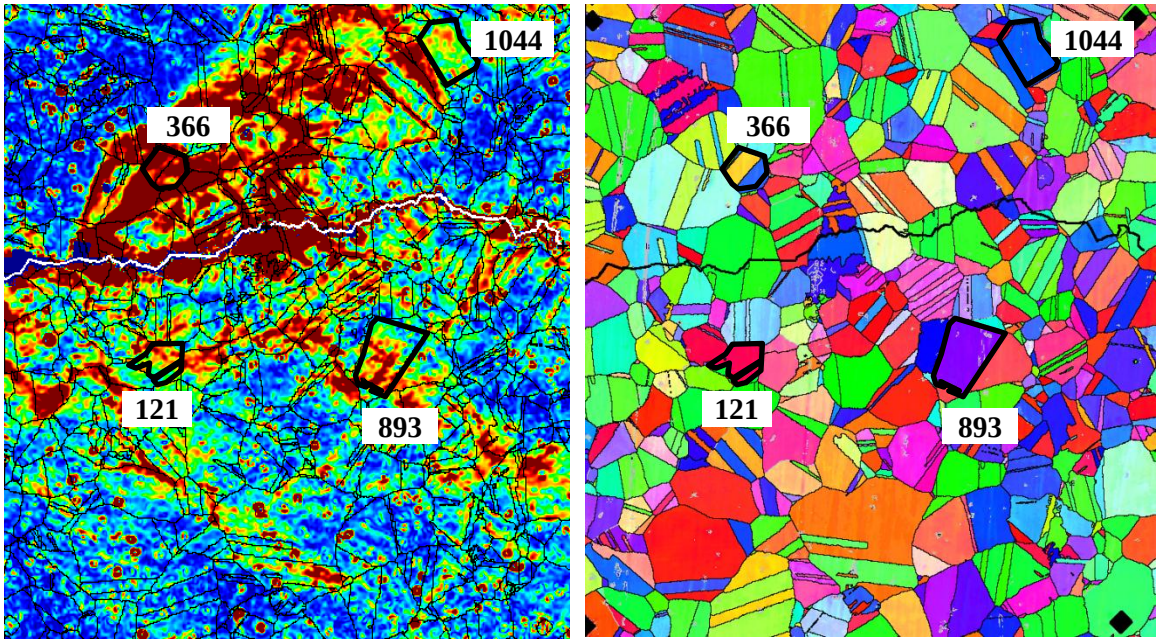

(b) **(c)**

Fig. 5.13. (a) Evolution of average octahedral shear strain within selected grains as the crack grows through the region. (b) Grains of interest highlighted on the octahedral shear strain field from Fig. 5.7d. (c) Highlighted grains on the microstructure map from Fig. 5.1c.

5.7 Summary

An *ex situ* technique was presented for measuring strains with sub-grain level resolution by stitching DIC results of multiple correlations of high magnification images. These sub-grain

level strain fields were then spatially linked to the underlying grain geometry and orientation from EBSD results. Using a combination of Vickers indentation marks and grain boundaries for fiducial markers was found to give excellent alignment accuracy.

This technique makes possible a quantitative investigation of the effects of microstructure on strain accumulation. DIC strain fields showed that all of the imaging regions are within the plastic wake of the growing fatigue crack. Localizations of fatigue strain near a growing fatigue crack were investigated, and almost no strain was found ahead of the lobes of strain that emanate from the crack tip. These lobes of strain accumulation were found to alternate in this case, possibly due to crack direction and mixed mode loading effects. Reverse plasticity was also observed to occur behind the crack tip of the growing fatigue crack. Enlarging a region of the results showed strain localizations along grain and twin boundaries within the plastic wake left by the growing fatigue crack as well as slip bands within grains. These localizations are instrumental in controlling the local crack path variations. An analysis of the average octahedral shear strain within a few selected grains showed that the strain increased and then plateaued as the crack passed.

Although these observations are quite interesting, there is no clear direct link between strain and grain orientation (or geometry). The asymmetric strain lobes and strong localizations within of the strain fields are certainly evidence that microstructure does affect the strain field. However, the location of each grain in relation to the crack tip is also a dominant factor that largely defines the strain field and convolutes the relation between strain and microstructure.

Chapter 6: *In Situ* and *Ex Situ* Study of Fatigue Crack Growth

In the previous chapter, an *ex situ* technique for linking DIC strains to microstructure was introduced and used to investigate strain inhomogeneities in the wake of a growing fatigue crack. This chapter will also study strain localizations in fatigue crack growth using the *ex situ* technique, but an *in situ* microscope mounted at the load frame provides real time strain measurements that give additional insight into how these localizations are initially formed and grow over time.

6.1 Experimental Procedure

The specimen geometry used in this part of the study is a single edge notched tension specimen with dimensions 50 x 7.0 x 1.55 mm, which is only half as thick as that used in the work described previously. The specimen thickness was reduced to allow the use of grips with more accurate alignment. As with the earlier work, the material used here is Hastelloy X. A 0.15 mm EDM wire was used to machine a 0.99 mm through-thickness edge notch. As with the previous chapter, the material studied here is Hastelloy X. The specimen was polished with increasingly fine silicon carbide polishing powders down to 0.05 μm followed by vibratory polishing with 0.05 μm colloidal silica. Using 0.05 μm silicon carbide powder made considerable improvements in surface finish compared to that obtained in the work described in chapter 5 where a 0.3 μm powder was used. The improved surface finish yielded much better quality (*i.e.*, less noisy) EBSD results. Once polished, two regions of interest were outlined by Vickers

indentation marks following the procedure outlined earlier. The first region of interest is located 1.84 mm to 2.31 mm ahead of the notch mouth with a size of 627 μm by 466 μm as indicated in Fig. 6.1. The second region is located 2.4 mm to 2.8 mm ahead of the notch mouth with a size of 629 μm by 413 μm. The reason for selecting two regions of interest, apart from obtaining more information from a single experiment, was to examine constant ΔK loading in region 1 and constant load, *i.e.*, increasing ΔK loading in region 2. The micrograph of the cracked specimen in Fig. 6.1 shows the speckle pattern and the location of these regions in relation to the notch tip and the crack line. Clearly, these regions were selected and marked before cracking the specimen, although region 1 was accidentally centered higher than region 2.

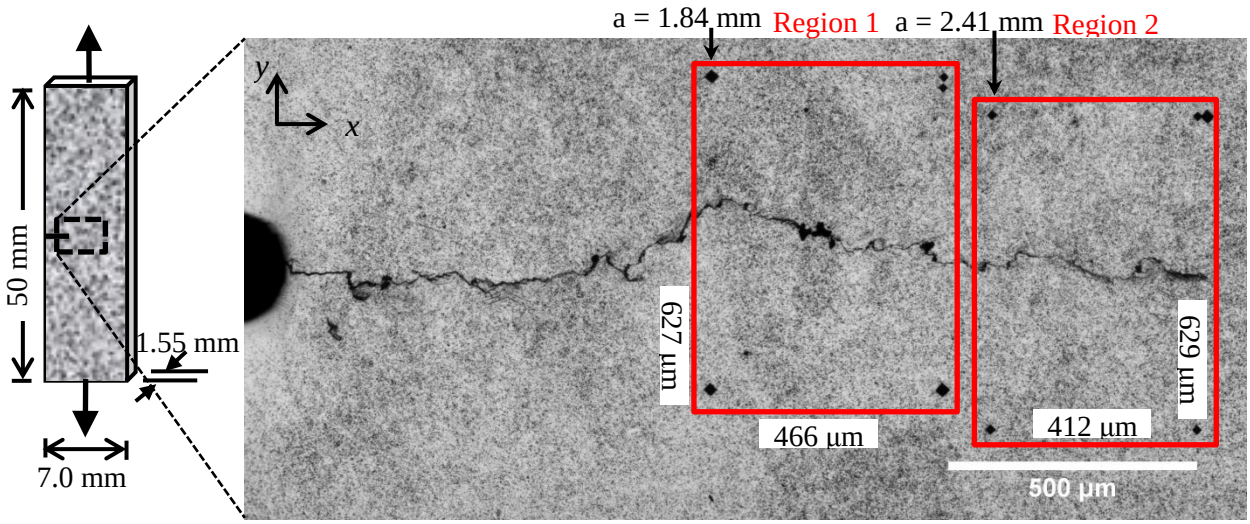

Fig. 6.1. Specimen dimensions and location of imaging regions in relation to the notch tip and the crack line. The regions were chosen before loading the specimen, but this image is taken after crack growth through both regions. Distances between Vickers indentation marks are noted on the image. Crack lengths at the left edge of each region are given above the image.

The specimen was placed in the scanning electron microscope, and microstructural information was acquired over both regions by stitching the results of 4 EBSD scans. Additionally, secondary electron images were acquired over both regions for alignment of EBSD results with DIC measurements (as described in section 5.2.6). The stitched microstructure maps of both regions are shown in their relative locations to one another in Fig. 6.2. Because the two

regions are so close to one another, there is a small amount of overlap between the areas covered by EBSD scans. The colors of the grains correspond to grain orientation with respect to the loading axis. The dark vertical lines are areas that were not indexed.

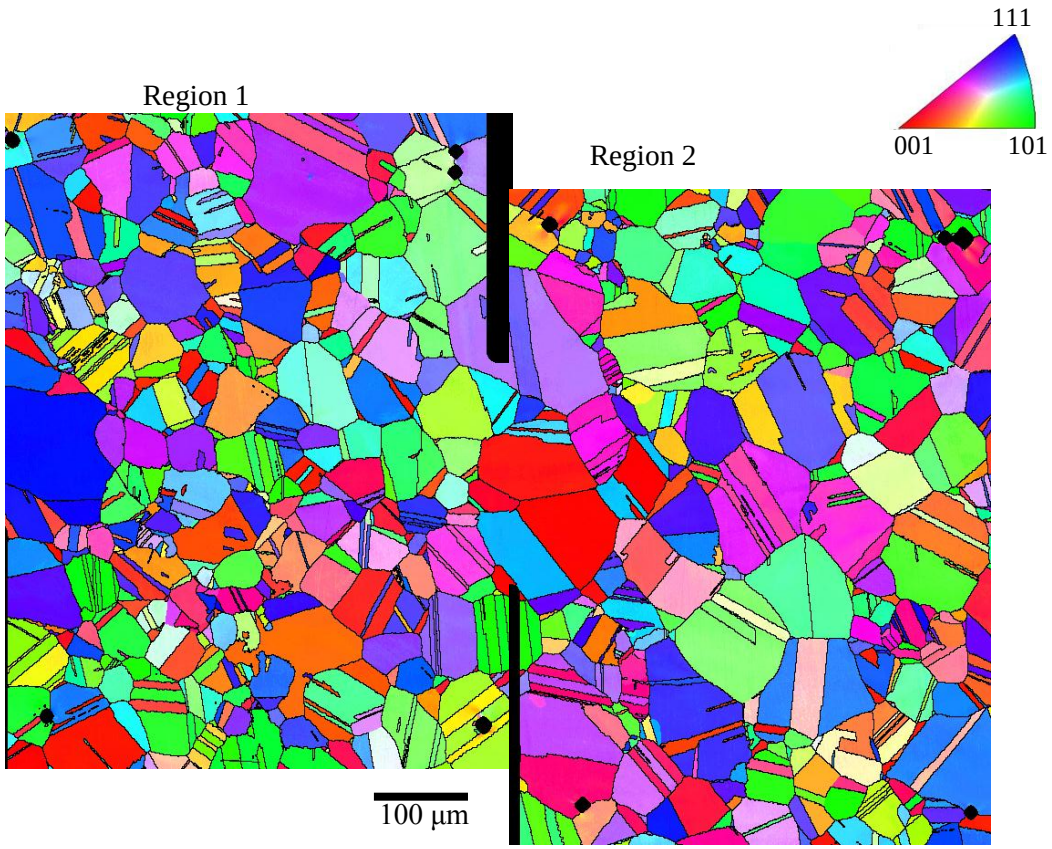

Fig. 6.2. Microstructure maps over both regions of interest. The regions are so close to one another that there is a small amount of overlap between the areas covered by EBSD scans.

After acquiring microstructural information, a speckle pattern was applied to the specimen using the powder method described in chapter 4. Before loading the specimen, images were captured at both 50x and 5x magnification for *ex situ* DIC (see Table 5.1 for image resolution at each magnification). At 5x magnification (0.87 µm/pix), a series of 8 images were captured to view a strip of the entire image width from the notch mouth to the right edge of the specimen. At 50x magnification (0.087 µm/pix), 36 images were required to image each of the two regions of interest.

The specimen was then placed in the load frame and fatigue loaded at a rate of 2 Hz to grow a fatigue crack. A crack initiated from the notch tip in 9,000 cycles and grew until entering region 1 around cycle 72,000. Before entering region 1, the specimen was loaded in constant ΔK loading with a range of 18.5 ± 0.5 MPa√m by periodically decreasing the load amplitude as the crack advanced. Upon entering region 1, the loading frequency was slowed to 1 Hz to facilitate image acquisition. As the crack grew across the first region of interest, ΔK was held constant at 18.3 ±0.3 MPa√m. The crack finished growing through region 1 at roughly cycle 149,000 spending a total of 77,000 cycles within the region.

The crack entered region 2 around cycle 166,000 and grew through the region for 42,000 cycles until exiting around cycle 208,000. When the crack tip was within the second region of interest, the fatigue loading was held at a constant *load* amplitude so that ΔK increased from 18.2 to 22.7 MPa√m (at 1 Hz) as the crack length increased. The minimum load was held constant at 0.2 kN throughout the entire fatigue loading so that the loading ratio, R, rose from 0.07 to 0.14 throughout the test.

During fatigue loading, images of the specimen were captured *in situ* by an optical microscope mounted on a 3-axis translation stage near the load frame as shown in Fig. 6.3a. The microscope objective is close to the specimen surface since it has a small working distance of a few millimeters (Fig. 6.3b). The primary advantage of an *in situ* optical microscope compared to conventional lenses is that it uses coaxial lighting making the speckle patterns appear sharper with fewer reflections, and leading to better DIC spatial resolution at comparable magnification. For example, compare a conventional lens 14x image in Fig. 4.8b to the 10x *in situ* microscope image in Fig. 6.4b. Because the image stitching used in the *ex situ* technique is not available for real time *in situ* measurements, the magnification of the *in situ* microscope was fixed at 10x

(0.44 μm/pix) in order to capture an entire region of interest in a single field of view. As a consequence, the spatial resolution of DIC measurements from *in situ* microscope images is not as high as the *ex situ* resolution. Additionally, DIC results from *in situ* measurements have more noise than *ex situ* measurements due to vibrations of the load frame. However, because the *in situ* images can be obtained without removing the specimen from the load frame or even slowing the fatigue loading, a much larger number of DIC measurements can be made throughout fatigue crack growth—thousands of *in situ* images are captured in this experiment compared to six *ex situ* images discussed in chapter 5.

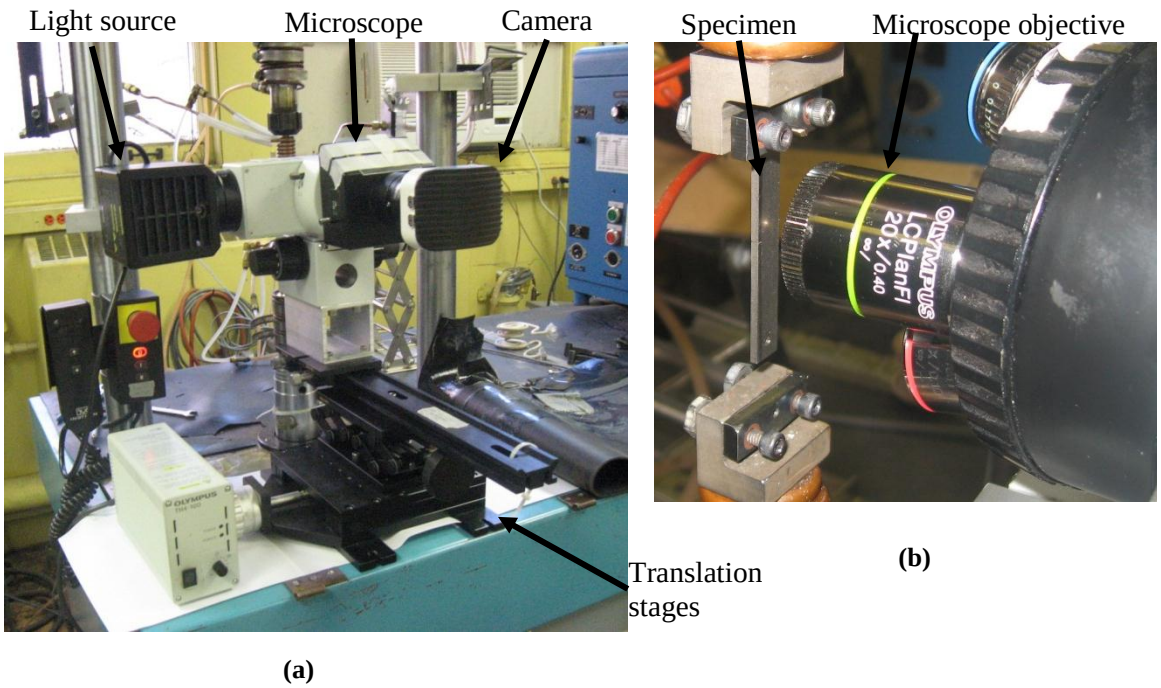

Fig. 6.3. (a) *In situ* microscope setup. (b) Close-up of microscope objective near specimen.

The speckle patterns at each magnification, both *in situ* and *ex situ*, are shown in Fig. 6.4 for region 1 (deformed images). At 5x magnification (Fig. 6.4a), a region significantly larger than the region of interest is captured, and a good speckle pattern is obtained. The *in situ* images at 10x magnification (Fig. 6.4b) are not as sharp as those taken with the *ex situ* microscope, most likely due to vibrations from the load frame, lens quality, or lighting differences. At 50x

magnification, the entire image array covering region 1 is shown in Fig. 6.4c, but this is a combination of 36 images, so the speckle pattern at 50x is more fairly compared to other magnifications by examining a single 50x image as shown in Fig. 6.4d. The speckle pattern at 50x is less dense and coarser than lower magnifications necessitating the use of larger subsets for DIC convergence, but as will be seen, even with the larger subset sizes, the 50x images yield better DIC spatial resolution than lower magnifications.

As the crack traveled through the two regions of interest, images were captured every 16 cycles. A loading rate of 1 Hz and an image capture rate of 15 frames per second allowed 16 images to be captured throughout each measurement cycle. However, because the depth of field of the microscope is small (around 100 μm with the 10x objective) the specimen goes out of focus throughout the loading cycle. The microscope was set to stay in focus when the specimen was near minimum load so that the *in situ* DIC in this work will only measure accumulated strain between images at minimum load.

DIC was performed on images obtained from the 10x *in situ* microscope at intervals of 64 cycles. A subset size of 22 x 22 μm (51 x 51 pixels) and a subset spacing of 2 μm (5 pixels) were used. As a result, roughly 1,200 full-field DIC measurements of the strain field within region 1 were made as the crack grew across the region of interest. Similarly, over 900 strain fields were obtained for region 2. These measurements allow for a detailed investigation of the evolution of full-field strains with crack growth. Because indentation marks are visible in the *in situ* images, these *in situ* DIC fields can be linked to microstructural measurements with the same procedure used in the *ex situ* technique.

After the crack had grown through both regions of interest, the specimen was removed from the load frame to capture a second set of *ex situ* optical microscope images. Again, eight

images were captured at 5x magnification and 36 images were captured at 50x magnification to cover each region. DIC was performed on these *ex situ* images and linked with microstructure.

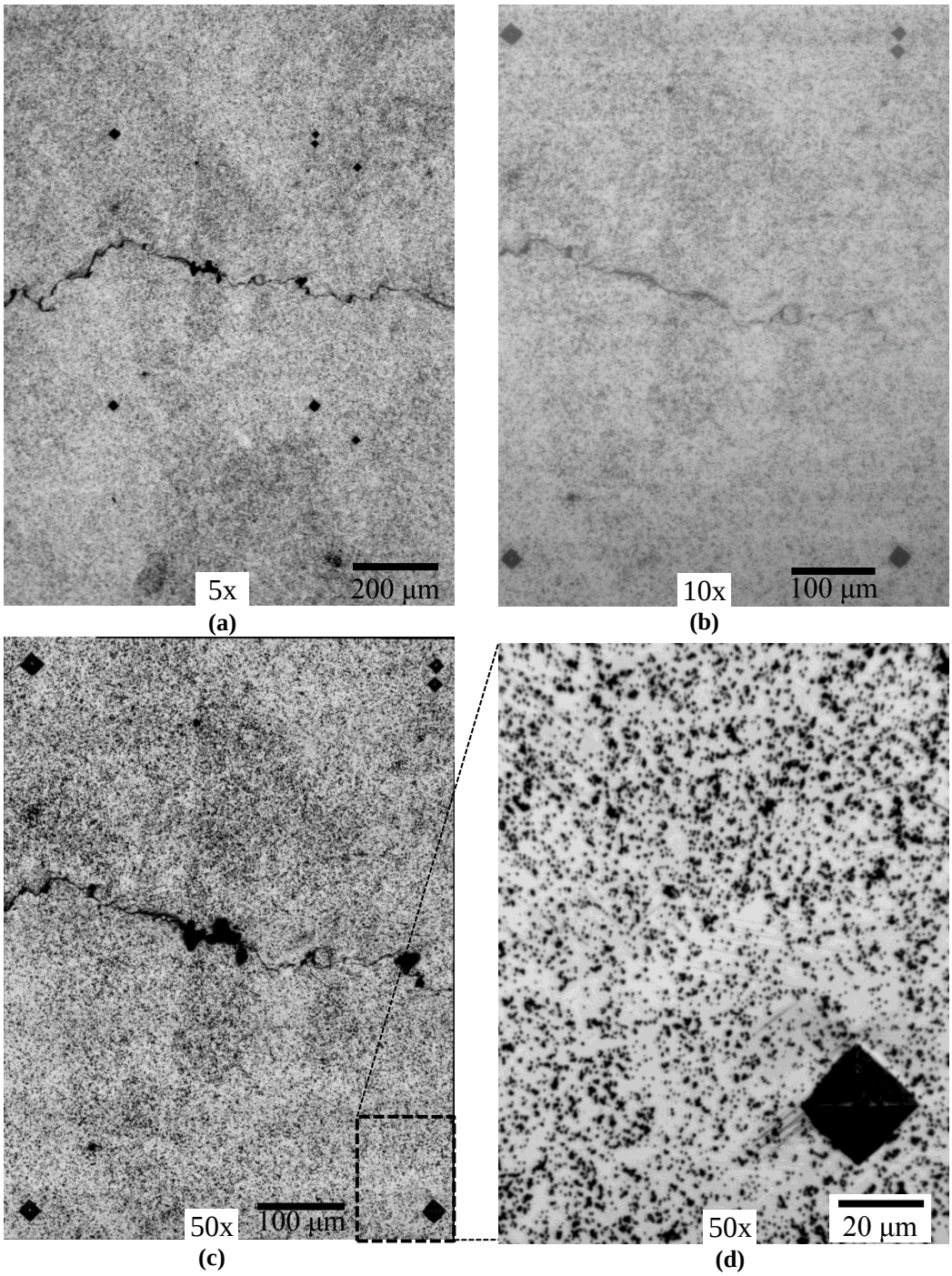

Fig. 6.4. Speckle patterns at various magnifications over region 1. (a) 5x *ex situ*, (b) 10x *in situ*, (c) 50x *ex situ* image array covering the entire region, (d) a single 50x *ex situ* image.

6.2 *Ex Situ* Strain Fields

Ex situ images at 5x magnification were correlated with a subset size of 27 x 27 μm (31 x 31 pixels) and a subset spacing of 4.4 μm (5 pixels). The ε_{yy} strain field (strain perpendicular to the crack line) across the entire specimen width is shown in Fig. 6.5a. Strain accumulation is limited to the material between the notch tip and the final crack tip location (*i.e.*, only elastic strains behind the notch tip and far ahead of the crack tip). This region, outlined in Fig. 6.5a, is enlarged in Fig. 6.5b to show details of the strain field in the wake of the fatigue crack. In contrast with Fig. 5.4, the reference image for this strain field was taken before crack initiation; consequently, the strains due to notch tip plasticity are also included in this strain field. The two regions of interest are outlined by black rectangles in Fig. 6.5b. The strain field in Fig. 6.5 does not exhibit the dramatic alternating asymmetric strain lobes that were observed in chapter 5. Instead, the strain field in Fig. 6.5 is more dispersed, but the strain does still appear to be faintly localized in lines at angles to the crack line between ±(30° to 60°). Additionally, there appears to be some degree of asymmetry in the strain field behind the crack line at a few places. In particular, there is a region of slightly compressed material just ahead of and below the upturn in the crack line before region 1 indicated by the white arrow in Fig. 6.5b.

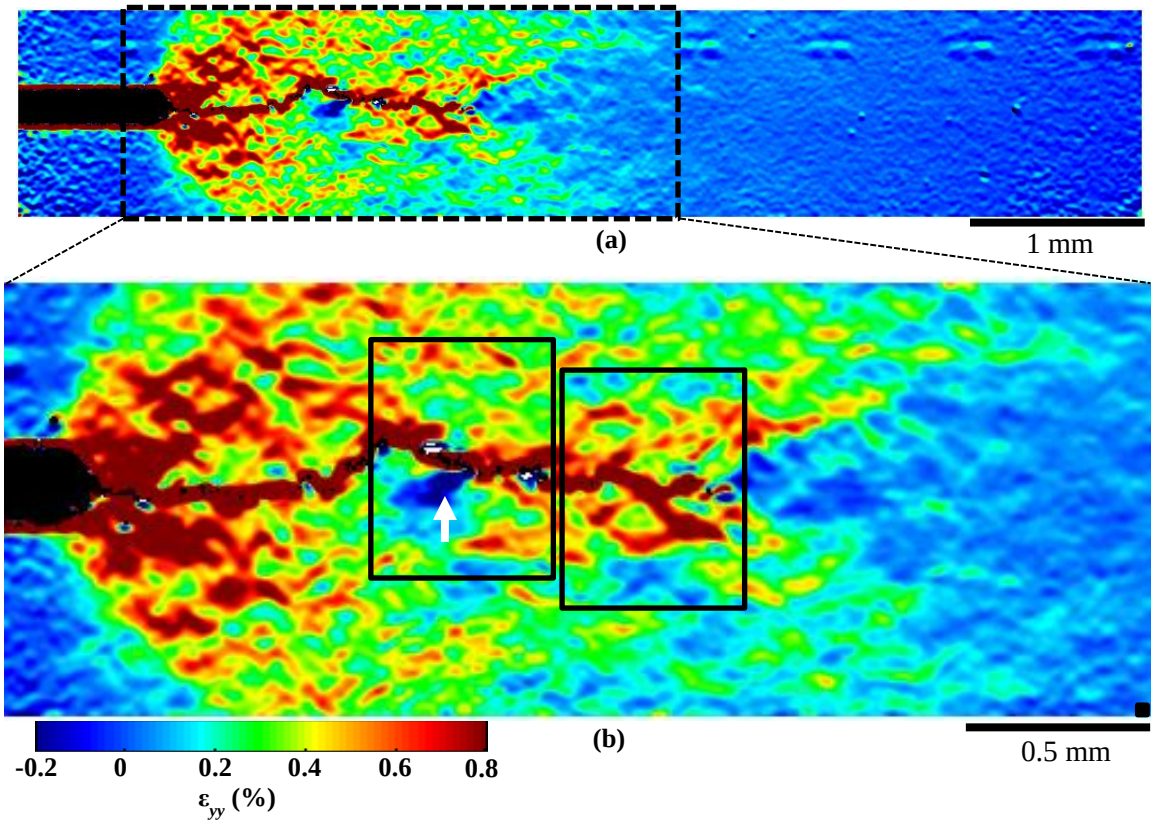

Fig. 6.5. *Ex situ* strain field, ε_{yy}, at 5x magnification. (a) Over the entire width of the specimen. (b) Region outlined in (a). Two microscale regions of interest are outlined in black.

At 50x magnification, *ex situ* images of both regions were taken after the crack had grown through the second region. These images were correlated with the images taken before any fatigue loading. DIC was performed using a subset size of 7 x 7 μm (81 x 81 pixels) and a subset spacing of 0.9 μm (10 pixels). These 50x *ex situ* correlations of each region provide strain fields with excellent spatial resolution – even better than those shown in chapter 5 because the use of smaller subset sizes was allowed here by an improved speckle pattern. In this chapter, only a single *ex situ* strain field is obtained for each region. Instead of removing the specimen at intervals, as was done the process described in chapter 5, an *in situ* microscope at 10x magnification was used to measure the development of strain fields over time (discussed later).

The 50x octahedral shear strain fields, ε_{oct} over regions 1 and 2 are shown in their relative location to one another in Figs. 6.6a and b respectively. The crack path through these regions is

drawn in white. The combination of these two regions covers an area roughly equal in size to the area observed in the experiment discussed in chapter 5. The 50x *ex situ* ε_{oct} strain fields in Fig. 6.6 show several types of strain localizations similar to those discussed in chapter 5. First, localizations are seen on grain and twin boundaries, indicated by number 1 in Fig. 6.6. Second, strain localizations are observed in slip bands within grains. Some of these slip bands change directions at twin boundaries as indicated by number 2. As indicated a point 3, some grains accumulated plastic strain in multiple active slip systems.

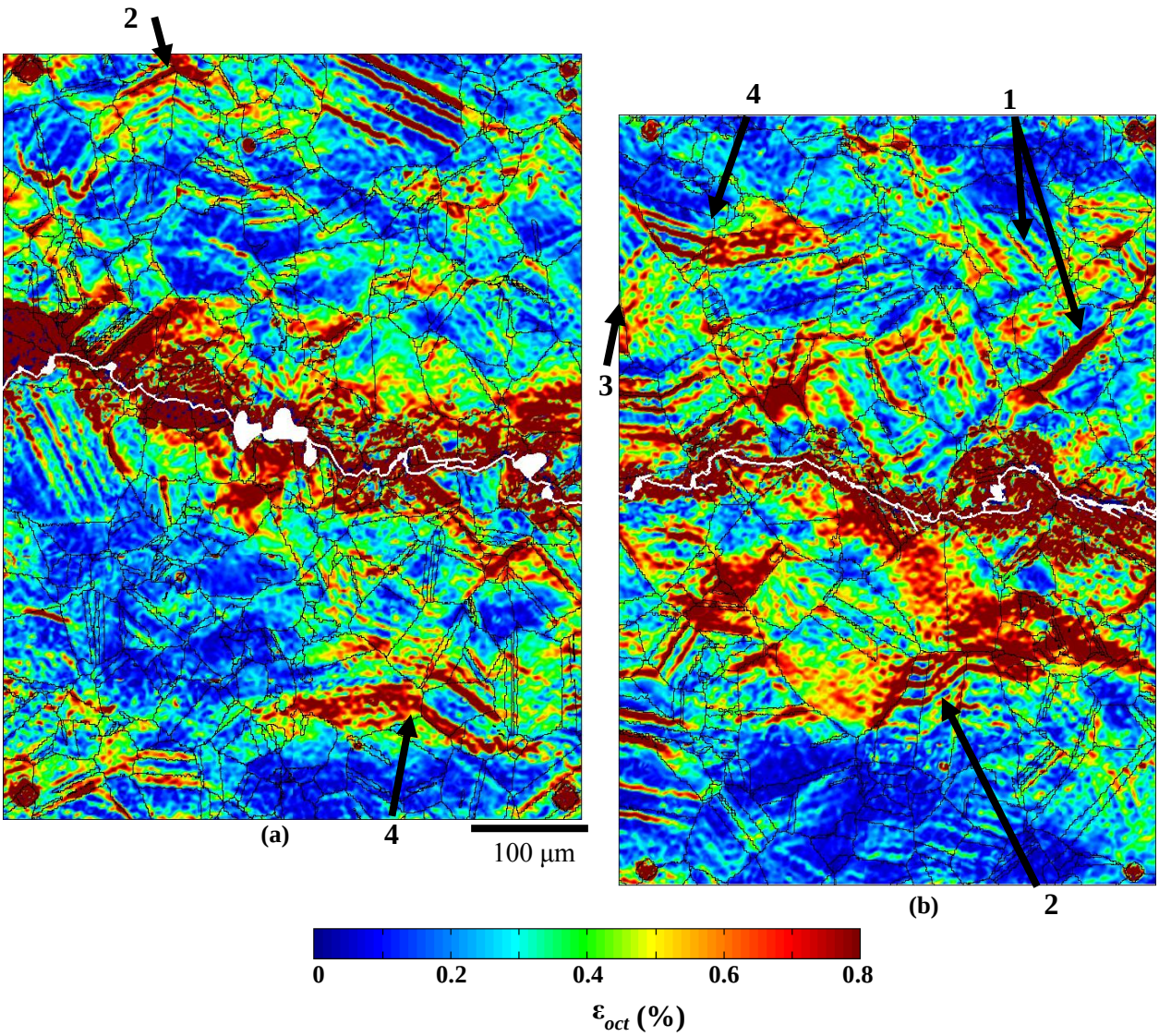

Fig. 6.6. *Ex situ* ε_{oct} strain fields at 50x magnification. (a) Region 1, (b) Region 2.

Strain localizations in this experiment appear to be somewhat evenly dispersed throughout the imaging region. Some relatively unstrained regions are visible in Fig. 6.6, but there are not lobes of high and low strain that were observed in chapter 5. The strain localizations shown here are primarily in the form of slip bands, but there are a few concentrations on grain boundaries. Many of these strain localizations extend over collections of several grains. Two examples of this are at points 4 in Fig. 6.6 where slip bands cross grain boundaries to grow through multiple grains. The slip systems of these grains are probably well aligned for transferring slip across boundaries so that a cluster of grains behaves like a single grain. This behavior was observed for microcrack nucleation in a nickel alloy by Davidson *et al.* (2007) and discussed extensively. Similar behavior was observed in dynamic loading in Padilla *et al.* (2011) and in cyclic plasticity in Efstathiou *et al*. (2010). Abuzaid *et al*., (2011) analyzed the conditions for slip transfer across grain boundaries based on measurements obtained with the *ex* situ procedure described in chapter 5. They found a relation between slip transmission and residual Burgers vector.

Observation of the ε_{yy} strain fields in Figs. 6.7b and 6.8b reveals that they are qualitatively very similar to the octahedral shear strain plots in Fig. 6.6 indicating that ε_{yy} strains dominate the values of ε_{oct}. A line scan was performed at the location of the black line in Fig. 6.8b to examine the variation in strain across these slip bands. In Fig. 6.9, ε_{yy} strain along this black line is plotted against distance from the top of the line. The contour plot in Fig. 6.8b shows four high-strain slip bands in the top half of this grain and several slip bands with less strain accumulation in the bottom half. This is confirmed by the Fig. 6.9 line plot by four peaks reaching strain levels of 1.8%. Four less intense bands observed in the bottom half of the grain

with peak strains reaching 0.5%, 0.6%, 0.2%, and 0.1%. Measured strains between the four major slip bands is close to 0% indicating that the slip bands shield adjacent material from strain.

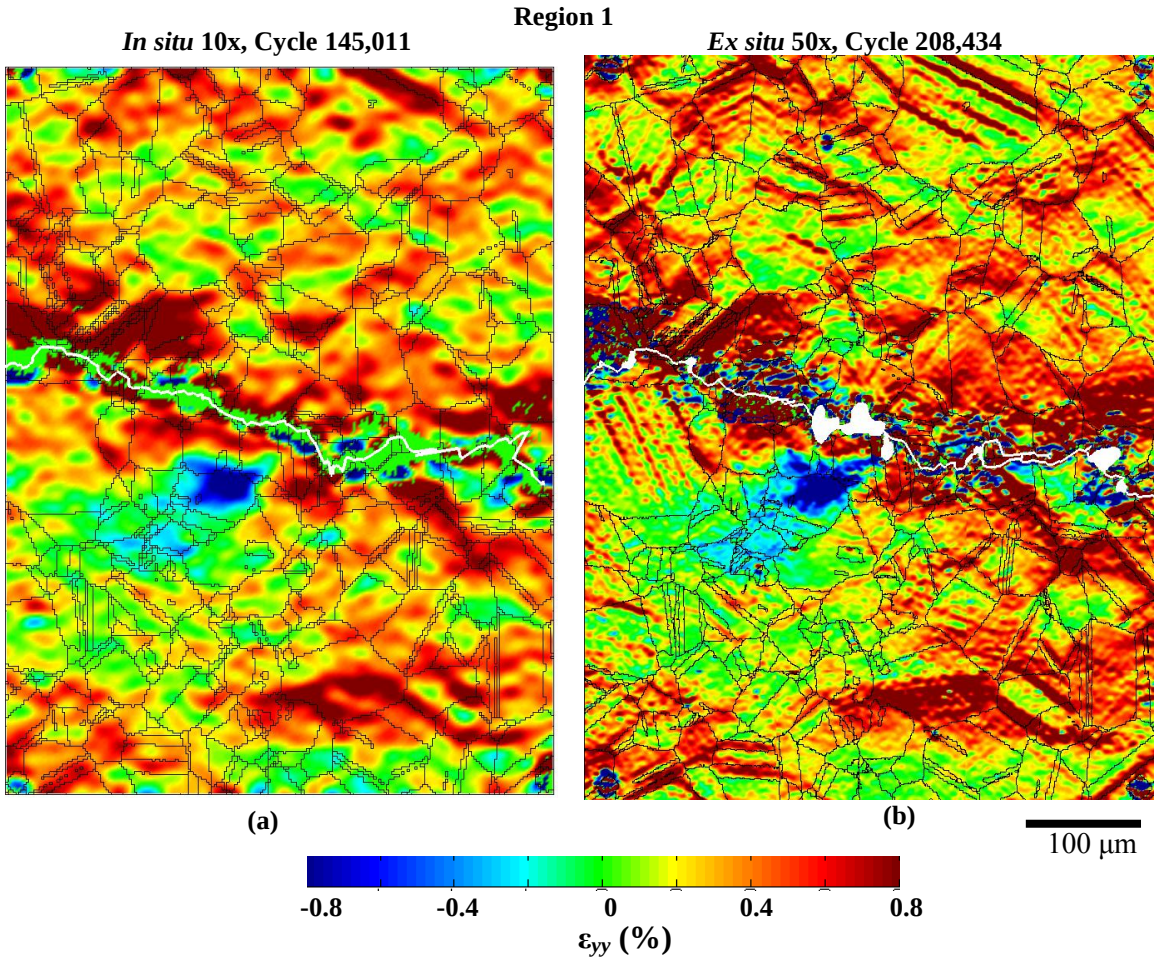

Fig. 6.7. Strain field ε_{yy} after the crack had grown through region 1 (a) *in situ* (b) *ex situ*.

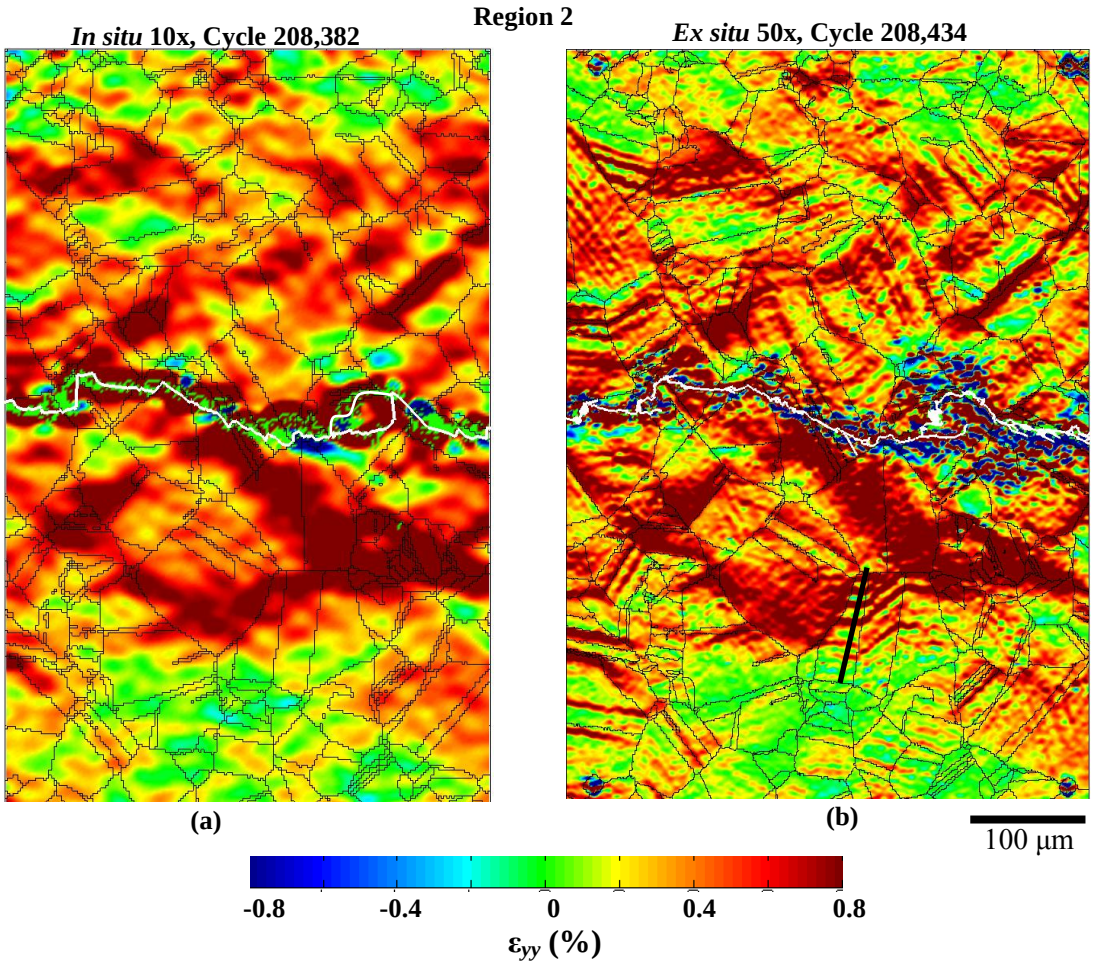

Fig. 6.8. Strain field ε_{yy} after the crack had grown through region 2 (a) *in situ* (b) *ex situ*. The black line in (b) corresponds to the line plotted in Fig. 6.9.

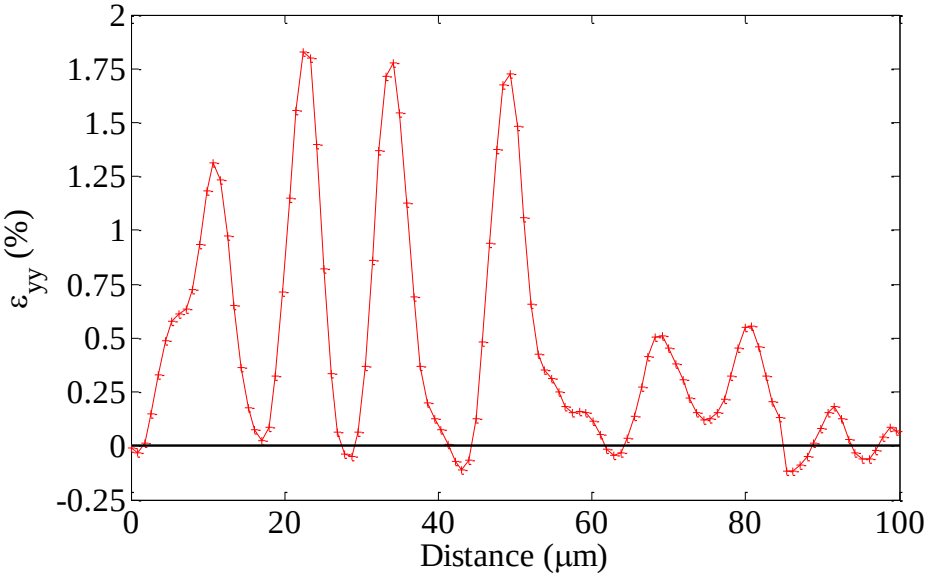

Fig. 6.9. Line scan along black line shown in Fig. 6.8b. Distance is measured along the line starting at the top. ε_{yy} strain within slip bands is around 1.8% while it is roughly zero in between slip bands.

6.3 *In Situ* Strain Fields

The 10x *in situ* images captured throughout fatigue loading were correlated using a subset size of 9 x 9μm (21 x 21 pixels) and a subset spacing of 2.2 μm (5 pixels). The 10x and 50x ε_{yy} strain fields throughout region 1 are compared in Fig. 6.7. Both of the plots in Fig. 6.7 also show the compressive region below the crack that was observed in *ex situ* 5x measurements in Fig. 6.5. Note that there is a difference of about 63,000 cycles between the two results, which corresponds to the time it takes for the fatigue crack to enter and traverse region 2. Nonetheless, the residual strain fields look similar, within their differing resolution, indicating that little additional damage occurs once the crack has passed. Similarly, region 2 is shown in Fig. 6.8 as the last frame of the *in situ* measurements compared to the *ex situ* result.

From Figs. 6.7 and 6.8, it is again clear that the 50x results have far better resolution. The physical subset size used for the 10x results (9 x 9 μm), is comparable to the 50x subset size (7 x 7 μm), but the subset size alone does not determine the spatial resolution of DIC results. One factor giving higher resolution at 50x is subset spacing. The subset spacing at 50x is 0.9 μm compared to 2.2 μm for 10x. A superficial view of subset spacing would lead one to conclude that reducing the 10x subset spacing to 1 pixel (0.4 μm) would give equal resolution between 10x and 50x results. However, it has been found that reducing subset spacing below 5 pixels does not measurably improve resolution. Perhaps more important than subset size or subset spacing is pixel size. Each subset at 50x contains roughly 15 times as many pixels as the 10x results that could account for both a higher signal-to-noise ratio and higher spatial resolution. Less noise and higher spatial resolution in the *ex situ* 50x results could also be partly be due to the fact that the speckle pattern appears sharper in the *ex situ* microscope than the *in situ* microscope as shown in Fig. 6.4 (possibly resulting from lighting conditions or lens quality).

Although the *in situ* 10x DIC results do not have the excellent spatial resolution obtained at 50x, they do indicate strain localizations at the same locations as the 50x results. The advantage of these *in situ* DIC measurements is their excellent temporal resolution. *In situ* DIC fields can be obtained every 16 cycles with the current measurement system, with 16 images taken in each cycle (although not all are in focus). This yields thousands of temporal snapshots of the strain field as the crack grows across a region. In contrast, *ex situ* measurements require the time consuming steps of removing the specimen from the load frame and capturing image arrays. Consequently, a combination of *ex situ* and *in situ* DIC measurements can give a more complete understanding of these strain fields—the 50x results give high resolution measurements of the final strain fields, and the 10x *in situ* measurements indicate the time at which each strain localization first appeared.

As mentioned, *in situ* images were captured every 16 cycles as the crack grew through each region, but only a few selected cycles can be shown in this document because of space limitations. In Figs. 6.10 and 6.11, ε_{yy} strain fields at six selected times are shown for regions 1 and 2, respectively. These six snapshots in each figure, at the cycles indicated, provide an accurate indication of strain evolution with crack location. When the crack is within the region of observation, the crack line is drawn in white with a white circle indicating the crack tip. When the crack tip has not yet entered the region, its location relative to the leftmost indentation marks of the region is indicated in the caption.

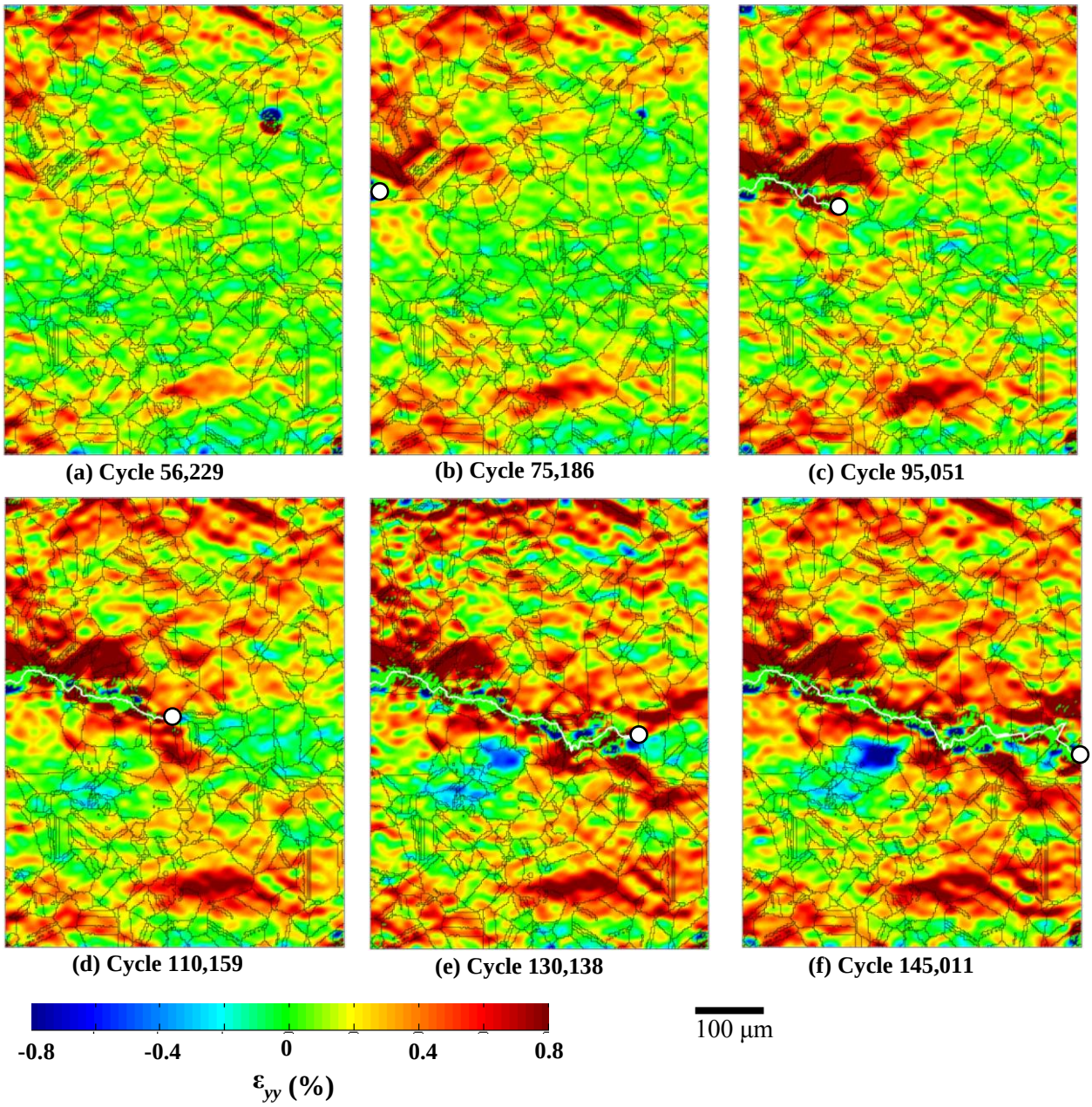

Fig. 6.10. Evolution of *in situ* ε_{yy} strain field throughout region 1. (a) Crack tip is 180 mm from entering the region, (b-f) Crack tip is indicated by white dot. Cycle numbers are indicated below each strain field.

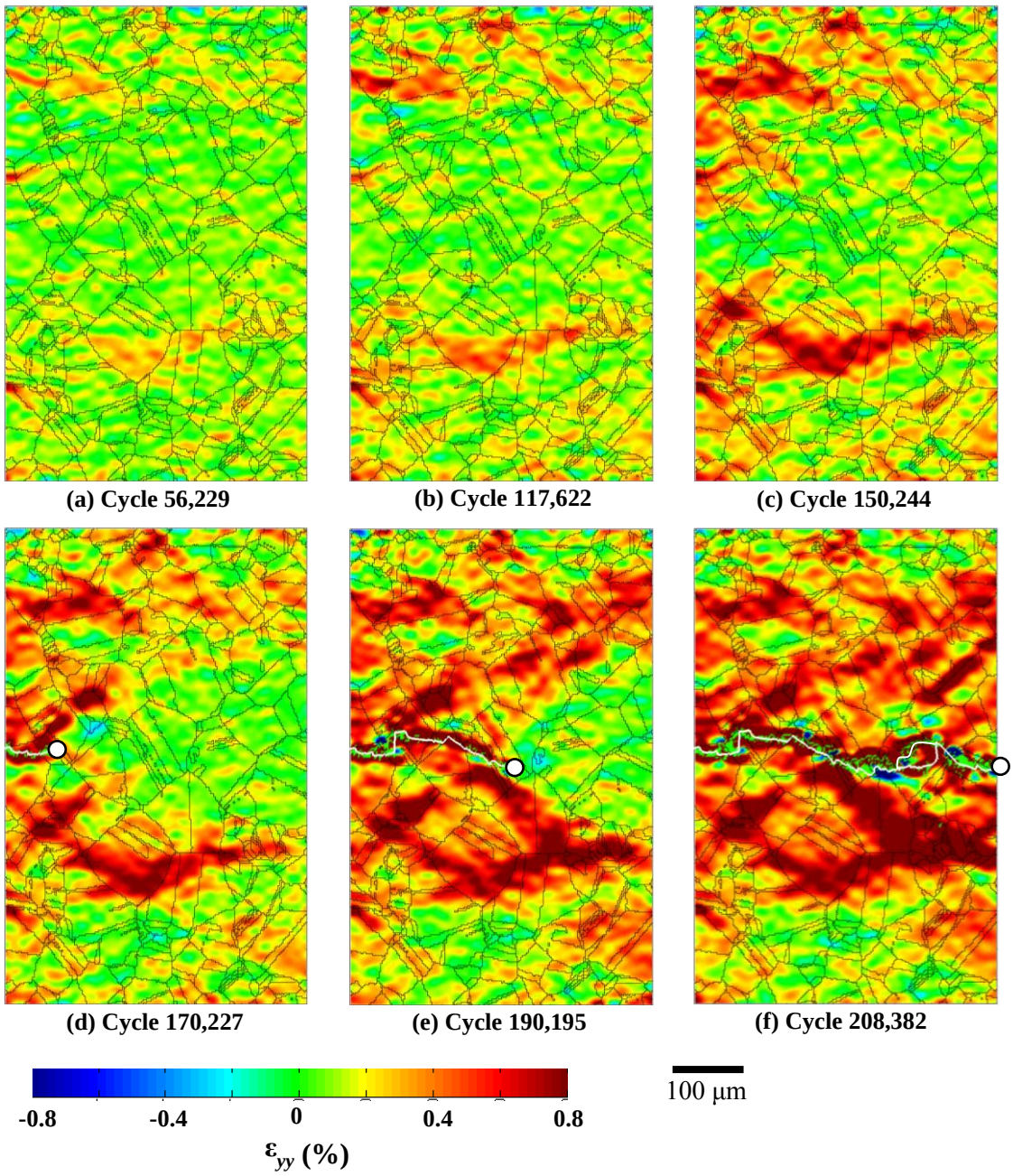

Fig. 6.11. Evolution of *in situ* ε_{yy} strain field throughout region 2. (a) Crack tip is 750 µm from entering region. (b) Crack tip is 290 µm from entering region. (c) Crack tip is 80 µm from entering region. (d-f) Crack tip is indicated by white dot. Cycle numbers are indicated below each strain field.

In Fig. 6.10a, the strain field indicates that several strain localizations have developed in region 1 – primarily starting at grain boundaries but also appearing as slip inside grains along specific slip systems – before the crack even enters the region. At cycle 56,229, the crack length was 1.66 mm (still 180 µm entering region 1). Even more interesting is that in region 2, which

was 750 μm ahead of the crack tip at cycle 56,229, measurable strain localizations are visible by this time (Fig. 6.11a) primarily in the form of slip bands in a significant number of grains. The evolution of strain fields in Figs. 6.10 and 6.11 show that many areas start accumulating strain long before the crack reaches the region of interest (*i.e.*, ahead of the high strain lobes at the crack tip). As the crack tip approaches each region, other strain localizations form, but the earliest slip band localizations intensify and most become the sites where some of the highest strains in the region are observed. This sequence of events is apparent in both Fig. 6.10 and Fig. 6.11.

In situ strain fields also show that plastic strain accumulation occurs when the two lobes emanating from the crack tip reach the point of interest. The material directly ahead of the crack tip is relatively unstrained until the crack tip passes through it. A good example of this is in Fig. 6.11(d-f).

Crack tip locations (the same ones displayed in Figs. 6.10 and 6.11) were identified in the deformed *in situ* images as demonstrated in Fig. 6.12 on strips of four images within region 1. These locations were then transformed to the reference image and the crack length at each image was calculated.

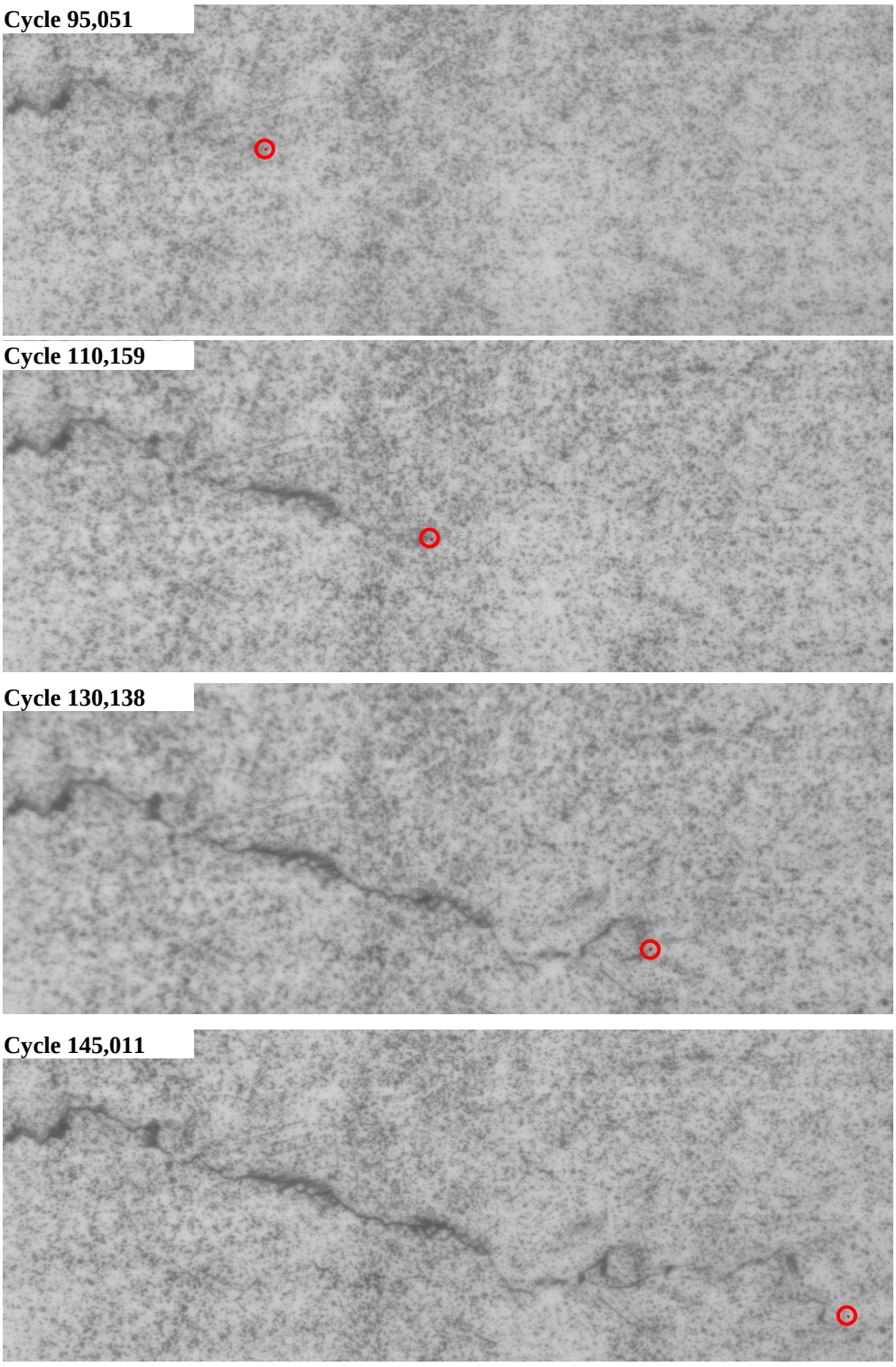

Fig. 6.12. *In situ* pictures of crack growth through region 1. Crack tips were identified in *in situ* images for measuring fatigue crack growth rates.

Based on the crack tip information from *in situ* images, the crack length was plotted against cycle number for both regions in Fig. 6.13. In region 1 (Fig. 6.13a), the plot of crack length vs. cycle number is color-coded so that the color of the a vs. N plot matches the color of the grain at that cycle number (seen on the right of the plot). In region 1 (Fig. 6.13a) the plot is nearly linear with a relatively constant crack growth rate (constant slope) of 6.7 nm/cycle (in agreement with Jablonski, 1978). The stress intensity range was held constant while the crack tip was within region 1; consequently, the Paris relationship also predicts a constant crack growth rate. The deviations from linearity in Fig. 6.13a are primarily due to microstructural effects, but there is some amount of crack tip identification error present as well. As the crack grows through the microstructure, the crack growth rate is expected to vary due to changes in crack direction and varying resistance of the microstructure to crack growth with location. Although the *in situ* images are capable of grain level observation, the crack tips within these images cannot be identified with enough accuracy to make conclusions about crack growth rates at the grain level. The images in Fig. 6.12 are an example of the appearance of the crack line in the *in situ* microscope images.

As the crack grew through region 2, the load range was held constant so that the stress intensity factor range increased with crack length. Consequently, the crack growth rate throughout region 2 increases slightly with crack length. This is indicated in Fig. 6.13b by the lower slope at shorter crack lengths (and cycle numbers) and higher slope at longer crack lengths. A linear fir to the curve in Fig. 6.13b gives a crack growth rate of 7.7 nm/cycle, but this is only an average value since the crack growth rate is nonlinear throughout region 2. As in region 1, there appear to be some local variations in crack growth rate that could be related to the microstructure, but some of this variation is caused by crack tip misidentification. The

relationship between crack growth rates and surface microstructure could be measured with much higher confidence by testing a polished specimen without a speckle pattern on the surface.

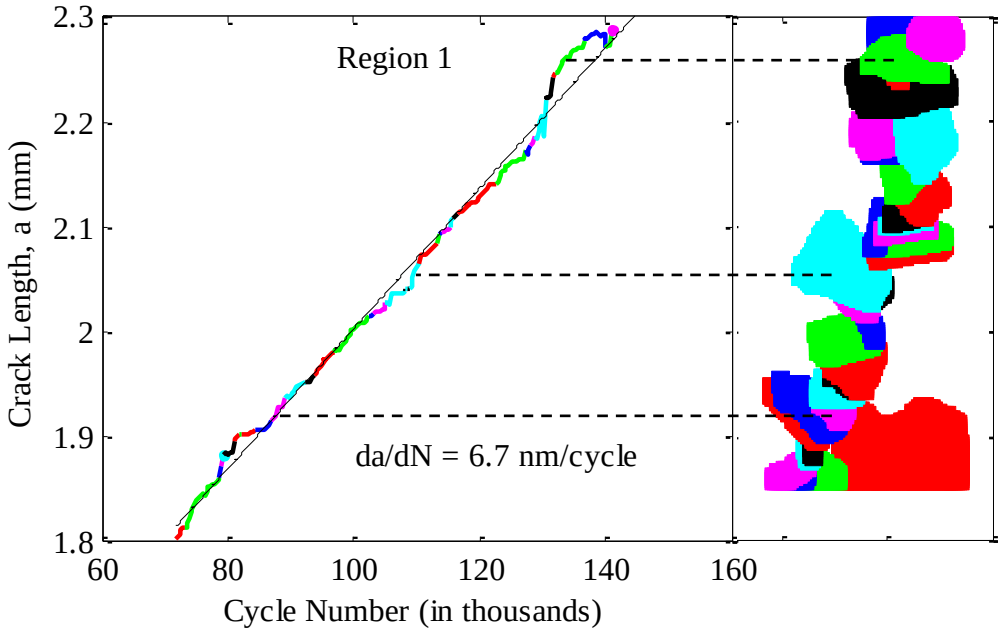

(a)

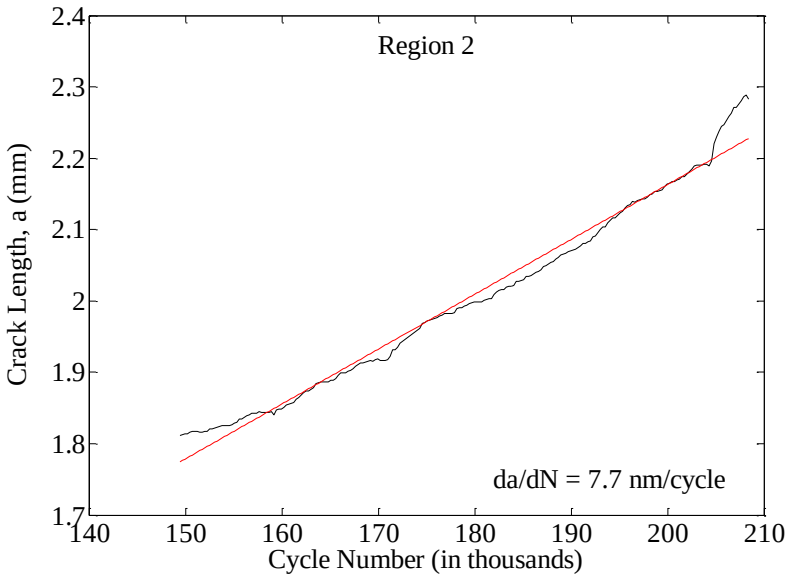

(b)

Fig. 6.13. Crack length vs. cycle number for (a) region 1 (b) region 2. Average crack growth rates are indicated in the lower right corner of each plot.

6.4 Postmortem Analysis

After the second set of *ex situ* images, the speckle pattern was cleaned off and the specimen was placed into the scanning electron microscope (for a second time). Backscatter electron (BSE) imaging was used to obtain images of the crack path in relation to the microstructure for both regions of interest, the results of which are shown in Figs. 6.14(a,b). Crack growth is predominantly transgranular like the crack growth observed in the experiments of chapter 5. The location of the crack line and slip bands in relation to the grain boundaries also confirms the accuracy of the spatial alignment between DIC fields and EBSD data shown in the earlier results of this chapter.

Portions of Figs. 6.14(a,b) are magnified in Figs. 6.14(c,d) respectively for a more detailed view of some parts of the crack path and associated slip bands within the selected areas. In Fig. 6.14d, the slip bands at point 1 change direction at twin boundaries confirming the DIC results in Fig. 6.6; however, the DIC results have the added advantage of giving quantitative values of strain at these locations. The strain within the slip bands at point 1 was plotted in Fig. 6.9 and strain was seen to vary significantly inside and outside the slip bands (with measured ε_{yy} strains up to 1.8% in some cases). While the plot in Fig. 6.9 appears to show a sinusoidal variation in strain with distance, the micrograph in Fig. 6.14d shows highly concentrated slip bands perhaps 1 μm in width with relatively large gaps (9-13 μm) between them. The width of the strain peaks in Fig. 6.9 is approximately equal to the subset size (9 μm) because the slip bands are narrower than the subset size. Because measured strains within these slip bands are averaged over the width of the subset size, the true peak strains within these slip bands (and consequently strain gradients) are higher than indicated in Fig. 6.9.

At point 2 in Fig. 6.14d, another grain shows slip occurring in two active slip systems. While most of the information about slip systems in Fig. 6.14 is also captured by DIC, one piece of important information in which these BSE images are more accurate is in crack path identification.

The crack path in Figs. 6.14(c,d) appears to be rather rough on the microstructural scale. The crack branches several times as it grows through these regions (points 3). The branches that become part of the primary crack path are the most energetically favorable ones. Whether a branch of the crack will continue growing depends on both the crack driving force and the material resistance. If the crack deviates from a straight line, it is the crack driving force that changes the crack direction so that the crack grows straight on the macroscopic scale. At the grain level, material resistance is inhomogeneous and anisotropic. For Hastelloy X, cracks appear to grow by following slip systems; therefore, material resistance is dominated by the orientation of slip systems. An example of this is at point 3 in Fig. 6.14d where the crack appears to grow at a downward angle along a slip band and then jump forward to the next slip band.

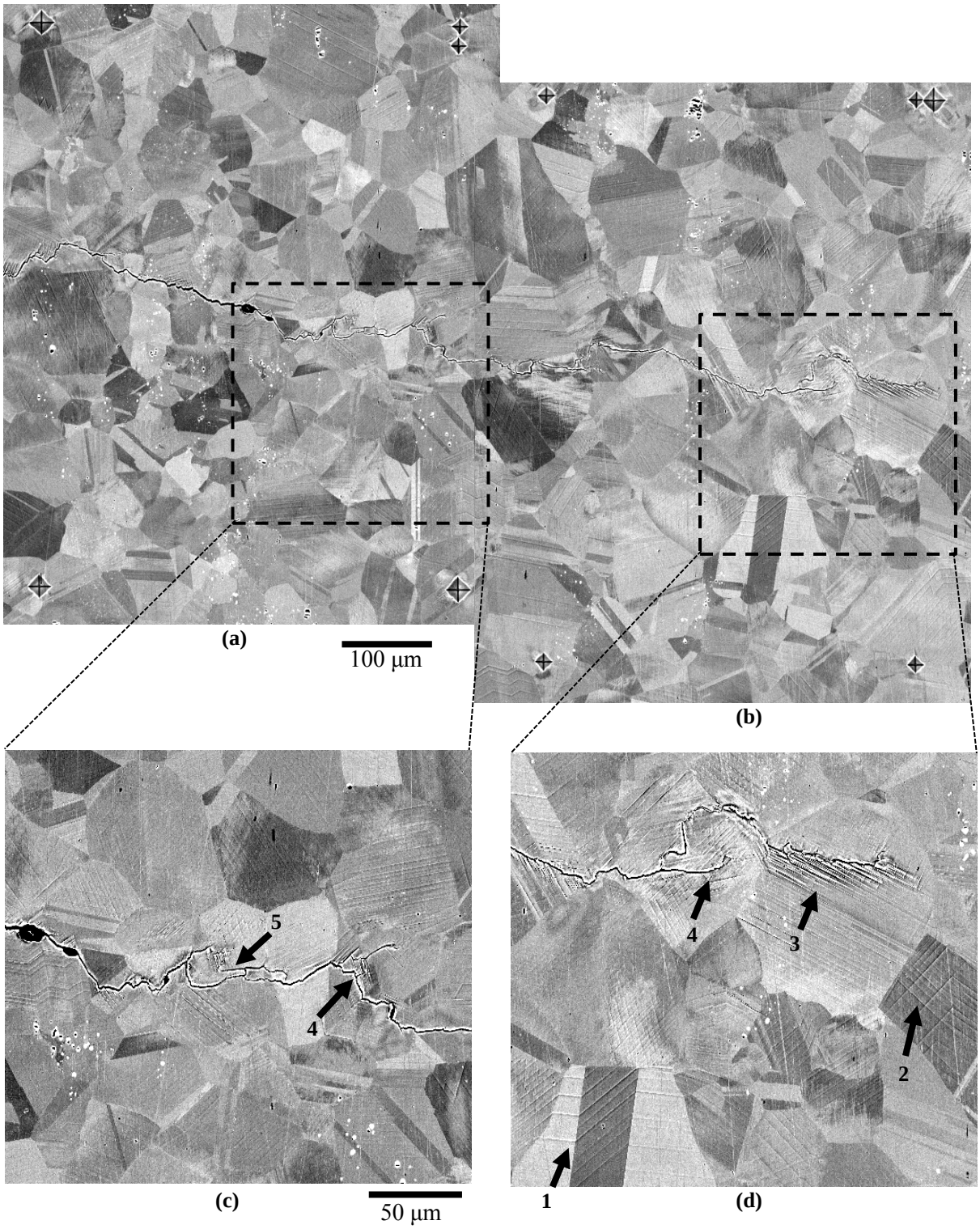

Fig. 6.14. Backscatter electron image showing the crack path through both regions of interest in relation to microstructure. (a) Region 1, (b) region 2, (c) magnified portion of region 1, (d) magnified portion of region 2.

Since slip systems are rarely parallel to the initial notch line, they tend to cause the crack to deviate from the straight path sought by the driving force. In this experiment, the crack is relatively long compared to the microstructure, but is still clearly under the influence of grain orientation at its tip. The crack grows relatively straight macroscopically, but at the grain level, there are deviations of up to 150 μm (see Fig. 6.1 where the crack has just entered region 1), which amounts to a few grain diameters.

Crack branches that do not become part of the primary crack path are the result of a crack growth direction that is only energetically favorable for a short period of time. An example of this is in Fig. 6.14c where the crack appears to branch and grow both downward and upward at point 4. The downward path may seem less energetically favorable at first because it is at a steeper angle, but the lower path soon crosses a twin boundary where a slip plane is oriented at a much shallower (and more energetically favorable) angle. The primary crack then continues along this path thereby reducing the stress (driving force) at the tip of the other branch. The *in situ* images showed one point where the crack branched and one of the branches actually grew backwards to form the closed loop at point 5 in Fig. 6.14c. Growing backwards is generally not energetically favorable; however, in this case it is suspected that sub-surface effects are at play. This experiment was only observed with surface measurements, but fatigue cracks are, by definition, three-dimensional. The backward crack growth at point 5 probably took place because the crack had grown forward in a similar trajectory in the grains just below the surface. The crack on the surface grew backward to meet up with this interior portion of the crack because it was more energetically favorable than the existing crack growing toward the interior of the specimen.

In fact, the crack front is typically curved in these specimens with the longest crack lengths near the center of the interior of the specimen. After capturing the BSE images, the sample was completely fractured by monotonic loading in the load frame. The resulting fracture surface is shown in Fig. 6.15 with the fracture surfaces corresponding to the notch on the left, the fatigue crack in the center, and the plastic monotonic overload region on the right. The final fatigue loading crack front is indicated by the dashed line where the fatigue crack surface meets the plastic overload fracture surface. Measurements made from this image show that the crack front was curved so that the crack length was slightly longer at the interior than the surfaces. The interior fatigue crack length was 2.9 mm at the end of the test. On the imaging surface, it was 2.8 mm (in agreement with *ex situ* DIC images) and on the back surface, it was 2.6 mm. Compared to other specimens subjected to similar loading, this crack front is typical. It is relatively symmetric with only a 200 μm difference in crack length between the front and back faces. The amount of curvature is also typical with about 200 μm of difference between the average surface crack length and the maximum interior length. Because this is a large grain material, the crack path was relatively jagged (see Fig. 6.14). This leads to the rather rough appearance of the fatigue crack surface in Fig. 6.15. However, at the macroscale, the crack surface is flat with the height of the crack at the specimen surface at approximately the same height as the crack surface at the interior of the specimen (*i.e.*, there is no slant in the crack from the interior to the specimen surface).

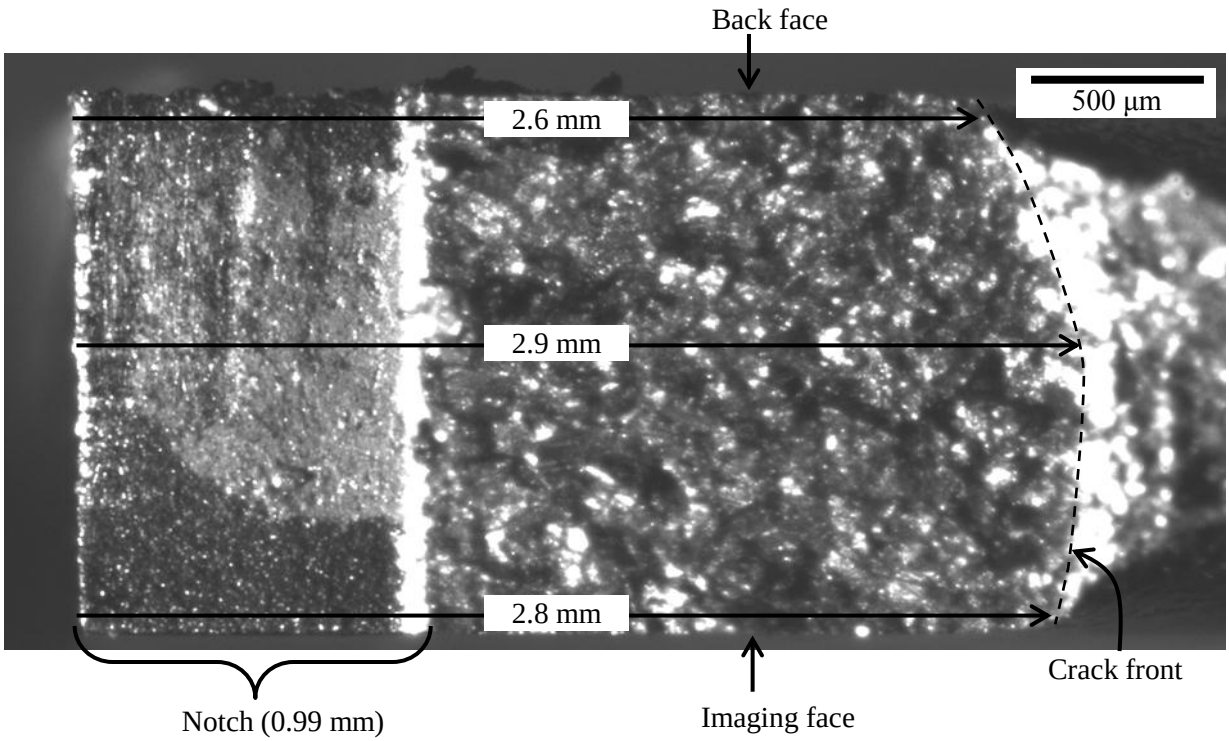

Fig. 6.15. Fracture surface of the specimen (bottom half). The notch is on the left and the fatigue crack runs from the right end of the notch to the "crack front" line.

While the cracks discussed in this thesis are all long enough to be characterized as macroscale cracks, microscale and mesoscale effects still clearly affect the local crack path. Micrographs of the three cracked Hastelloy X specimens discussed in this thesis are shown in Fig. 6.16. For easier comparison among specimens, the micrographs were rotated so that the cracks are vertical with the notch tips at the bottom. The specimens discussed in chapters 4, 5, and 6 are shown in Fig. 6.16(a,b,c), respectively with outlines of the regions of interest investigated in each of those experiments. All three cracks are macroscopically straight – the most variation is in Fig. 6.16c near the first set of indentation marks where the crack deviates by 150 μm corresponding to the distance of a few grain diameters. However, as was shown in chapters 4 through 6, there are locations where branching or turning of the crack path can be related to microstructure.

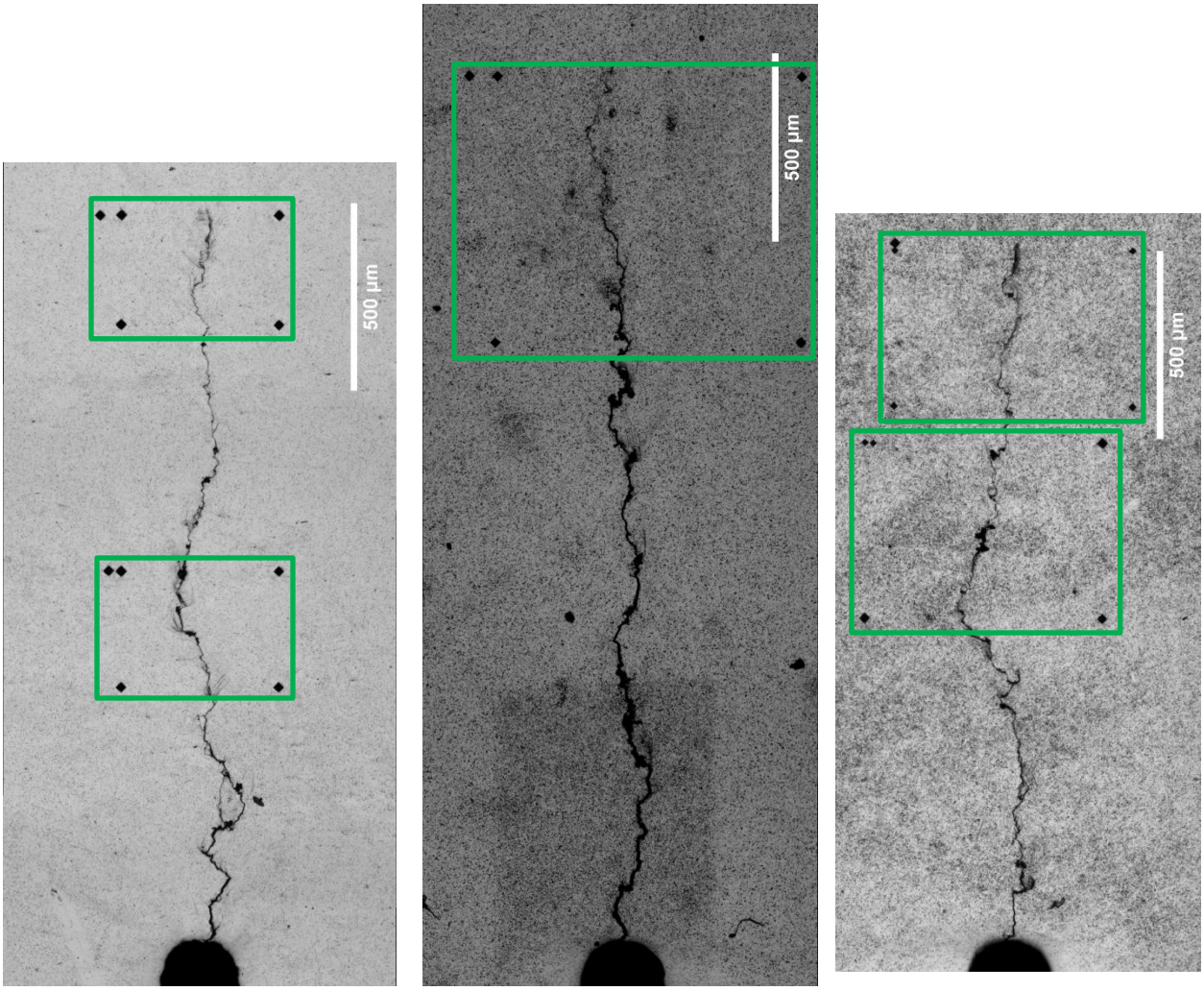

(a) **(b)** **(c)**

Fig. 6.16. Crack paths for the three Hastelloy X specimens shown in chapters 4 through 6 (rotated images taken at 5x magnification in the optical microscope). Regions of interest for each specimen are outlined. (a) Chapter 4: specimen that was observed at 2x and 14x magnification simultaneously. (b) Chapter 5 specimen examined with *ex situ* technique. (c) Chapter 6 specimen observed with combined *in situ* and *ex situ* technique. All three crack paths are relatively straight, deviating from straight by less than the notch width. The most extreme deviation in (c) is around 150 µm, which is only a few grain diameters' distance.

6.5 Summary

In this chapter, many different data sets from various measurement techniques were aligned to investigate fatigue crack growth strains with an unprecedented level of detail. Low magnification *ex situ* DIC provided a macroscopic view of the strains in the vicinity of the fatigue crack. High resolution e*x situ* DIC provided grain level measurements of strain fields in the wake of a fatigue crack. This allowed the identification of strain localizations at grain

boundaries and in slip bands within grains. *In situ* DIC with an optical microscope provided grain level measurements of the strain fields and how they developed as the crack grew through the specimen in addition to crack growth rates. All of these measurements were linked to microstructure through alignment with EBSD measurements, which provided grain geometry and orientation. After fatigue loading, BSE measurements gave visual confirmation of the slip bands seen in the DIC measurements and a clearer picture of the crack path in relation to the microstructure. Finally, images of the fracture surface gave limited but useful glimpse of fracture within the interior of the specimen.

Strain localizations within the wake of the fatigue crack has a complex dependency on several factors including position with relation to the crack line, crack direction, grain geometry and orientation, and sub-surface grains. Crack growth was in a transgranular fashion, most frequently following slip bands. Microstructural effects on crack growth were evident in the form of crack branching and frequent changes of crack direction. Ultimately, the crack path depends on a number of factors including the local stress field, the global crack driving force, and local microstructural inhomogeneities.

In situ results showed that some plastic strains accumulate ahead of the strain lobes, but most strain localization occurs when the strain lobes pass through the material. In the area directly ahead of the crack tip, between the strain lobes, there is relatively little strain until the crack tip passes.

Chapter 7: Conclusions and Suggested Future Work

This work provided a multiscale investigation into fatigue crack growth including aspects of crack closure, fatigue strain accumulation, crack path, and their relation to microstructure. The conclusions and future work presented here are divided into three sections, all of which have a strong emphasis in multiscale understanding of the fatigue crack growth phenomenon. The first is related to crack closure studied at multiple length scales (chapter 3). The second section presents conclusions from the grain level DIC measurements of fatigue crack growth and their relation to microstructure (chapters 4, 5, and 6). The third section provides suggestions for future work in this field.

7.1 Crack Closure

In chapter 3, three techniques for measuring fatigue crack closure (and opening) levels at different length scales were introduced. At the microscale, the first technique used two-point DIC virtual extensometers to measure local crack opening levels at several points along the crack line. Local crack opening levels were found to increase as the crack tip was approached, which is consistent with other studies (Macha *et al.*, 1979; Riddell *et al.*, 1999). For the low and medium K experiments (ΔK = 15.4 and 18.9 MPa$\sqrt{m}$, respectively), local crack opening levels near the crack tip were 34% and 35% respectively, in agreement with published values (27-42%, Takao *et al.*, 1985). In the high K experiment (ΔK = 18.9 MPa$\sqrt{m}$), crack tip opening level was around 21%, somewhat lower than the other experiments due to the short crack effect.

Two macroscale crack closure measurement techniques were also introduced. Both used the least squares regression method (discussed in detail in chapter 2) to extract stress intensity factors from DIC-measured macroscale displacement fields. The first full-field technique, called the full-field effective *K* method, measured crack closure levels as the difference between the measured value of stress intensity factor and the value predicted by linear elastic theory. The results of this method agreed well with local crack closure measurements far from the crack tip (beyond 400 μm). The second full-field technique, the *K*-compliance method, used *K* as a measure of displacement and crack closure levels were designated as the load at which a compliance change in the *K* vs. load curve occurred. Crack closure measurements from this method are slightly lower than local measurements at the crack tip (and higher than the full-field effective *K* method). Both macroscale methods use the entire field of view as a global displacement gage, and consequently give crack closure values below the local crack tip closure values from microscale measurements.

Although the crack closure study performed here used DIC measurements of higher resolution than had previously been accomplished, allowing the described multiscale measurements, the issue of crack closure remains a significant challenge particularly in terms of modeling. The physical origins of crack closure are well understood. However, the use of a single crack closure/opening load as an adjustment in a Paris relationship to describe what is clearly a 3D multiscale process with many underlying causes is not very satisfactory. In the future, it would be beneficial to develop multiscale models, likely based on experiments such as these that specifically consider multiscale effects.

One potential use for the crack closure measurement techniques shown in this thesis is the determination of crack closure values at elevated temperatures at which other measurement

techniques have difficulty. This work was funded by the Midwest Structural Sciences Center (MSSC). The MSSC is a collaborative effort between the Air Force Research Laboratory and the University of Illinois to develop tools for structural design of aircraft operating in extreme environments. As one of the goals of the MSSC is to study thermoacoustic fatigue, it would be of interest to study thermal effects on crack closure. This work is currently being undertaken by another MSSC collaborator, Mallory Casperson. She has already applied these techniques to measure crack closure at temperatures up to 400 °C and to investigate thermal overload effects.

7.2 Influence of Microstructure on Fatigue Crack Growth

While the work described in chapters 2 and 3 focused on deformation *within a fatigue cycle*, the work in chapters 4 through 6 studied fatigue strain accumulation *over a number of fatigue cycles* and compared those strain fields to the microstructure. In chapter 4, accumulated plastic strain fields in titanium were quantified using DIC and compared to grain boundaries revealed by etching. While this technique provided a good method for relating strains to microstructural geometry, the EBSD method presented in chapters 5 and 6 showed grain boundary geometry with higher precision and additionally provided grain orientation information.

Measurements of accumulated fatigue crack growth strains made at multiple length scales were discussed in chapter 4. *In situ* strain fields at 14x (0.322 μm/pix) and 2x (2.12μm/pix) optical magnifications and were measured *simultaneously* on the front and back sides of the specimen. *Ex situ* strain fields on the same specimen at 5x (0.87 μm/pix) and 20x (0.22 μm/pix) magnification (both on the front side) revealed strain concentrations in lobes inclined at angles between ±(30° to 60°) to the crack line. An asymmetry of the strain field about the crack line was also seen with a relatively large (several hundred square microns) unstrained region below the

crack line. Higher magnification DIC measurements were shown to have finer resolution than low magnification measurements with subset size being the dominant, but not the only, factor determining spatial resolution. To achieve reliable sub-grain level measurements, the subset size (linear dimension) must be smaller than roughly one-fourth of the grain diameter. Other factors such as subset spacing, speckle pattern quality, and number of pixels per subset were also found to have an effect on the spatial resolution of DIC measurements.

The novel *ex situ* technique introduced in chapter 4 was described in detail in chapter 5 for obtaining high resolution strain fields and relating them to microstructure. Using an optical microscope, image arrays of a region of interest were captured *ex situ* and the DIC strain fields from each correlation were stitched together to form a strain field over the entire region of interest. Vickers indentation marks were then used to overlay strain fields with EBSD measurements of microstructure.

This *ex situ* technique was used to investigate accumulated strain fields in fatigue crack growth. The specimen was removed from the load frame for imaging at intervals of crack growth giving strain fields for 5 different crack tip positions (B–F). Low magnification 5x results (0.87 μm/pix) (Fig. 5.4) showed that the height of plastically deformed material in the crack tip wake was in excess of 970 mm. The measurements of the residual strain field at 5x magnification again showed lobes of high strain on alternating sides of the crack line. The details of these lobes were further examined using 50x(0.087 μm/pix) *ex situ* DIC measurements at each crack length to reveal strain localizations on grain and twin boundaries and along slip bands within grains, thought to act as predecessors to widespread fatigue damage accumulation. A plot of the crack path on the microstructure map revealed several locations where the crack path abruptly changed direction within the interior of grains. This was attributed to the competition between local

microstructural barriers versus the global crack driving force (although subsurface microstructural effects cannot be ruled out).

The average octahedral shear strain within four selected grains was tracked and found to increase when a strain lobe emanating from the crack tip reached each grain location. With further crack growth, the strain in these grains plateaued as the lobes moved ahead of the grains. In one case, the accumulated strain in a particularly intense strain lobe (formed at time E) was found to decrease after further crack growth indicating *reverse plasticity* near or slightly behind the crack tip. This was in agreement with observations of full-field plots of incremental strain accumulation.

To acquire DIC measurements more frequently, instead of intermittently removing the specimen from the load frame for multiple *ex situ* measurements, an *in situ* microscope was mounted near the load frame to supplement *ex situ* measurements, as described in chapter 6. *Ex situ* DIC strain fields measured at 50x still provided excellent sub-grain level spatial resolution, while the excellent temporal resolution of the 10x (0.44 μm/pix) *in situ* DIC measurements provided details of when and how specific strain localizations developed. The combination of *in situ* and *ex situ* DIC strain fields linked with grain orientation and geometry measurements from EBSD, along with micrographs from both optical and electron microscopy, provided a study of fatigue crack growth with an unprecedented level of information.

The *in situ* measurements revealed that many of the strain localizations developed in the regions of interest had originated long before the crack tip approached the regions. As the crack grew through the region, these localizations intensified. Plastic strain moved through the region within lobes emanating from the crack tip at angles of ±(30° to 60°) leaving a wake of plastically deformed material behind them. In areas directly ahead of the crack tip, the material remained

relatively unstrained until the crack passed through it. Crack growth rates were found to be consistent with the Paris relationship. Some local variations were observed that were most likely due to microstructural effects, but there is some uncertainty in these measurements since the speckle pattern, necessary for these experiments, hindered crack tip identification.

Strain localizations were found to have a complex dependency on location, crack path, and microstructure. DIC measurements revealed many strain localizations on grain and twin boundaries that were not apparent from micrographs of the specimen. However, micrographs did confirm the existence of slip bands within several grains that were detected by DIC measurements. *Ex situ* DIC measurements at 50x magnification showed that ε_{yy} strains within some slip bands, were 1.8 % with strains of 0.0 % within the material between slip bands. This resulted in steep strain gradients up to 0.4 % strain per μm. These calculations imply a measurement resolution of 4.5 μm or about half of the subset size, as is consistent with the spatial resolution being limited by subset size. Additionally, some slip bands were detected in the high resolution DIC results that were not visible in the postmortem backscatter electron images (at the magnifications used here).

Postmortem micrographs also provided enhanced detail of the slip bands and the crack path. In agreement with other studies of nickel alloys, the crack was most frequently found to grow in a transgranular fashion along slip planes. The global crack driving force provides motivation for the crack to grow straight, but local inhomogeneities in the microstructure cause deviations in the crack path up to 150 μm—a couple of grain diameters' distance. This competition between global driving force and microstructural inhomogeneities also caused several instances of crack branching and abrupt changes of direction.

7.3 Future Work

Although these experiments produced an unprecedented amount of data, both in terms of extent and resolution, it is inevitable that data have limitations. There are a few aspects of these experiments that could benefit from further optimization. Strain fields with even higher resolution than the *ex situ* 50x results shown in this work could be obtained by further optimizing the speckle pattern allowing for smaller subset sizes by a factor of 2 or more (by the length dimension). Better resolution for *in situ* measurements could be obtained by improving lighting, increasing magnification, and reducing system noise (*e.g.,* vibration). *In situ* measurements also have the potential for simultaneously measuring strain fields *within* cycles and *between* cycles if the images can be kept in focus throughout the loading cycle. Commercially available systems that integrate load frames with microscopes could be helpful in this regard.

Several insights were gained from the experiments described in this thesis, but measurements such as these could also be analyzed on a statistical basis to infer the effects of microstructure on strain localizations. A multivariate regression could be used to extract correlations between local strain values and microstructural properties. Because of the non-uniform nature of the strain field around a crack tip, any such regression would also need to include the location of each point in relation to the crack tip and possibly some information about crack path variation. A statistical correlation would provide a quantitative measure of the effects of microstructural variables such as grain orientation (perhaps based on the global or local Schmid factor), grain geometry (large vs. small grains), and grain boundary misorientation among others. Padilla *et al.* (2011) used a Spearman rank correlation to compare strain fields to microstructural properties. They found a correlation between Schmid factor and maximum shear strain in uniaxial tension experiments in Zirconium. A statistical analysis of the transmission of persistent slip bands was performed by Sangid *et al.*, 2011 by performing molecular dynamics

simulations over a large number of grains. They found that twin boundaries are stronger barriers to slip transmission between grains than other coincidental site lattice grain boundaries.

An alternative approach to a statistical analysis was taken by Abuzaid *et al.* (2011). Uniaxial tension experiments were performed on Hastelloy X using the *ex situ* technique described in this thesis. They examined specific grain boundaries and observed that more strain transmission across boundaries occurred when the boundaries had a low residual burgers vector while boundaries with high residual burgers vectors blocked transmission (in agreement with predictions from theory). As with the crack closure work, the MSSC would like to extend this work to high temperature applications. Wael Abuzaid, another MSSC collaborator, has done some work in this area.

Both strain and microstructure measurements in these experiments are two-dimensional and take place only on the specimen surface. However, one factor that potentially influences the crack path and surface deformation is microstructural effects below the surface. Thus, one extension of this work that would overcome this limitation is the acquisition of 3D measurements, both in regards to microstructure characterization and displacement/stain. Microstructural characterization could be partially improved by obtaining sub-surface measurements of microstructure (after crack growth) through serial sectioning as, for example, in the work of Groeber *et al.,* 2008, and Field *et al.,* 2010. A more thorough approach is the use of diffraction contrast tomography (Herbig *et al.,* 2011), which can be used non-destructively to measure both microstructure and crack path three dimensionally.

Improvements in the measurement of material deformation can be obtained by using the stereovision DIC technique (Luo *et. al.*, 1998) which uses two cameras to measure out-of-plane deformation; however, this technique is still limited to surface measurements. An even more

powerful technique for measuring material deformation is digital volume correlation (DVC) which uses tomography to measure three-dimensional displacements throughout the entire specimen (Bay *et al.*, 1999, Gates *et al.*, 2011). The technique has a few drawbacks: it is currently limited to relatively small data sets (due to computational speed and memory), there are difficulties in generating a three dimensional speckle pattern, and acquisition of each tomography scan is slow. However, it may be possible to obtain very high resolution *ex situ* 3D DVC measurements, of fatigue damage accumulation analogous to those presented in this work.

Another piece of data that would improve understanding of these experiments is the stress field. Although the global stress is known, microstructure and crack path geometry alter these fields locally. It is rare for experimental techniques to capture both stress and strain. Some estimation of stress values could possibly be obtained through simulations such as crystal plasticity models. Multiple studies on these models have shown them to be qualitatively accurate in some situations, but their reliability still has room for improvement. The fidelity of these models could be improved if they were given three dimensional microstructure measurements of the sample to be experimentally tested. Simulation strain fields on the specimen surface could then be compared to experimental measurements to validate the model and improve the credibility of simulated stress fields.

While this work shed light on the fatigue crack growth process, strain localizations and crack path have a complicated dependency on microstructure. Some of the suggestions above for future work could provide further insight. However, even with the experimental techniques developed here, an extensive testing program and/or multivariate analysis could further elucidate this dependency. This work developed several techniques for linking grain level strains in fatigue

crack growth to microstructure and used those techniques to show how localizations in these strain fields are affected by crack path, grain geometry, and grain orientation.

References

Abanto-Bueno J. Lambros J. Experimental determination of cohesive failure properties of a photodegradable copolymer. Experimental Mechanics, v. 45, n. 2, pp. 144-152 (2005).

Abanto-Bueno J., Lambros J., An experimental study of mixed mode crack initiation and growth in functionally graded materials. Experimental Mechanics, v. 46, n. 2, pp. 179-196 (2006a).

Abanto-Bueno J., Lambros J., Parameters controlling fracture resistance in functionally graded materials under mode I loading. International Journal of Solids and Structures v. 43 n. 13, pp. 3920-3939 (2006b).

Abuzaid W., Carroll J., Sehitoglu H., Lambros J., Global Analysis of Slip Transmission Across Grain Boundaries in a Polycrystalline Nickel Based Super Alloy (in progress) (2011).

Adams NJI, Fatigue crack closure at positive stress, Engineering Fracture Mechanics, v. 4, pp. 543-554 (1972).

Allison JE. Ku RC. Pompetzki MA. A comparison of measurement methods and numerical procedures for the experimental characterization of fatigue crack closure. ASTM – STP 982, pp. 171-185 (1988).

Anderson, T.L., Fracture Mechanics, Fundamentals and Applications, 2nd ed., pp. 162, (1995).

ASTM Standard E399, Standard test method for linear-elastic plane-strain fracture toughness KIC of metallic materials, ASTM International, West Conshohocken, PA (2006).

ASTM Standard E647-05 Standard test method for measurement of fatigue crack growth rates. ASTM International, West Conshohocken, PA (2005).

Bartali A. E., Aubin V., Degallaix S., Surface observation and measurement techniques to study the fatigue damage micromechanisms in a duplex stainless steel, International Journal of Fatigue, v. 31, p. 2049 (2009).

Bay BK., Smith TS., Fyhrie DP., Saad M., Digital volume correlation: three-dimensional mapping using X-ray tomography, Experimental Mechanics, v. 39, n. 3, pp. 217-226, (1999).

Budiansky B., Hutchinson JW., Analysis of closure in fatigue crack growth, Journal of Applied Mechanics, v. 45, pp. 267-276 (1978).

Callister W.D. Jr., Materials Science and Engineering an Introduction, 5th ed., John Wiley & Sons Inc., New York (1999).

Carroll J. Abuzaid W. Lambros J. Sehitoglu H., An experimental methodology to relate local strain to microstructural texture. Review of Scientific Instruments, v. 81, article 083703 (2010).

Carroll J. Efstathiou C. Lambros J. Sehitoglu H. Hauber B. Spottswood S. Chona R., Investigation of fatigue crack closure using multiscale image correlation experiments. Engineering Fracture Mechanics, v. 76, pp. 2384-2398 (2009).

Clayton JD., Schroeter BM., McDowell DL., Graham S., Distributions of stretch and rotation in polycrystalline OFHC Cu. Journal of Engineering and Materials Technology, v. 124, p. 302 (2002).

Davidson DL., A model for fatigue crack advance based on crack tip metallurgical and mechanics parameters, Acta Metallurgica, v. 32, n. 5, pp. 707-714 (1984).

Davidson DL., Tryon RG., Oja M., Matthews R., Ravi Chandran KS., Fatigue crack initiation in waspaloy at 20°C. Metallurgical and Materials Transactions A, v. 38A, pp. 2214-2225 (2007).

Delaire F., Raphanel J. L., Rey C., Plastic heterogeneities of a copper multicrystal deformed in uniaxial tension: experimental study and finite element simulations. Acta Materialia, v. 48, p. 1075 (2000).

Donald K. Paris PC. An evaluation of ΔK_{eff} estimation procedures on 6061-T6 and 2024-T3 aluminum alloys. International Journal of Fatigue, v. 21, pp. S47-S57 (1999).

Dodds R.H., Anderson T.L., Kirk M.T., A framework to correlate a/W ratio effects on elastic-plastic fracture toughness (J_c). International Journal of Fracture, v. 48, pp. 1-22 (1991).

Efstathiou C., Experimental Characterization of Heterogeneous Deformation due to Phase Transformations, Twinning, and Slip Deformation Using Digital Image Correlation. Ph.D. Thesis, University of Illinois at Urbana-Champaign (2008).

Efstathiou C., Sehitoglu H., Lambros J., Multiscale strain measurements of plastically deforming polycrystalline titanium: Role of deformation heterogeneities. International Journal of Plasticity, v. 26, pp. 93-106 (2010).

Eftis J., Subramonian N., Liebowitz H., Crack stress and displacement equations revisited. Engineering Fracture Mechanics, v. 9, pp. 189-210 (1977).

Elber W. Fatigue crack closure under cyclic tension. Engineering Fracture Mechanics, v. 2, pp. 37-45 (1970).

Elber W. The significance of fatigue crack closure. ASTM – STP 486, pp. 230-242 (1971).

Fagerholt E., Dørum C., Børvik T., Laukli HI., Hopperstad OS., Experimental and numerical investigation of fracture in a cast aluminum alloy. International Journal of Solids and Structures, v. 47, pp. 3352-3365 (2010).

Field DP., Magid KR., Mastorakos IN., Florando JN., Lassila DH., Morris JW. Jr., Mesoscale strain measurement in deformed crystals: A comparison of x-ray microdiffraction with electron backscatter diffraction. Philosophical Magazine, v. 90, p. 1451 (2010).

Fleck NA., Newman JC Jr., Analysis of crack closure under plane strain conditions. ASTM – STP 982, pp. 319-341 (1988).

Gates M., Lambros J., Heath MT., Towards high performance digital volume correlation, Experimental Mechanics (in press), DOI 10.1007/s11340-010-9445-0 (2011).

Groeber M., Ghosh S., Uchic MD., Dimiduk DM., A framework for automated analysis and simulation of 3D polycrystalline microstructures. Part 1: Statistical characterization. Acta Materialia, v. 56, pp. 1257-1273 (2008).

Héripré E., Dexet M., Crépin J., Gélébart L., Roos A., Bornert M., Caldemaison D., Coupling between experimental measurements and polycrystal finite element calculations for micromechanical study of metallic materials. International Journal of Plasticity, v. 23, p. 1512 (2007).

Herbig, M., King A., Reischig P., Proudhon H.,Lauridsen EM., Marrow J., Buffière JY., Ludwig W., 3-D growth of a short fatigue crack within a polycrystalline microstructure studied using combined diffraction and phase-contrast X-ray tomography. Acta Materialia, v. 59, pp. 590-601 (2011).

Irwin GR., Analysis of stresses and strains near the end of a crack traversing a plate. Journal of Applied Mechanics, v. 24 pp. 361-364 (1957).

Jablonski DA., Fatigue behavior of Hastelloy-X at elevated temperatures in air, vacuum and oxygen environments. Ph.D. Thesis, Massachusetts Institute of Technology (1978).

Jonnalagadda KN., Chasiotis I., Yagnamurthy S., Lambros J., Pulskamp J., Polcawich R., Dubey M., Experimental investigation of strain rate dependence of nanocrystalline Pt films. Experimental Mechanics, v. 50, p. 23 (2010a).

Jonnalagadda KN., Karanjgaokar N., Chasiotis I., Chee J., Peroulis D., Strain rate sensitivity of nanocrystalline Au films at room temperature. Acta Materialia, v. 58, pp. 4674-4684 (2010b).

Kmiec KJ., Determination of the Fracture Parameters Associated with Mixed Mode Displacement Fields and Applications of High Density Geometric Moiré. M.S. Thesis Texas A&M University (1994).

Laird C., Initial stages of damage in high stress fatigue in some pure metals. The Philosophical Magazine, v. 8, n. 95, pp. 1945-1963 (1963).

Lalor PL. Sehitoglu H. Fatigue crack closure outside a small-scale yielding regime. ASTM – STP 982, pp. 342-360 (1987).

Lambros J., Patel JK., Microscale digital image correlation study of irradiation induced ductile-to-brittle transition in polyethylene. Journal of Strain Analysis for Engineering Design, (in press) (2011).

Lankford J., Davidson DL., Fatigue crack micromechanisms in ingot and powder metallurgy 7xxx Aluminum alloys in air and vacuum. Acta Metallurgica, v. 31, n. 8, pp. 1273-1284 (1983).

Luo PF., Chao YJ., Sutton MA., Peters WH. III., Accurate measurement of three-dimensional deformations in deformable and rigid bodies using computer vision. Experimental Mechanics, v. 33, n.2, pp. 123-132 (1998).

Macha DE. Corbly DM. Jones JW. On the Variation of fatigue-crack-opening load with measurement location. Experimental Mechanics, v. 19, n. 6, pp. 207-213 (1979).

McEvily AJ. Boettner RC. On fatigue crack propagation in FCC metals. Acta Metallurgica, v. 11, pp. 725-743 (1963).

McNeill SR. Peters WH. Sutton MA. Estimation of stress intensity factor by digital image correlation. Engineering Fracture Mechanics, v. 28 n. 1 pp. 101-112 (1987).

Merzouki T., Collard C., Bourgeois N., Zineb TB., Meraghni F., Coupling between measured kinematic fields and multicrystal SMA finite element calculations. Mechanics of Materials, v. 42, p. 72 (2010).

Morris WL., James MR., Zurek AK., The extent of crack tip plasticity for short fatigue cracks. Scripta Metallurgica, v. 19, pp. 149-153 (1985).

Padilla H., Lambros J., Beaudoin A., Robertson I. M., Relating inhomogeneous deformation to local texture in zirconium through grain-scale digital image correlation strain mapping experiments. International Journal of Solids and Structures (in review) (2011).

Paris P. Erdogan F. A critical analysis of crack propagation laws. Basic Engineering Transactions ASME Series D, v. 85, pp. 528-534 (1963).

Paris PC. Tada H. Donald JK. Service load fatigue damage – a historical perspective. International Journal of Fatigue, v. 21, pp. S35-S46 (1999).

Paris PC. Lados D. Tada H. Reflections on identifying the real ΔK_{eff} in the threshold region and beyond. Engineering Fracture Mechanics, v. 75, pp. 299-305 (2008).

Peralta P., Dickerson R., Dellan N., Komandur K., Jameel MA., Effects of local grain orientation on fatigue crack growth in multicrystalline fcc metallic materials. Journal of Engineering Materials and Technology, v. 127, p. 23 (2005).

Peralta P., Choi SH., Gee J., Experimental quantification of the plastic blunting process for stage II fatigue crack growth in one-phase metallic materials. International Journal of Plasticity, v. 23, pp. 1763-1795 (2007).

Raabe D., Sachtleber M., Zhao Z., Roters F., Zaefferer S., Micromechanical and macromechanical effects in grain scale polycrystal plasticity experimentation and simulation. Acta Materialia, v. 49, p. 3433 (2001).

Randle V., Engler O., Introduction to Texture Analysis, CRC Press, Boca Raton FL. (2000).

Riddell WT. Piascik RS. Sutton MA. Zhao W. McNeill SR. Helm JD. Determining fatigue crack opening loads from near-crack-tip displacement measurements. ASTM – STP 1343, pp. 157-174 (1999).

Sachtleber M., Zhao Z., Raabe D., Experimental investigation of plastic grain interaction. Materials Science and Engineering A, v. 336, p. 81 (2002).

Saka M., Tanaka S. Strain and stress fields near the blunted tip of a crack under mixed mode loading and the implications for fracture. Mechanics of Materials, v. 5, pp. 331-338 (1986).

Sanford RJ., Dally J., A general method for determining mixed-mode stress intensity factors from isochromatic fringe patterns. Engineering Fracture Mechanics, v. 11, pp. 621-633 (1979).

Sangid MD., Maier HJ, Sehitoglu H., An energy-based microstructure model to account for fatigue scatter in polycrystals. Journal of the Mechanics and Physics of Solids, v. 59, pp. 595-609 (2011).

Schijve J. Fatigue crack closure: observations and technical significance. ASTM – STP 982, pp. 5-34 (1988).

Sehitoglu H. Characterization of crack closure. ASTM – STP 868, pp. 361-380 (1983).

Sehitoglu H. Crack opening and closure in fatigue. Engineering Fracture Mechanics, v. 21, n. 2, pp. 329-339 (1985).

Sehitoglu H. Sun W. Modeling of plane strain fatigue crack closure. Journal of Engineering Materials and Technology, v. 113, pp. 31-40 (1991).

Shih TT. Wei RP. A study of crack closure in fatigue. Engineering Fracture Mechanics, v. 6, pp. 19-32 (1974).

Suresh S. Ritchie RO. Near-threshold fatigue crack propagation: a perspective on the role of crack closure. In: Davidson D, Suresh S, editors. Fatigue Crack Growth Threshold Concepts. The Metallurgical Society of AIME, pp. 227-261 (1984).

Suresh S., Fatigue of Materials, 2nd ed., Cambridge University Press (1998).

Sutton MA. Wolters WJ. Peters WH. Ranson WF. Mcneil SR. Determination of displacements using an improved digital image correlation method. Image and Vision Computing, v. 1, n. 3, pp. 133-139 (1983).

Sutton MA. Zhao W. McNeill SR. Helm JD. Piascik RS. Riddell WT. Local crack closure measurements: development of a measurement system using computer vision and a far-field microscope. ASTM – STP 1343, pp. 145-156 (1999).

Sutton MA., Orteau J-J., Schreier HW., Image Correlation for Shape Motion and Deformation Measurements: Basic Concepts, Theory and Applications, Springer Media (2009).

Tada H. Paris PC. Irwin GR. The Stress Analysis of Cracks Handbook 2nd ed. St. Louis MO: Paris Productions Inc. (1985).

Takao K. Matsumoto K. Nisitani H. Fatigue crack closure in commercially pure titanium (measurement using DC-potential drop method). Nippon Kikai Gakkai Ronbunshu A Hen/Trans of Japan Society of Mechanical Engineers, v. 51(462), pp. 450-454 (1985).

Tatschl A., Kolednik O., A new tool for the experimental characterization of micro-plasticity. Materials Science and Engineering A, v. 339, p. 265 (2003).

Tong W., Detection of plastic deformation patterns in a binary aluminum alloy Experimental Mechanics, v. 37, p. 452 (1997).

Tschopp MA., Bartha BB., Porter WJ., Murray PT., Fairchild SB., Microstructure-dependent local strain behavior in polycrystals through *in-situ* scanning electron microscope tensile experiments. Metallurgical and Materials Transactions A, v. 40, p. 2363 (2009).

Walley J., Wheeler R., Uchic MD., Mills MJ., Local strain accommodation in polycrystalline Ni-base superalloys. Proceedings of the SEM Annual Conference, Indianapolis June 2010.

Westergaard HM., Bearing pressures and cracks. Journal of Applied Mechanics, v. 6, pp. 49-53 (1939).

Williams ML. On the stress distribution at the base of a stationary crack. Journal of Applied Mechanics v. 24 pp. 109-114 (1957).

Zhang N., Tong W., an experimental study on grain deformation and interactions in an Al-0.5% Mg multicrystal. International Journal of Plasticity, v. 20, p. 523 (2004).

Zhao L.G., Tong J., Byrne J., The evolution of the stress-strain fields near a fatigue crack tip and plasticity-induced crack closure revisited. Fatigue and Fracture of Engineering Material Structures, v. 27, pp. 19-29 (2004).

Zhao Z., Ramesh M., Raabe D., Cuitino A. M., Radovitzky R., Investigation of three-dimensional aspects of grain-scale plastic surface deformation of an aluminum oligocrystal. International Journal of Plasticity, v. 24, p. 2278 (2008).

Zhu T., Sutton M.A., Li N., Orteau J.-J., Cornille N., Li X., Reynolds A.P., Quantitative stereovision in a scanning electron microscope, Experimental Mechanics, v. 51, n. 1, p. 97 (2011).

Author's Biography

Jay D. Carroll was born on November 23, 1981 in Salt Lake City, UT to Doug and Colleen Carroll. The oldest of three children, Jay spent the summers boating with his family and engaging in numerous outdoor sports. In May of 2004, he graduated with honors from the University of Utah with a Bachelor's degree in Mechanical Engineering. After graduation, Jay spent the summer as an intern for ATK Thiokol.

In fall of 2004, Jay moved to Urbana to start his graduate career at the University of Illinois. He worked under the guidance of Professor Darrell Socie for his Master's degree on interfacial fracture toughness of hard surface coatings. Jay stayed at the University of Illinois to begin his doctoral studies in 2006 with Professor John Lambros. For the past five years, Jay has performed countless experiments on fatigue crack growth, taught a course on experimental stress analysis, and attended numerous conferences to present his work.

While working on his doctorate degree, Jay has been living apart from his wife, Crystal, who is pursuing a Ph.D. in school psychology at the University of Wisconsin-Milwaukee. After graduation, Jay and Crystal (with child on the way) are excited to live together in Albuquerque, New Mexico where Jay will begin a Post-Doctoral position at Sandia National Laboratory.